universität wien

MASTERARBEIT | MASTER'S THESIS

Titel | Title

Irradiation-Induced Noble Gas Trapping and Carbon Atom Displacement in Single and Double Layer Graphene

verfasst von | submitted by

Milan Paraš BSc

angestrebter akademischer Grad | in partial fulfilment of the requirements for the degree of

Master of Science (MSc)

Wien | Vienna, 2025

Studienkennzahl lt. Studienblatt | Degree programme code as it appears on the student record sheet:	UA 066 876
Studienrichtung lt. Studienblatt | Degree programme as it appears on the student record sheet:	Masterstudium Physics
Betreut von | Supervisor:	Univ.-Prof. Dr. Jani Kotakoski
Mitbetreut von | Co-Supervisor:	Mgr. Jana Dzíbelová Ph.D.

Mojim roditeljima.

Mama, uhvatio sam munju!

Abstract

This study explores the controlled implantation of xenon atoms into double layer graphene using low-energy ion plasma irradiation, aiming to understand implantation behavior at the atomic scale and determine the threshold displacement energy of carbon atoms in single layer graphene. The work examines the feasibility of trapping noble gases within the double layer graphene, as well as the spatial distribution and implantation density of xenon under various irradiation conditions.

Due to its atomic thickness, chemical stability, and mechanical strength, graphene offers a unique platform for nanoscale material manipulation. High-resolution imaging and spectroscopic characterization were performed using aberration-corrected scanning transmission electron microscopy (STEM) and electron energy loss spectroscopy (EELS), while data analysis combined manual annotation and semi-automated Python tools for identifying clean areas and xenon clusters.

Contrary to theoretical expectations, xenon implantation was observed under all experimental conditions, including those designed to reduce ion kinetic energy through electrical biasing below the threshold required to penetrate the graphene lattice. Measurable implantation still occurred even in this condition. Implantation densities varied across samples, but no case showed complete suppression. Structural damage induced by ions was visible in both single and double layer graphene regions. Implanted xenon clusters exhibited high mobility and internal rearrangement, revealing their metastable nature.

Overall, the results demonstrate that noble gas implantation into double layer graphene is feasible and highly efficient, even at low ion energies. These insights provide a basis for future experimental efforts in atomic-scale defect-engineering of 2D materials.

Zusammenfassung

Diese Studie untersucht die kontrollierte Implantation von Xenon-Atomen in doppellagiges Graphen mittels niederenergetischer Plasmaionen-Bestrahlung, mit dem Ziel, das Implantationsverhalten auf atomarer Skala zu verstehen und die Schwellenenergie für die Verdrängung von Kohlenstoffatomen in einlagigem Graphen zu bestimmen. Dabei wird sowohl die Machbarkeit der Einschließung von Edelgasen zwischen den Graphenschichten als auch die räumliche Verteilung und Implantationsdichte von Xenon unter verschiedenen Bestrahlungsbedingungen analysiert.

Aufgrund seiner atomaren Dicke, chemischen Stabilität und mechanischen Festigkeit bietet Graphen eine einzigartige Plattform zur Materialmanipulation im Nanomaßstab. Für die hochauflösende Bildgebung und spektroskopische Charakterisierung wurden aberrationskorrigierte Raster-Transmissionselektronenmikroskopie (STEM) und Elektronen-Energieverlustspektroskopie (EELS) eingesetzt. Die Datenauswertung erfolgte durch eine Kombination aus manueller Annotation und halbautomatisierten Python-Skripts zur Identifikation sauberer Bereiche und von Xenon-Clustern.

Entgegen theoretischer Erwartungen wurde die Xenon-Implantation unter allen experimentellen Bedingungen beobachtet, auch unter solchen, bei denen durch elektrische Vorspannung die kinetische Energie der Ionen unter die Schwelle gesenkt werden sollte, die für das Eindringen in das Graphengitter erforderlich ist. Selbst unter diesen Bedingungen trat eine messbare Implantation auf. Die Implantationsdichten variierten zwischen den Proben, jedoch konnte in keinem Fall eine vollständige Unterdrückung festgestellt werden. Strukturelle Schäden, verursacht durch die Ionen, waren sowohl in ein- als auch in doppellagigen Graphenbereichen sichtbar. Die implantierten Xenon-Cluster zeigten eine hohe Mobilität und interne Umstrukturierung, was auf ihren metastabilen Charakter hinweist.

Insgesamt zeigen die Ergebnisse, dass die Implantation von Edelgasen in doppellagiges Graphen nicht nur möglich, sondern selbst bei niedrigen Ionenenergien hoch effizient ist. Diese Erkenntnisse liefern eine Grundlage für zukünftige experimentelle Arbeiten im Bereich der atomaren Defekt-Engineering zweidimensionaler Materialien.

Acknowledgements

As it is only natural, the deepest thanks go to my mentors, Professor Jani Kotakoski and Jana Dzíbelová, who not only gave me the chance to pursue my research dream, but welcomed me into the company and community of serious and accomplished scientists. Without the two of them, their eye for detail and their unwavering commitment, this thesis would not be of the same scope or quality. I am truly grateful that it was you who became a part of my scientific growth. All that remains now is to enjoy the fruits of our work and successes together, and to continue the collaboration on the projects that the future has yet to bring.

The life and work of a scientist would be a sad and lonely place without people to share the experiences and successes with. I consider myself incredibly lucky, because whenever I found myself at a dead end, day or night, I could count on the support of Shrirang Chokappa with irradiation, Philipp Irschik for heating or programming issues, Wael Joudi for the laser cleaning process, and Clemens Mangler for absolutely everything else one could possibly imagine. Thank you for letting me learn about these tools from you, it made all the difference.

If there's one thing I know for certain, it's that in science, one of the most important skills is the ability to ask for help. I've always lived by the quote: "Help will always be given at Hogwarts to those who ask for it" and this person truly let me live my scientific Hogwarts fantasy. Not even a thousand thank-yous would be enough for what Thuy An Tripathi Bui has done for me. In our daily life, learning is a normal thing, but learning from Thuy An is an absolute privilege, honor and a joy that life rarely grants. She didn't just teach me the skills I needed to be a diligent, responsible, and competent scientist, but she showed me what it means to be a true and honest friend, and a good person in this world. She gave me wings, and for that, I will be endlessly grateful.

In my best attempt to avoid yet another metaphor about the journey of life, I'll stop right after this one. Sometimes, life comes at you like the wind. Some gusts carry you high and far, and others slam you to the ground. But nothing steers these winds quite like friendship. So to Ana, Marko, and Crissi - thank you. Thank you for always being there to give me just the kind of wind I needed to fly.

There's a saying: "If you want something done - get yourself a Virgo friend." There is little more to be said about one of my best friends, Aleksandar, except that the brilliance and sharpness of this thesis belong only to him. Thank you for the countless hours of commitment, reading

and refining. Without you, neither this thesis nor my mental health would be anywhere near where they are now. You've set the standard for friendship, expertise, and patience (despite being positively bedeviled with meetings etc.) and I sincerely hope I never have to display you to (this kind of) troubles ever again.

It hardly seems fair to thank last the people who made this entire journey possible from the very beginning, but I suppose that's how the tradition goes. My brother Ognjen, my mother Smiljana, and my father Goran are a kind of support that cannot be described in words of this world. The love, care, wisdom, and guidance you've given me, through life and now through this, are something I will be eternally thankful for. This academic and personal achievement belongs fully and completely to you. Thank you!

And yes, I really hope that my grandma Cvetana doesn't cry again when she reads this.

Contents

Chapter 1

Introduction

Since the groundbreaking isolation of single-layer graphene in 2004 [1], the field of two-dimensional (2D) materials has rapidly evolved, expanding to include a wide variety of atomically thin crystals. These include insulating hexagonal boron nitride (hBN), semiconducting transition metal dichalcogenides (TMDs), and other layered compounds with distinct physical properties. The reduced dimensionality of these systems not only enhances their electrical, mechanical, and optical characteristics, but also renders them highly sensitive to external stimuli such as light, electrons, and energetic ions. This sensitivity opens new possibilities for manipulating matter at the atomic scale, offering control over material properties.

Graphene, composed of a single layer of sp^2-bonded carbon atoms arranged in a honeycomb lattice, has served as a model system for studying 2D material behavior under extreme conditions [2, 3, 4]. Its exceptional mechanical strength, high carrier mobility, and chemical inertness make it ideal for fundamental studies of defect formation and atomic-scale engineering. A defining feature of 2D materials like graphene is their exposure of every atom to the environment, making them especially prone to structural modification through irradiation. Consequently, controlled irradiation has emerged as a versatile tool to modify and engineer the atomic structure of these materials, enabling the introduction of vacancies [5], substitutional atoms [6], and nanoscale heterostructures [7] with high spatial precision.

Energetic ion and electron beams have proven to be particularly effective means of tailoring the atomic landscape of 2D systems [8]. Electron beams in scanning transmission electron microscopy (STEM) allow real-time visualization of atomic structures and defects with sub-nanometer resolution, while ion beams offer direct means to displace atoms and implant foreign species.

In the case of noble gas ions such as xenon (Xe), ion irradiation can be used both to probe the fundamental displacement behavior of target atoms and to manipulate the lattice by trapping atoms between 2D layers. When single or double layer graphene is exposed to heavy ions like Xe^+, momentum transfer from the ions can displace carbon atoms from their lattice sites, thus forming vacancies and interstitials. Simultaneously, implanted noble gas atoms may become trapped between graphene layers [9].

Understanding these processes requires a deep knowledge of both the nuclear and electronic stopping mechanisms that govern energy loss during ion irradiation. While nuclear stopping dominates at low energies and results in direct momentum transfer to atoms, so-called knock-on damage, electronic stopping becomes relevant at higher energies and involves interactions with the electronic structure of the target [10]. The threshold displacement energy (T_d) of carbon atoms in graphene is a key parameter that dictates whether a collision event leads to the formation of a stable defect. Experimental measurements combined with simulations have estimated T_d to be in the range of 21–23 eV for single layer graphene, though this value may vary with the local bonding environment [11, 12]. Moreover, the behavior of defects under electron irradiation in STEM can be quantitatively studied by tracking the evolution of atomic configurations over time. By recording time series of atomically resolved images, researchers have been able to extract displacement cross sections and correlate them with the incident beam energy and dose [13]. These approaches provide a framework for quantifying irradiation-induced changes and comparing them to theoretical models of beam-induced damage.

In this research, we aim to explore the atomic-scale effects of noble gas ion irradiation on graphene, focusing particularly on the displacement of carbon atoms in single and double layer and trapping of xenon atoms in double layer graphene. Using a combination of experimental techniques, including low-energy ion irradiation and high-resolution STEM imaging, we investigate the threshold displacement energy of carbon atoms and the conditions under which noble gases can be encapsulated between graphene layers. Our goal is to establish a comprehensive understanding of ion–solid interactions in 2D materials and to assess the feasibility of manipulating matter at the atomic level using controlled irradiation. These insights will guide future strategies for defect engineering, ion implantation, strain engineering and nanoscale device fabrication using atomically thin materials.

Chapter 2

Materials

2.1 Graphene

Graphene is one of the most remarkable representatives of two-dimensional materials, consisting of a single layer of carbon atoms arranged in a hexagonal honeycomb lattice. The unique atomic arrangement of graphene is based on sp^2 hybridization, where each carbon atom forms three strong covalent bonds with its neighboring atoms at angles of 120° (σ bonds). The fourth valence electron remains in an unhybridised p orbital, which extends perpendicular to the plane of the sheet. These p orbitals overlap sideways with those of adjacent carbon atoms, forming delocalized π bonds across the entire lattice. This combination of localized σ and delocalized π bonds results in an exceptionally stable and tightly packed two-dimensional structure as illustrated in the Figure 2.1

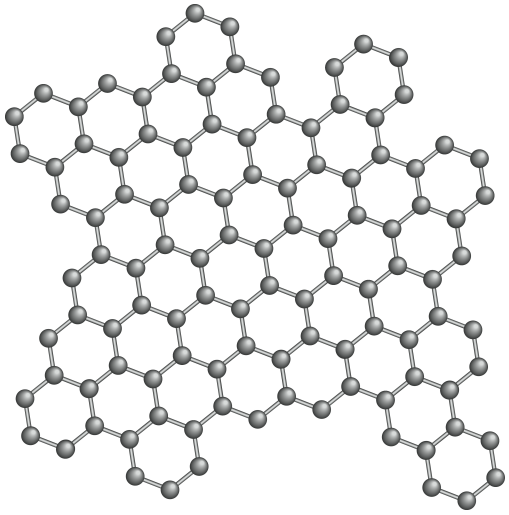

Figure 2.1: Graphical representation of graphene. Spherical, gray structures represent C atoms.

These specific bonding configurations are responsible for graphene's extraordinary electronic (delocalized π electrons from unhybridized p orbitals and honeycomb lattice symmetry), mechanical (strong in-plane σ bonds), and thermal properties (covalent bonds), making it one of the most exciting materials studied in modern material physics.

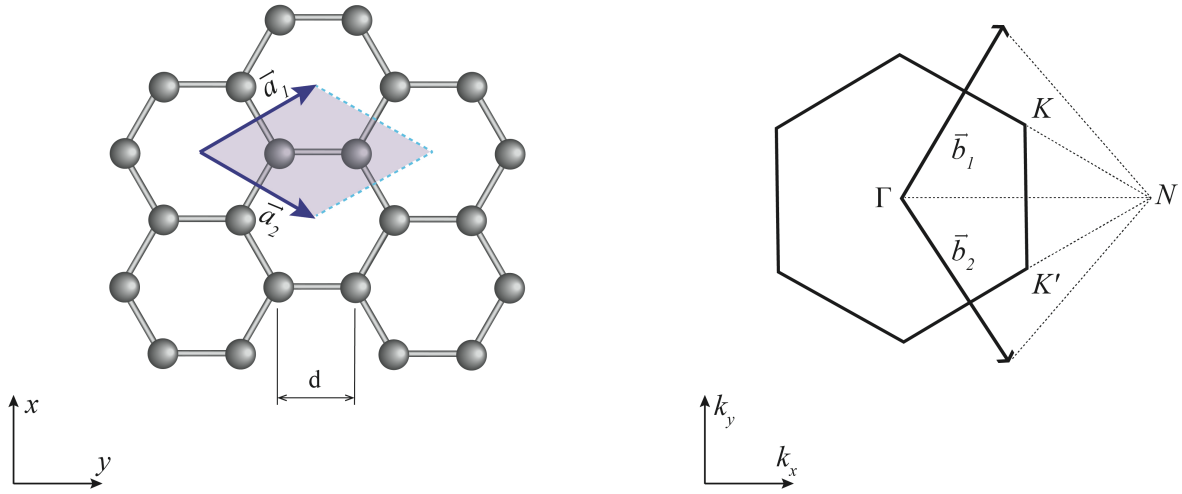

Figure 2.2: Left: graphical representation of the lattice vectors $\vec{a}_1$ and $\vec{a}_2$ of graphene; honeycomb lattice structure with unit cell highlighted in light blue; d is the distance between two carbon atoms, i.e., the bond length. Right: graphical representation of the first Brillouin zone of graphene lattice in the reciprocal vector space, with corresponding symmetry points Γ, K, K' and M as well as reciprocal lattice vectors $\vec{b}_1$ and $\vec{b}_2$.

Based on trigonometry and as illustrated on the left side of the Figure 2.2, the real space lattice vectors $\vec{a}_1$ and $\vec{a}_2$ are defined as

$$\vec{a}_1 = \sqrt{3}d\begin{pmatrix}\frac{\sqrt{3}}{2} & \frac{1}{2}\end{pmatrix}, \quad \vec{a}_2 = \sqrt{3}d\begin{pmatrix}\frac{\sqrt{3}}{2} & -\frac{1}{2}\end{pmatrix}, \tag{2.1}$$

where $d = 1.42\ \mathring{A}$ is the bond length, i.e., the distance between two carbon atoms. The lattice vectors in the reciprocal space $\vec{b}_1$ and $\vec{b}_2$, shown on the right side of the Figure 2.2, are given by

$$\vec{b}_1 = \frac{2\pi}{3d}\begin{pmatrix}1 & \sqrt{3}\end{pmatrix}, \quad \vec{b}_2 = \frac{2\pi}{3d}\begin{pmatrix}1 & -\sqrt{3}\end{pmatrix} \tag{2.2}$$

respecting the relation between real and reciprocal space

$$b_i \cdot b_j = 2\pi\delta_{ij} \ , \tag{2.3}$$

where δ_{ij} is Kronecker delta and is defined as

$$\delta_{ij} = \begin{cases} 1 \ \ if \ \ i = j \ , \\ 0 \ \ otherwise. \end{cases} \tag{2.4}$$

The first Brillouin zone, i.e., the Wigner-Seitz cell of the reciprocal lattice, as shown in the Figure 2.2, is a hexagon consisting of four symmetry points Γ, K, K' and M [14]. When it comes to graphene, K and K' are also known as Dirac points and their coordinates in reciprocal space are given by

$$\vec{K} = \frac{2\pi}{3d}\left(1 \quad \frac{1}{\sqrt{3}}\right), \quad \vec{K'} = \frac{2\pi}{3d}\left(1 \quad -\frac{1}{\sqrt{3}}\right) \ . \tag{2.5}$$

Dirac points in the reciprocal lattice space are very interesting as they represents locations in the electronic band structure of graphene where conduction and valence bands meet. These points are of high interest, since there the electrons in graphene behave as massless relativistic fermions, meaning that their energy dispersion relation follows a linear dependence with momentum [15, 16]. In standard materials, electrons behave as classical particles with an effective mass, whereas with graphene this is not the case. The Dirac equation is the one responsible for governing the low-energy excitations around the Dirac points, which ultimately leads to the quantum effects known as Klein tunneling, high carrier mobility and quantum Hall effect [17, 18].

Based on the work of Jishi et al. [19], by utilizing the tight-binding approximation, the following analytical form for the electronic band structure of graphene was determined:

$$E(\vec{k}) = \pm\gamma_0\sqrt{1 + 4\cos\left(\frac{\sqrt{3}}{2}\cdot ak_x\right)\cos\left(\frac{1}{2}\cdot k_y a\right) + 4\cos^2\left(\frac{1}{2}\cdot k_y a\right)} \ , \tag{2.6}$$

where γ_0=2.7 eV is defined as the nearest C-C neighbor tight binding overlap energy, i.e., transfer integral between two neighboring p_z orbitals. The energy dispersion around two Dirac points can be approximated to

$$E(\vec{k}) = \pm \hbar v_F |\vec{k}| \ , \tag{2.7}$$

where $\hbar$ is the reduced Planck constant, v_F is the Fermi velocity or electronic group velocity

$$v_F = \frac{\sqrt{3}}{2} \frac{\gamma_0 \, a}{\hbar} \tag{2.8}$$

and a (see Figure 2.2 lattice vectors) is the lattice constant of graphene, $||\vec{a}_1|| = ||\vec{a}_2|| = a = 2.46 \, \mathring{A}$. At each of the K points of the Brillouin zone, i.e., where $k_x = k_y = 0$, the energy comes to the zero value as both the conduction ($E > 0$) and valence ($E < 0$) band touch, which graphically forms a shape that is also known as the Dirac cone. The effective mass of the electron is proportional to the second derivative of $E(k)$, following a linear trend that is resulting in massless electrons, also known as Dirac electrons, that resemble relativistic particles with zero rest mass and move at speeds of roughly 10^6 m/s [20].

Graphene's exceptional mechanical strength has been extensively characterized using techniques such as nanoindentation [21] and Raman spectroscopy [22], and it has demonstrated to act as an impermeable atomic membrane [23]. The authors Bunch et al. [23] investigated gas leakage by varying the pressure outside a graphene-covered aperture, thereby introducing a pressure differential across the membrane. This experiment was performed for graphene membranes of varying thicknesses. Exploration of graphene's impermeability showed the ability to detect permeation of only a few atoms per hour for gases including helium, neon, nitrogen, oxygen, argon, krypton, and xenon, with hydrogen being the only gas showing significant permeation [24]. Furthermore, experiments demonstrated that graphene can withstand macroscopic volumes of trapped gas [25]. Mechanically exfoliated graphene that was supported on SiO_2/Si substrate was exposed to HF/H_2O etching or proton irradiation, causing gas release from the substrate and accumulation at the graphene/SiO_2 interface. This process led to the formation of bubbles in the graphene layer, which were subsequently characterized by scanning tunneling microscopy (STM) and atomic force microscopy (AFM). Multiple studies have since focused on gases, especially inert gases, confined beneath graphene membranes, some of which were introduced in the initial discussion.

In this work, graphene also serves as a STEM sample holder, providing a stable environment for imaging inert gas atoms. Graphene's atomic thickness allows electron transmission with minimal phase shift, thus preserving the amplitude and rendering the electron beam spreading, induced by the specimen, negligible, and its mechanical robustness enables stable suspension over large regions [26]. Furthermore, graphene shows high stability, due to a very low displacement cross section, in the order of 10^{-4} barns at 80 kV and approximately 0.2 barns at 100 kV [11, 27]. This stability is what makes graphene suitable for a role of STEM support and its ability to trap atoms between layers allows it to be employed for studying samples that would not survive

vacuum conditions or would not exist without such encapsulation [28, 29, 30, 31]. Encapsulated materials, i.e., trapped molecules between van der Walls layers, experience pressures in the order of 1.2 ± 0.3 GPa [32].

Nanoindentation of graphene using an AFM revealed a tensile strength of 130 GPa and a breaking strength exceeding 200 times that of steel, with a Young's modulus in the range of 0.5 to 1 TPa, for high-quality samples [33, 34, 35]. In terms of electrical properties, graphene exhibits exceptionally high electron mobility, reaching 2000 cm^2 /V·s at room temperature for mechanically exfoliated samples, resulting in measurable quantum Hall effect at room temperature for both electrons and holes [36].

2.2 Ultra-high Vacuum System

Ultra-high vacuum (UHV) represents an environment where the pressure is lower than 10^{-9} mbar (or 10^{-7} Pa). In those extreme conditions, the number of gas molecules is drastically reduced, thus making UHV crucial for experiments and applications where even the smallest amount of residual gas contamination could affect the results. Naturally, achieving these conditions from ambient requires a multi-step pumping and preparation processes that gradually remove air and other gases from the enclosed system.

In general, reaching UHV from ambient conditions begins with rough pumping, where a rotary vane (or scroll) vacuum pump lowers the pressure to around 10^{-3} mbar by removing most of the gases that are usually in the atmosphere (nitrogen, oxygen, carbon dioxide, water vapor). After that, a high-vacuum stage proceeds, using either a turbomolecular pump or a diffusion pump to bring the pressure down further to approximately 10^{-6} mbar. Finally, in order to reach ultra-high vacuum, specialized pumps such as ion (-getter) pumps, titanium sublimation pumps, or cryogenic pumps are used. These operate by ionizing gas molecules and trapping them on surfaces or condensing them at extremely low temperatures. To speed up this process and remove gas molecules stuck to the inner surfaces, a bakeout procedure is often performed. This involves heating the whole system (or just one part, depending on the setup) to temperatures between 100 and 300 °C for several hours with continuous pumping out of the released gases.

Once the UHV is achieved, crucial step is the maintenance. Pumps continue operating in order to remove any newly formed gas molecules. The materials inside the vacuum chamber are usually stainless steel, and surfaces are polished, cleaned, or coated for the purpose of minimizing the

contamination. If the chamber needs to be opened, it must be vented carefully using pure noble gases like argon, to prevent contamination and the adsorption of moisture on the surfaces.

All the experiments in this work were conducted using a specialized system known as CANVAS (Controlled Alteration of Nanomaterials in Vacuum down to the Atomic Scale) [37]. This setup is designed for precise nanoscale characterization and manipulation of 2D materials, built around an aberration-corrected ultra-high vacuum scanning transmission electron microscope. By keeping the entire experimental process within the same vacuum environment, CANVAS minimizes contamination and limits unwanted interactions with external factors, both of which are crucial when working with delicate low-dimensional materials.

Different components of CANVAS are connected through vacuum pipelines that maintain a base pressure of 10^{-9} mbar, allowing seamless sample transfer without exposure to ambient conditions. On the first floor, the system is equipped with tools for sample loading, heating and manipulation, as well as material growth, electron beam evaporator and cleaning laser. Additionally, this is where defect-engineering and material manipulation is performed using low-energy plasma irradiation in the so-called target chamber. Once prepared, samples are transported to the ground floor via a pulley system, where they undergo high-resolution imaging and in-situ electron spectroscopy using a customized Nion UltraSTEM 100 microscope [38], or are mapped and manipulated by atomic force microscope [39].

Sample Loading

Samples are introduced into the CANVAS system through a load lock, which is an isolated vacuum compartment designed to accommodate specimens while preventing contamination. This chamber is capable of baking out samples in order to remove residual surface contaminants. The load lock is connected to the sample transport line via two gate valves and filled with argon gas before opened to ensure the least possible contact between the system's components and outer atmosphere. This process is also known as venting and it is also used to bring the load lock volume to the ambient pressure, allowing for careful exchange of pucks, which are essentially sample holders. Once the puck exchange is done, the vacuum is restored through a multi-stage pump-down procedure involving a rotary pump, a turbo-molecular pump, and an ion-getter pump. Before activating the ion-getter pumps, the system undergoes a bake-out process at 180°C to eliminate moisture and hydrocarbon contaminants accumulated during sample fabrication and transport under standard temperature and pressure conditions. This routine can

take up to twelve hours to complete, after which the sample is ready to be transferred into the system for experimentation.

Sample Transportation

The CANVAS setup uses a specialized wheeled carrier, known as a car in order to transport samples across the system. Each car can accommodate up to three samples, which are securely placed on metallic sample holders called pucks. These pucks follow a standardized mechanical design, ensuring compatibility with all instruments connected to the vacuum line. Given the extensive layout of the UHV system, the cars must be manually navigated by hand, which is achieved by using two rare earth magnets on the vehicle. To transfer a puck outside of the car, which usually takes place in devices like Nion UltraSTEM 100 and target chamber (see chapters 2.2.1 Target Chamber and 3.2 Nion Ultra STEM 100), a mechanical arm equipped with an openable jaw is used. This arm moves back and forth along the loading axis, allowing precise handling of the pucks.

Sample Storage

For experiments that span several days, samples are stored within a dedicated section of the CANVAS system known as the garage. There are two garages within the setup, one located near the irradiation setup and another adjacent to the microscopes. Structurally, the storage system consists of an entrapment pump linked to a vacuum module with eight branches, each capable of holding up to two cars. Just like the load lock, access to this storage volume is controlled via a gate valve connected to the main transport line, ensuring that stored samples remain under ultra-high vacuum conditions until they are needed for analysis.

2.2.1 Target Chamber

The target chamber is a specialized experimental setup designed to enable the modification of materials at the atomic level by combining electron beam evaporation with a low-energy plasma irradiation setup and a cleaning laser. As shown in Figure 2.3, the chamber has a central compartment, known as deceleration setup, where the puck containing the graphene sample is placed using a mechanical arm. This arm can move back and forth and rotate freely along its horizontal

axis. All instrumentation is visible in the main chamber through dedicated view ports, allowing careful monitoring of the process.

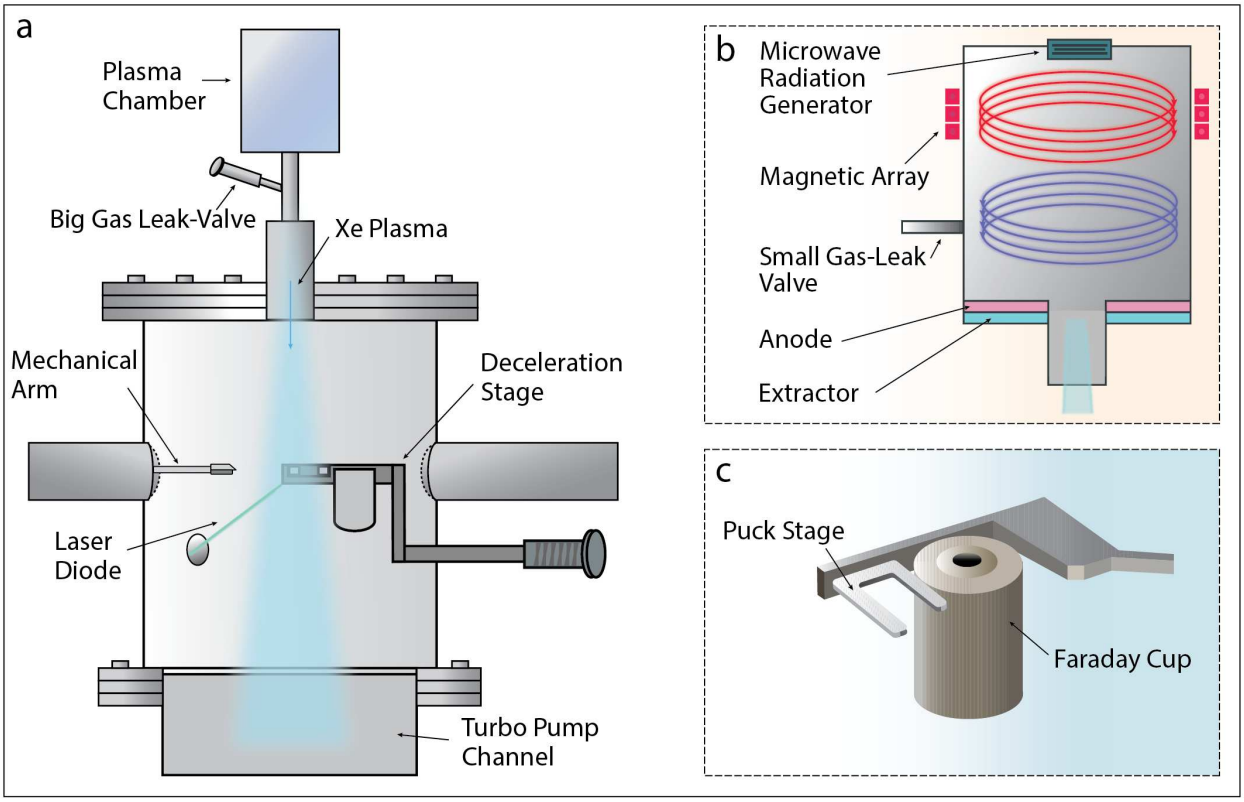

Figure 2.3: Graphic illustration of the target chamber. Panel (a) shows a cross-sectional side view of the chamber, depicting all components for controlled ion irrdiation and their arrangement. Panel (b) illustrates the plasma chamber, highlighting its key components and ongoing processes. Panel (c) depicts the deceleration stage.

At the very top of the setup, see Figure 2.3 b, a microwave generator equipped with a magnetron provides the electromagnetic radiation needed to generate plasma [40]. The microwaves are directed into the ignition chamber, where specific gases can be introduced. Plasma formation occurs when the microwave radiation reaches the electron cyclotron resonance of the gas, stripping electrons from their atomic orbits. This process generates a dynamic mixture of free electrons and positively charged ions, which begin to move under the influence of external electromagnetic fields or due to charge imbalances within the plasma itself. Moving charged particles in plasma undergo collisions with other particles, thus exchanging their energy and transferring their momentum. Ions are extracted from the plasma with an extractor potential and diverted towards the sample positioned in the puck stage of the deceleration setup.

To monitor the presence and behavior of the plasma by measuring the current produced by caught

charged particles, a Faraday cup is positioned at the puck stage height [41]. At this level, the system is also equipped with a 60 W, 437 nm laser diode laser. The laser serves primarily to minimize hydrocarbon contamination and maintain the sample's cleanliness. It operates under software control, where parameters such as illumination time and power can be adjusted, and laser alignment can be verified through integrated cameras. To maintain the high purity of the vacuum environment, the entire system is isolated from the rest of the ultra-high vacuum setup through a gate valve. A turbo-molecular pump, located at the base of the target chamber, ensures an exceptionally low pressure of approximately $1 \cdot 10^{-10}$ mbar, providing the necessary conditions for contamination-free material processing.

2.3 Ion Irradiation

Ion irradiation, particularly with heavy ions, represents a technique in material science, used for modifying material properties, creating defects, and studying radiation effects under controlled and defined conditions. Heavy-ion irradiation involves the use of high-energy ions, such as xenon with atomic number $Z = 54$, which penetrate the target material, displacing atoms and creating defects within the lattice.

The experimental setup for (heavy-) ion irradiation consists of an ion source, accelerator, puck stage and Faraday cup, all incorporated into the target chamber (see Figure 2.3), and is designed to ensure precise control over irradiation conditions. The energy of the ions is carefully selected based on the interaction dynamics within the target material.

When ions strike a material, their interactions can be broadly categorized as either elastic or inelastic scattering. While properties such as mass, energy, and momentum help describe these collisions and predict their influence on the material's structure, the underlying dynamics are often complex [42]. In the basic view of considering a material as a lattice of stationary atoms and electrons, conservation laws apply, which means that the total energy and/or momentum of the ion or electron and material system remain constant throughout scattering events, as schematically shown in Figure 2.4. This allows for modeling the ion's energy loss using measurable properties like the composition and density of the target material. As the ion penetrates the medium, it undergoes a series of collisions, gradually losing its energy. This energy loss per unit distance is described by the stopping power S, defined as

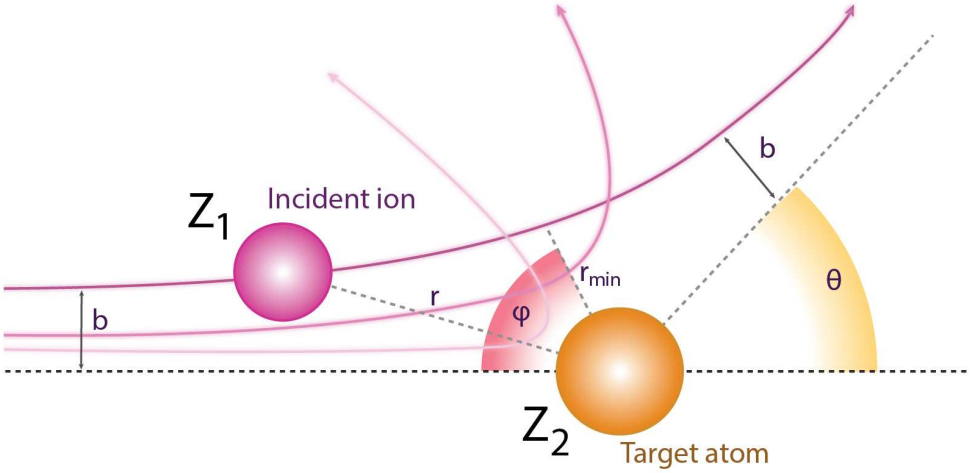

Figure 2.4: Schematic of a scattering event between an accelerated ion with atomic number Z_1 and a stationary target atom with atomic number Z_2. The changes in the ion's trajectory are shown as lines, illustrating how they vary with the beam parameters. b is the impact parameter, r is radial distance between particles, $r_{min} = \pi - 2\varphi$ is the smallest collision distance, φ is the collision angle, and θ is the scattering angle.

$$S = -\frac{dE}{dx} \ , \tag{2.9}$$

where E is the ion's kinetic energy and x is the path length traveled by the ion [43]. There are two principal mechanisms by which ions lose energy: electronic stopping, S_e, which represents the energy loss due to the excitation or ionization of electrons in the target, and nuclear stopping, S_N, that occurs through elastic collisions with the nuclei of the target atoms [44]. The total stopping power is the sum of these two contributions

$$S = S_e + S_N = -\left(\frac{dE_e}{dx} + \frac{dE_N}{dx}\right) \ . \tag{2.10}$$

Which mechanism dominates depends on the ion's energy and the nature of the target. Generally, nuclear stopping is more significant at low energies, while electronic stopping dominates at higher energies. In most real scenarios, both mechanisms contribute simultaneously [42].

In the case of this study, heavy-ion irradiation serves a dual purpose: first, to study defect dynamics and threshold displacement energies, and second, to explore potential trapping mechanisms for noble gas atoms between graphene layers. The interactions between heavy ions and graphene bilayers can lead to intercalation effects, where noble gas atoms become confined between the

layers. The success of heavy-ion irradiation experiments depends on the precise control of ion beam parameters.

2.3.1 Cross Section

When discussing interactions between electrons or ions and atoms or solid materials, it's very important to introduce the concept of the cross section. When a beam of particles interacts with a solid target, the stochastic nature of individual events, combined with the sheer number of particles involved, makes it practically impossible to predict the behavior of each particle individually. At its core, this idea helps describe how likely it is that a specific type of interaction, such as scattering, will take place between two energetic particles. The cross section provides a quantitative measure of that probability and is commonly expressed in internationally recognized units called barns, where one barn equals 10^{-24} cm^2 [11]. In more intuitive terms, it can be thought of as the effective target area of an atom in the particular interaction.

The differential cross section ($d\sigma/d\Omega$) is particularly significant, as it characterizes the probability of a particle being scattered into a specific solid angle ($d\Omega$) or of a particular amount of energy being transferred to a target atom, in other words, it describes the angular distribution of scattering from an atom [45]

$$\frac{d\sigma}{d\Omega} = \frac{1}{2\pi \sin(\theta)} \frac{d\sigma}{d\theta} \quad . \tag{2.11}$$

Mathematically, it quantifies the likelihood that the energy T will be transferred to an atom within the narrow range between T and $T + dT$, or that a projectile will scatter into a small angular range between θ and $\theta + d\theta$ [46].

Upon integration over all scattering angles or energy values, the differential cross section yields the total cross section, which represents the overall probability of an interaction occurring, irrespective of the direction or energy transfer involved

$$\sigma_{atom} = \int_0^{\theta} d\sigma = 2\pi \int_0^{\theta} \frac{d\sigma}{d\Omega} \sin(\theta)\, d\theta \quad \text{and} \tag{2.12}$$

$$\sigma_{total} = N\, \sigma_{atom} = \frac{N_A\, \sigma_{atom}\, \rho}{A} \quad , \tag{2.13}$$

where σ_{atom} is the scattering cross section in the simple case of one atom, N_A the Avogadro's number and A is the atomic weight of the scattering atoms in the specimen ($\frac{kg}{mol}$) which has density ρ ($\frac{kg}{m^3}$).

2.3.2 Nuclear Stopping

At lower ion energies, nuclear stopping becomes the predominant mechanism. Here, the ion undergoes direct collisions with atomic nuclei, transferring kinetic energy to them. If this energy exceeds the displacement threshold of the material, atoms can be ejected from their lattice sites, leading to defect formation.

The rate of energy loss through nuclear stopping E_N can be expressed as

$$\frac{dE_N}{dx} = N \int T\,\sigma\big(E,T\big)dT \quad , \tag{2.14}$$

where N is the atomic density, $\sigma(E,T)$ is the cross section for the transfer of energy T. Assuming an ion with the initial kinetic energy E_0, for an elastic collision between a projectile of mass m_1 and a target atom of mass m_2, the energy transferred at a scattering angle Θ is given by

$$T = \frac{4E_0 m_1 m_2}{(m_1+m_2)^2}\ \sin^2\left(\frac{\Theta}{2}\right) \ . \tag{2.15}$$

Assuming the atoms in the material are spaced far enough apart, so that it allows the consideration of a spherically symmetric potential $V(r)$, which is something also known as binary collision approximation, the scattering angle can be expressed according to the classical scattering integral

$$\Theta = \pi - 2b\int_{r_{min}}^{\infty} \frac{dr}{r^2\left[1-\frac{V(r)}{E_k}-\frac{b^2}{r^2}\right]} \quad , \tag{2.16}$$

where b is the impact parameter, E_k is the ion's kinetic energy and r_{min} is its point of closest approach to the nucleus [47]. Rutherford originally proposed a screened Coulomb potential to describe $V(r)$

$$V\big(r\big) = \frac{1}{4\,\pi\,\varepsilon_0}\frac{Z_1 Z_2 e^2}{r}\cdot\phi\left(\frac{r}{a}\right) \tag{2.17}$$

with ε_0 the dielectric constant and Z_1 the atomic number of the projectile and Z_2 the atomic number of the target atom, $\phi(r)$ a radial screening function scaling as a material-dependent screening parameter a. A widely used form of the screening function is that of Ziegler, Biersack and Littmark [48]

$$\phi\left(\frac{r}{a}\right) = 0.1818e^{-3.2\frac{r}{a}} + 0.5099e^{-0.9423\frac{r}{a}} + 0.2802^{-0.4029\frac{r}{a}} + 0.0282e^{-0.2016\frac{r}{a}} \tag{2.18}$$

with the screening length given by

$$a = \frac{0.8854\, a_0}{Z_1^{0.23} + Z_2^{0.23}} \quad , \tag{2.19}$$

where a_0 is the Bohr radius and Z_1 and Z_2 are atomic numbers. Combining these models, the nuclear stopping power becomes

$$S_N = \frac{8.462 \cdot 10^{-15} Z_1 Z_2 M_1}{(M_1 + M_2)(Z_1^{0.23} + Z_2^{0.23})} S_N(\varepsilon) \quad , \tag{2.20}$$

where $S_N(\varepsilon)$ is the reduced nuclear stopping cross-section

$$S_N(\varepsilon) = \begin{cases} \frac{\ln(1+1.383\varepsilon)}{2(\varepsilon+0.01321\varepsilon^{0.21226}+0.19593\varepsilon^{0.5})} & for \;\; \varepsilon \leq 30\,, \\ \frac{\ln(\varepsilon)}{2\varepsilon} & for \;\; \varepsilon > 30\,. \end{cases} \tag{2.21}$$

2.3.3 Electronic Stopping

Unlike nuclear stopping, where ions interact directly with stationary nuclei, electronic stopping describes the transfer of energy from the ion to the electrons in the target material [48]. These electrons span a wide range of velocities, making the whole process more dynamic. According to the Thomas-Fermi atomic model [49], Bohr proposed that an ion gradually loses its outer electrons as its velocity surpasses the orbital velocity of those electrons. This leads to an effective charge

$$Z^* = Z \frac{v_1}{v_0 Z^{2/3}} \quad , \tag{2.22}$$

where v_1 is the velocity of the ion and $v_0 \approx 2 \cdot 10^6$m/s is the Bohr velocity of a hydrogen electron.

At low ion velocities ($v < v_0 Z_1^{2/3}$), the ratio Z^*/Z is less then one, meaning that the ion retains most of its electrons. Assuming most electrons have momentum $p = m_e v_F$, with v_F Fermi velocity of the electrons in the material, the stopping power in this regime scales linearly with the ion's velocity

$$\frac{dE}{dv} = \frac{dE}{dp}\frac{dp}{dv} = mp \rightarrow dE = mpdv \quad . \tag{2.23}$$

The energy loss thus depends more on the number of interactions than on the individual momenta of the electrons. This linear relationship in respect to v also holds when considering interactions with bound electrons at low ion velocities [50]. During these interactions, electrons can be transferred between the ion and the target atom. If an electron is captured by the ion, it must accelerate to match the ion's velocity, thereby gaining momentum ($m_e v$). This momentum comes from the ion, contributing to energy loss. Although this transfer does not slow down the ion directly, it contributes to the overall energy loss per unit path length.

Lindhard and Scharff [42] derived an analytical model to describe electronic stopping in this regime

$$S_e(E) = 3.83 \frac{Z_1^{7/3} Z_2}{\left(Z_1^{2/3} + Z_2^{2/3}\right)^{3/2}} \left(\frac{E}{M_1}\right)^{1/2} \quad , \tag{2.24}$$

where the slope is in direct dependence on the atomic mass and number of the ion and target atom.

At high ion energies the ions behave more like fast-moving, bare positive charge, that move faster than the electrons in the material [43]. In this regime, the ion's high energy prevents easy neutralization by electrons. Consequently, interactions become dominated by pure Coulomb scattering between the ion and negatively charged electrons in the material. The electronic stopping power, defined as the rate of energy loss per unit path length, is then expressed as

$$S_e = -\frac{dE_e}{dx} = n_e \int T \frac{d\sigma}{dT} dT = n_e \int_{b_{min}}^{b_{max}} T\, 2\pi b\, db = \frac{4\pi Z_1^2 e^4}{v^2} \frac{M_1}{m_e} \ln\left(\frac{b_{max}}{b_{min}}\right) \quad , \tag{2.25}$$

and here, $b_{\min}$ and $b_{\max}$ are the minimum and maximum impact parameters, respectively, which define the range of effective interactions, Z_1 is the ion's charge, v its velocity.

Bethe noted [51] that the minimum impact parameter $b_{\min}$ corresponds to the maximum energy

transfer, which must at least be sufficient to ionize the target atom, this sets a lower bound on the energy an electron can receive. Conversely, the maximum impact parameter $b_{\max}$ is associated with a head-on collision, where the maximum momentum and energy transfer occurs and is roughly proportional to $2v$. Taking these considerations into account, the electronic stopping power simplifies to

$$S_e(E) = \frac{2\pi Z_1^2 e^4}{E} \frac{NZ_2}{M_1} m_e \ln\left(\frac{2m_e v^2}{I}\right) \quad , \tag{2.26}$$

where N is the number density of target atoms, Z_2 is the atomic number of the target, M_1 is the ion mass, $I = 10Z_2$ is the average excitation energy of the target material.

2.4 Scanning Transmission Electron Microscopy

Microscopy is a fundamental scientific technique that allows researchers to explore the structure and behavior of matter at scales far smaller than what the human eye can perceive and resolve. By employing various imaging techniques, microscopy has become an essential tool in fields such as physics, chemistry, and biology, enabling scientists to visualize fine details of materials, biological cells, and nanoscale structures [52, 53]. The effectiveness of a microscope is typically measured by its resolution [54]. Over the years, continuous advancements in lens quality and optical system design have significantly improved imaging capabilities, reaching sub-micrometer scales. The resolution of an optical system is constrained by the wave nature of light (and refraction), describing how light propagates through space and matter, which present physical boundary on how finely details can be resolved [55]. This limitation, known as the diffraction barrier [56], prevents optical instruments from distinguishing two objects separated by less than approximately half the wavelength of the light used for imaging. Mathematically, the smallest resolvable distance d, i.e. the minimal resolvable distance between two objects is given by

$$d = \frac{\lambda}{2 \cdot NA} \quad , \tag{2.27}$$

which is a ratio of wavelength of light λ and numerical aperture NA, a parameter defining the microscope's light-collecting efficiency [57]. For visible light microscopy, where wavelengths range between 380 and 700 nm, this diffraction limit results in a resolution of about 200-250 nm. Consequently, structures closer than this appear blurred and indistinguishable, a restriction formally

described by Ernst Abbe in 1873 as the Abbe diffraction limit [58]

$$d = \frac{\lambda}{2 \cdot n \cdot \sin(\theta)} \leq \frac{\lambda}{2.8} \quad . \tag{2.28}$$

A major breakthrough in the early 20th century transformed microscopy with the development of quantum mechanics. Louis de Broglie introduced the wave-particle duality of matter [59], demonstrating that electrons, which were previously thought of as particles, also exhibit wave-like properties. The wavelength of an electron, known as the de Broglie wavelength λ, is inversely proportional to its momentum p as expressed by

$$\lambda = \frac{h}{p} \quad , \tag{2.29}$$

where h is Planck's constant. For an electron accelerated by a 60 kV acceleration voltage, this wavelength reduces to just 10 pm, which is significantly shorter than the one of visible light's, enabling much higher resolution imaging. When considering an electron of mass m_e traveling through an accelerating potential V in a relativistic regime

$$p^2c^2 = E^2 - m^2c^4 \tag{2.30}$$

its wavelength can be further expressed as:

$$\lambda = \frac{hc}{\sqrt{E^2 - m_e^2c^4}} = \frac{hc}{\sqrt{(m_ec^4 + eV)^2 = m_e^2c^4}} = \frac{hc}{\sqrt{eV(2m_ec^2 + eV)}} \quad , \tag{2.31}$$

where c is the speed of light, m_e is the electron mass, and e is the elementary charge. The interaction between charged particles and electromagnetic fields lays base understanding for the electron beam trajectories and ray behavior is generated and manipulated under the action of Coulomb and Lorentz force

$$\vec{F} = e\vec{E} + e(\vec{v} \times \vec{B}) \quad , \tag{2.32}$$

where $\vec{E}$ and $\vec{B}$ are electric and magnetic field respectively. Using carefully engineered electric and magnetic fields, electron beams can be focused and directed, behaving analogously to visible

light in an optical microscope. This concept led Ernst Ruska and Max Knoll to construct the first electron microscope in 1931, marking the dawn of electron microscopy [60].

Scanning transmission electron microscopy is an imaging technique that integrates the strengths of both TEM and SEM. Unlike conventional TEM, where a collimated parallel electron beam illuminates the entire sample and forms an image through projection onto the detector, STEM operates by directing a highly focused electron probe that scans across the specimen (i.e., image field, field of view). As the beam interacts with the sample, transmitted electrons are collected by a detector, generating a raster image based on the scanned area. The resolution in STEM is directly tied to the precision of the electron probe as the image is created as a convoluted product of the electron probe with the sample topology.

In order to achieve high-resolution imaging, STEM employs a cold field emission electron source, that generates an electron beam via quantum tunneling from an atomically sharp cathode under the influence of a strong electric field. This emission method is favored for its high brightness and minimal energy dispersion, both of which enhance image clarity. Structurally, a STEM microscope consists of two primary optical sections: the illumination optics, responsible for creating, accelerating and focusing the electron beam on the sample, and the projection optics, which gather the transmitted electrons and direct them toward detectors. The beam is controlled using condenser and aberration-correcting lenses, along with coils that ensure aberration correction and precise probe movement across the sample. Two objective pole pieces focus the electron beam onto the sample and collect the transmitted electrons in the projection optics. In the very last part of the column of the microscope, a projection lens in responsible for directing the electrons towards the detectors for imaging or spectroscopy.

As the electron probe penetrates and passes through the sample, interactions with atomic nuclei and electrons lead to scattering events, including elastic and inelastic collisions. High-angle scattered electrons, which result primarily from elastic interactions with atomic nuclei, are captured by annular dark-field (ADF) detectors to form atomic-resolution images. Consequently, a specialized software system processes the detected electron signals, translating them into a digital image. Segmented ADF detector works by mapping the spatial distribution of transmitted electrons across the imaging detector to specific locations in the microscope's field of view, assigning corresponding intensity values to digital pixels. For dark field imaging, only electrons that interact with the sample contribute to the final image and the brightness of any given region directly reflects the extent of electron scattering in that area.

As the sample's density and thickness increase, the probability of electron interactions rises, thus leading to enhanced contrast and greater image intensity. In ultra-thin samples, such as monolayers with varied elemental compositions, heavier elements appear significantly brighter due to their stronger scattering cross-section. This effect, known as Z-contrast, results from the direct relationship between an atom's atomic number and its interaction probability with the electron beam. The dependence of scattering intensity on atomic number follows an approximate $Z^{1.7}$ power law [61].

2.4.1 Elastic Scattering

Elastic scattering refers to the electrostatic deflection of incident electrons by the Coulomb field surrounding atomic nuclei. In this process, the total kinetic energy of the system is conserved, which is what defines it as elastic. This type of scattering is fundamental to several imaging and analytical techniques like STEM, where it it gives rise to atomic number contrast, often referred to as Z-contrast. For instance, it contributes to the formation of electron diffraction patterns and the contrast mechanisms in transmission electron microscopy (TEM), including both diffraction and phase contrast. In scanning electron microscopy (SEM), elastic scattering underlies the generation of backscattered-electron (BSE) contrast. Under certain conditions, elastic collisions can also cause displacement of atoms within a crystal lattice or result in electron-beam-induced sputtering of atoms from the surface [62].

The presence of beam-induced excitations can weaken atomic bonding, thereby reducing these threshold values. Once the displacement threshold energy is known, it becomes possible to estimate the displacement cross section σ under specified electron-beam conditions. This is commonly done using the McKinley-Feshbach formalism for relativistic Coulomb scattering of electrons [63].

2.4.2 Inelastic Scattering

Compared to the elastic scattering, the resulting deflection in inelastic scattering angles are generally smaller and associated cross section scales are approximately $\sigma \sim Z^2$. This process contributes quite significantly to the generation of secondary electrons and is key factor in several major techniques in electron microscopy. It leads to X-ray emission used by detectors for identification of elements in electron microscopy, helps create image contrast in SEM, and makes it

possible to measure electron energy losses through electron energy loss spectroscopy (EELS).

Inelastic scattering leads to both deceleration (i.e. retardation) and angular deviation of the incident electrons, while simultaneously exciting or ionizing the atoms within the target material. An approximation can be achieved using Bethe formalism [64], where Susi et al. [65] through adaptation of this approach to SI units derive the following expression for the total radiolysis cross section

$$\sigma_{rad}(E) \approx 4\pi \frac{Ze^4}{(4\pi\varepsilon_0)^2\, 2\,\gamma\, m_e c^2\, T_d\, \beta^2} \left[\log\left(\frac{2\,\gamma\, m_e\, c^2 \beta^2}{T_d\,(1-\beta^2)} \right) - \beta^2 \right] \zeta \quad , \tag{2.33}$$

where ζ is an efficiency factor, that also includes the contributions of shell-dependent factors, and describes the proportion of ionization events.

2.4.3 Aberrations

Over the decades, electron microscopy has seen remarkable advancements. The introduction of aberration-corrected electron microscopes [66], using sophisticated magnetic and electrostatic multipole lenses, has significantly reduced distortions.

Aberrations are principally deviations from the ideal optical behavior of an instrument. In an ideal system, an optical element, such as a lens, would perfectly focus rays to form an image with the characteristics predicted by Gaussian optics. However, real optical systems introduce distortions, leading to deviations from this ideal behavior.

Under ideal conditions, every electron in the ray passing through the system would perfectly map to its expected position in the Gaussian image plane, producing a sharp and well-defined image. However, aberrations introduce distortions that shift the rays away from their ideal positions, leading to blurring, contrast loss, or geometric distortions in the final image.

The aberration function for symmetric lens and phase error as a function of the angular deviation is given as

$$\chi(\alpha) = \frac{2\pi}{\lambda}\delta = \frac{2\pi}{\lambda}\left(\frac{1}{2}C_1\alpha^2 + \frac{1}{4}C_3\alpha^4 + \frac{1}{6}C_5\alpha^6 \; + \; \ldots \right) \tag{2.34}$$

with $\alpha = \sqrt{\alpha_x^2 + \alpha_y^2}$ being angular deviation and C_n aberration coefficients measured in $\mathring{A}$. From this, some of the most common aberration types are:

Spherical aberrations ($C_3 = C_{S3} = C_S$) occur when electron beam passing through different regions of a lens or an aperture come into focus at different positions along the optical axis. Ideally, according to Gaussian optics, all parts of the electron beam, regardless of whether they pass through the central or peripheral parts of the lens, should converge to a single point on the Gaussian image plane. However, in reality, this is not the case. Electron beams that pass through the outer regions of the lens or aperture (known as peripheral rays) tend to focus at different points along the optical axis compared to those passing near the center, as shown in Figure 2.5.

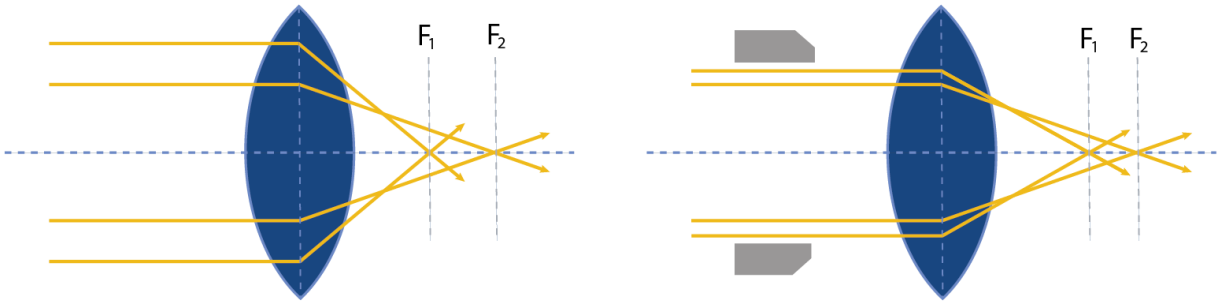

Figure 2.5: Graphical representation of spherical aberration with focal points F_1 and F_2. The case on the right shows that the use of aperture results in the two focal points being closer together.

It is said, that spherical aberration arises from non-uniform radial fields, causing electrons at different distances from the optical axis to focus at varying points, leading to image blurring. In STEM, where the probe is finely scanned, this type of aberrations contribute to increasing probe size and limits the microscope's ability to resolve fine details. In order to correct for this type of aberrations, spherical aberration correctors are used, which introduce counteracting phase shifts in order to compensate for the unwanted deviations.

Chromatic aberrations arise when electron beam carries a distribution of electrons of different wavelengths, or more precisely - different energy ranges, and as they come into focus at different positions along the optical axis, as shown in Figure 2.6. This is a significant deviation from the assumptions of Gaussian optics, which assumes a monochromatic (single-wavelength) electron beam. Since chromatic aberration directly violates this principle, it represents one of the most fundamental imperfections in electron optics.

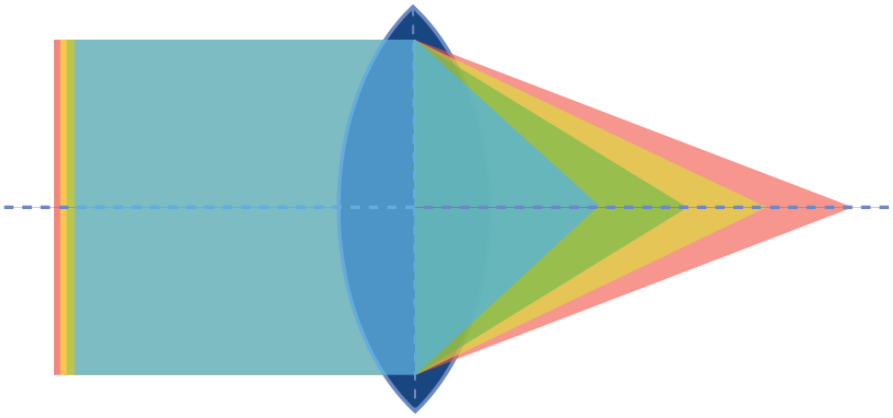

Figure 2.6: Graphical representation of chromatical aberrations.

The primary cause of chromatic aberration is that electrons entering the objective lens do not all possess the same exact energy. As a result, lower-energy and higher-energy electrons focus at different depths, leading to image blur and contrast loss.

In STEM, this aberration type typically limits spatial resolution, since electrons with slightly different energies would tend to be focused at different depths. Knowing and understanding the cause and effect, chromatic aberrations are able to be minimized through the usage of monochromators or high-voltage electron sources that are able to provide a narrow energy distribution of electrons.

Coma is a special type of aberration that falls into the category of off-axis aberrations. As the name suggests, in this case, off-axis rays focus at different positions compared to those passing along the optical axis, as shown in Figure 2.7. This results in a characteristic comet-shaped distortion, hence the name coma, where points near the edge of the field of view appear elongated or asymmetric.

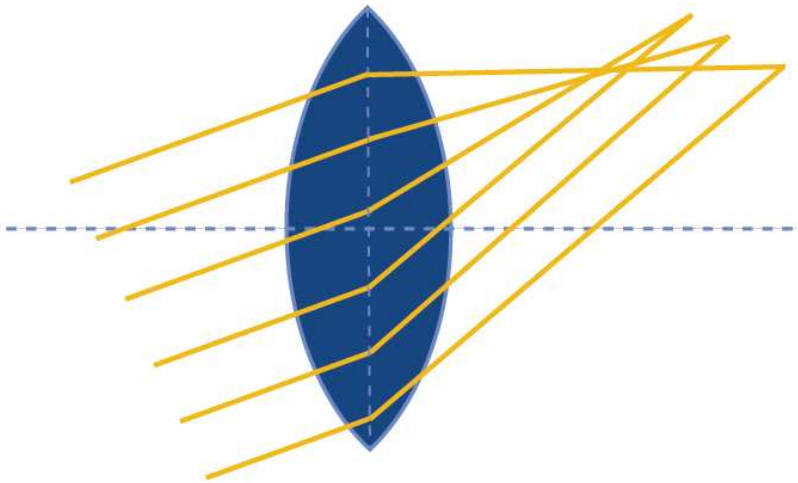

Figure 2.7: Graphical representation of coma aberation.

Coma aberration is particularly problematic in high-precision electron imaging, as even small temperature changes in the experimental setup can cause the optical system to become misaligned, worsening the coma effect. In STEM it causes an elliptical probe shape.

Astigmatism is another off-axis optical aberration, and it occurs when a lens system has different focal lengths in two perpendicular directions, as shown in Figure 2.8. Instead of focusing the electron beam into a single point, astigmatism causes the beam to focus into an ellipse or, in extreme cases, even a line.

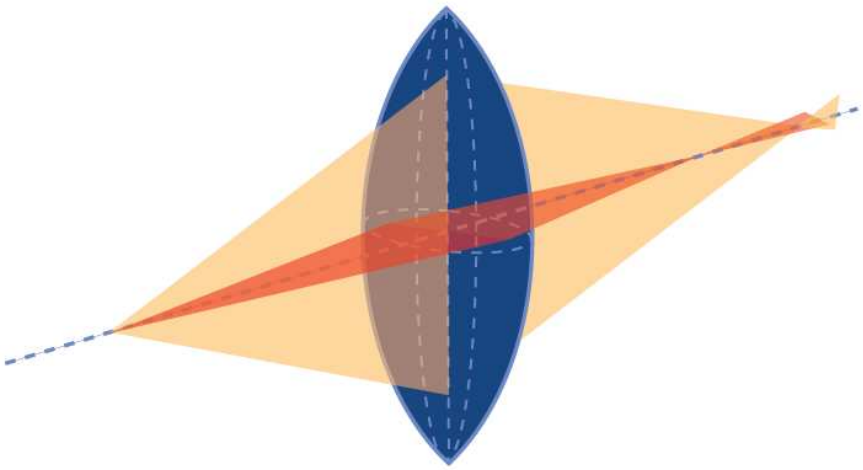

Figure 2.8: Graphical representation of astigmatism aberrations.

In STEM, this type of aberration alters the electron probe shape which turns a round probe into

an elliptical, thus directly reducing the resolution.

Defocus represents another crucial aberration that is very common in the electron microscopy. In principle, it describes how and how much the image plane is shifted along the optical axis. As an aberration function

$$\chi(\alpha) = \frac{1}{2} C_1 \, \alpha^2 \tag{2.35}$$

with defocus coefficient $\Delta f = -C_1$, describes the proportionality of defocus to the square value of the illumination angle, i.e., angular deviation. In practical sense, defocus causes uniform phase shift across the entire wavefront, which means that all electron rays experience the same type of distortion but at different strengths (depending on their angle).

2.5 Electron Energy Loss Spectroscopy

This type of spectroscopy is based on analyzing the changes in kinetic energy of an electron beam after it undergoes inelastic scattering while interacting with a target material. This energy loss, resulting from electron–matter interactions, is captured as an energy loss spectrum by measuring the energy distribution of the transmitted and scattered electrons.

EELS is typically performed in combination with a TEM or a STEM, thus providing a powerful tool for probing chemical composition and bonding configurations at high spatial resolution. When combined with imaging, EELS enables simultaneous structural and chemical characterization of a material, with spatial resolution that can reach the atomic scale and energy resolution typically better than 1 eV.

The EELS system relies on a magnetic prism, which uses a uniform magnetic field, typically around 0.01 T, generated by an electromagnet to disperse electrons according to their energy. As electrons enter this magnetic field, they follow circular trajectories with radius R and are deflected, usually by 90°, due to the Lorentz force:

$$\vec{F} = e(\vec{v} \cdot \vec{B}) = \frac{2mv}{R} \quad , \tag{2.36}$$

where e, v, and m are the electron charge, velocity, and relativistic mass. The radius of curvature, and thus the electron path, is directly related to the kinetic energy

$$R = \frac{m \cdot v}{e \cdot B} \quad . \tag{2.37}$$

This principle enables energy dispersion across the EELS detector, mapping the electron energies based on how much energy was lost during inelastic scattering.

EELS spectra can span several hundred eV, covering a wide range of inelastic interactions. These arise from energy and momentum exchange between the incoming electrons and the sample, leaving the latter in various excited states. These excitations include: lattice vibrations (phonons), plasmon oscillations from collective electron motion, and electronic transitions, where electrons are excited to unoccupied states above the Fermi level. Thanks to the variety of such processes, EELS provides rich material insights, including elemental mapping, bonding environments, and dielectric properties. The EELS spectrum is typically divided into three regions:

Zero-Loss Peak, (ZLP), centered at 0 eV energy loss, the ZLP represents electrons that either passed through the sample without undergoing inelastic scattering or lost too little energy to be resolved. Its width is mainly governed by the energy spread of the electron source. Measuring the full width at half maximum (FWHM) of the ZLP provides an estimate of the system's energy resolution. Additionally, the ZLP can be used to determine relative sample thickness using the log-ratio method based on a Poisson distribution of scattering events [67]. Typical energy resolutions range from 0.2–2.0 eV, and can reach below 10 meV with a monochromated beam.

Low-Loss Region (Valence Region), extending up to ~50 eV [68], this region is dominated by plasmon excitations (collective oscillations of quasi-free electrons) and inter- or intra-band electronic transitions. Plasmon peaks typically appear between 5 and 30 eV, providing insights into the electronic structure and dielectric properties of materials, such as the band gap. As in optical techniques like X-ray absorption spectroscopy (XAS), this region reveals information about valence electron behavior. The intensity in the low-loss region increases with sample thickness, and plasmon peak position or multiplicity may shift with increasing disorder or structural variations in the material [68].

High-Loss Region (Core-Loss Region), at energy losses above 50 eV, this region corresponds to ionization of core-level electrons, i.e., those that are deeply bound in inner atomic shells. The spectrum shows sharp features known as ionization edges, which are element-specific and arise when a beam electron transfers sufficient energy to excite a core electron into an unoccupied state above the Fermi level. These edges are typically composed of a sharp rise followed by a

gradually decaying tail, superimposed on a sloping background due to multiple scattering. Since they depend on the atomic number and local bonding environment, core-loss features can be used for precise elemental identification and to study chemical bonding.

Chapter 3

Methods

3.1 Sample Preparation

Single layer graphene used in this study was the so-called easy transfer graphene (Graphenea), which is grown via chemical vapor deposition on top of a paper-like sacrificial layer and coated by a layer of polymethyl methacrylate (PMMA) (see Figure 3.1).

The process of sample preparation was conducted on three different types of TEM grids: Quantifoil R 1.2/1.3 on 300 gold mesh grid, Quantifoil R 1.2/1.3 on 200 gold mesh grid and SiN 3x3 grid. Aside from the grids, necessary laboratory instruments, including glass plates, inverted tweezers, scalpel and glass beaker were used. Grids were carefully picked by the edge using tweezers, placed on glass plates, and inspected under a light microscope. Graphene was cut into squares matching the size of the grids and floated on deionized water after detaching from its sacrificial layer. In the deionized water submerged grid was navigated so that the floating protected monolayer graphene piece was caught onto the grid's surface. Grids were air-dried for 10 min, then heated to 150°C for 30 min. Optimal drying was found to be around 1 h in total. Coverage was verified under a light microscope. The transfer procedure is shown in the Figure 3.1.

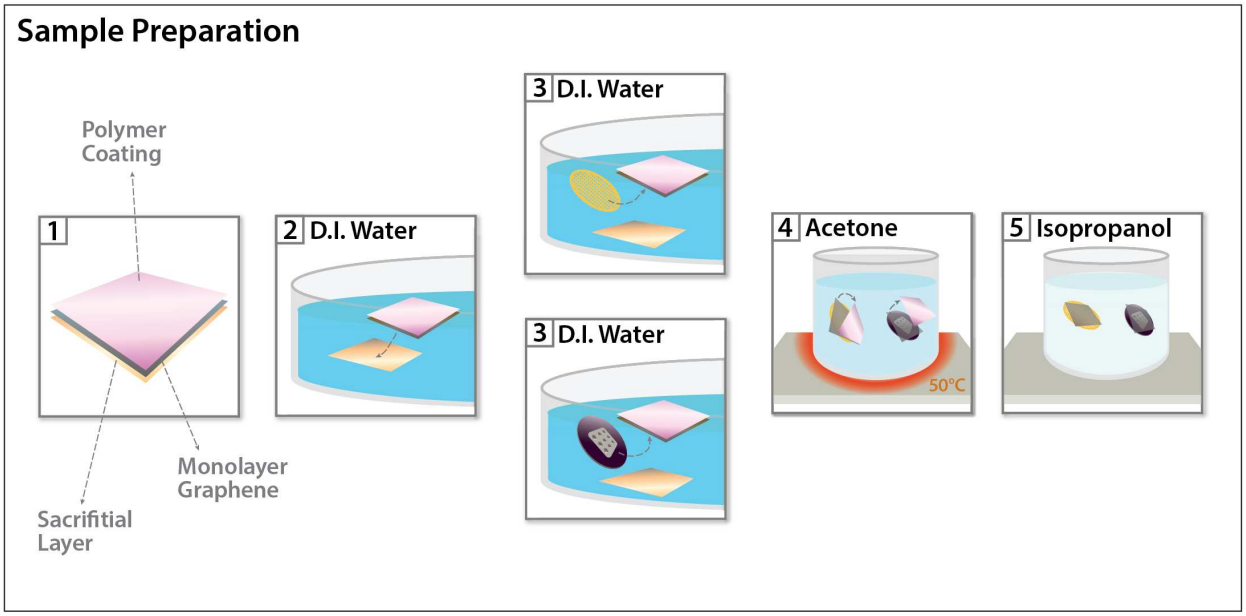

Figure 3.1: Step-by-step illustration of the transferring procedure for Easy-transfer graphene.

To remove PMMA, grids were submerged in 50°C acetone bath for 1 h, then transferred to isopropanol bath for 30 s, and air-dried again. For double layer regions, the entire procedure was repeated with flipped or identical orientations depending on grid type (same grid orientation for Quantifoil on 300 gold mesh and SiN grid, and with the opposite grid orientation for Quantifoil on 200 gold mesh grid. Prepared samples were labeled, placed in pucks, and loaded into the CANVAS system for further experiments.

3.1.1 Cleaning

Graphene was present across the newly prepared samples, but only small and limited areas appeared to be atomically clean. Coverage (presence of graphene covered regions in relation to empty grid regions) and cleanliness of these areas were assessed using STEM device. Two cleaning methods were used depending on grid type: UHV heating for Quantifoil, and laser cleaning for SiN grids.

Samples were individually loaded into an UHV heating stage using a mechanical arm. The heater design allowed close contact with sensors for temperature control. Cleaning parameters of 3 h at 450 °C were set, based on prior optimization studies [69]. The timer started once the target temperature was reached. After cleaning, samples were removed once the chamber cooled to approximately 125 °C.

Initial laser settings (0.5 % power, 1 kHz, 9000 s) were used for alignment. Due to laser instability after power changes, a 10 to 15 min wait was included before exposing the sample to the laser. The puck was centered using the internal camera. For cleaning, the power was increased to 27 %, requiring another 10 min of stabilization. The sample was then positioned at the center and irradiated for 10 min.

3.2 Nion Ultra STEM 100

The Nion Ultra STEM 100 electron microscope was utilized to assess the quality of the prepared samples, thereby determining whether the sample fabrication method was successful and met the required standards. Simultaneously, this technique was employed for sample mapping to precisely identify regions containing single layer, double layer, and multilayer graphene, as well as empty areas or contaminated regions. This comprehensive mapping was essential for later stages of the study, such as the identification of the irradiation effects. Correcting aberrations in a STEM is a highly complicated task. In the Nion UltraSTEM 100, this is achieved using a sophisticated configuration of four quadrupole and three octopole electromagnetic lenses [38], which are designed to counteract the aberrations introduced primarily by the objective lens. The correction process begins by compressing the electron beam into a highly elongated elliptical shape (see Figure 3.2 b). This line-shaped beam is then subjected to an octopole field oriented along its major axis, which imposes a negative spherical aberration onto the beam. Following this, the beam is rotated orthogonally and again passed through a similar octopole lens to introduce additional controlled negative spherical aberration along the second axis. In the final step, the beam is rotated once more and reshaped back into a circular probe, now with minimized spherical aberrations. Executing this process requires precise, iterative adjustments, as each correction step alters the beam's shape and can introduce new aberrations. Therefore, accurate measurement of the aberrations is essential before and throughout the correction process. In order to characterize and quantify the aberrations, the ronchigram method is employed. In this technique, the beam is intentionally defocused and scanned over an amorphous region of the sample.

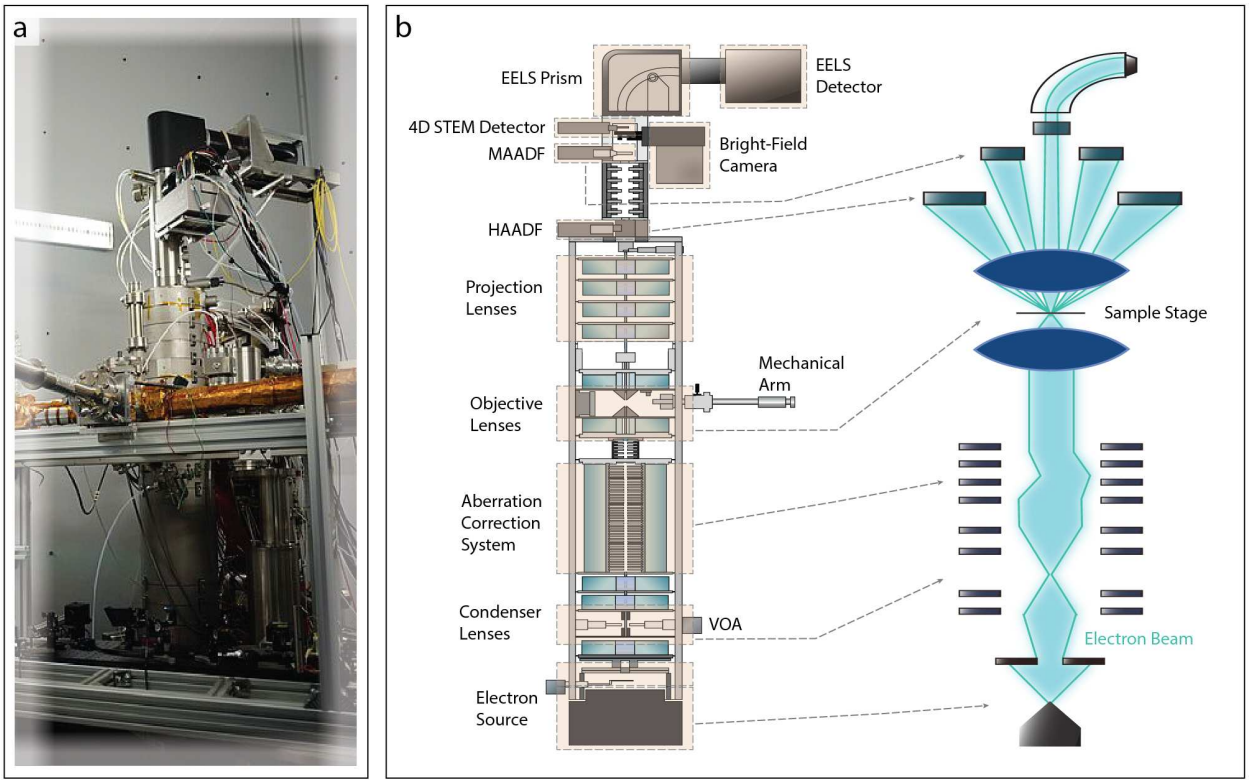

Figure 3.2: a) A photograph of the Nion UltraSTEM 100 microscope is shown alongside a schematic illustration highlighting its key hardware components and operating principles shown in the panel b). The microscope column is vertically oriented, beginning with the electron source located at the base. Above it are the virtual objective aperture (VOA), condenser optics, and the aberration correction system. The objective lenses are positioned around the sample region, where specimens can be inserted either manually using a mechanical arm or automatically via an integrated sample loading system. During operation, the electron beam interacts with the sample and is subsequently guided by the projection lenses toward the detection systems. Electrons scattered elastically are collected by the medium- or high-angle annular dark field detectors (MAADF or HAADF), while inelastically scattered electrons are directed to the bright field detector or to the EELS spectrometer mounted at the top of the microscope column. Based on Ref. [38].

The resulting interference patterns, or ronchigrams, are recorded using a charged coupled device (CCD) camera. From these images, local magnifications and distortions are extracted, allowing the reconstruction of the beam's aberration function [70, 71]. The entire procedure is automated and controlled using advanced software algorithms that precisely tune the electromagnetic lenses. These iterative corrections ensure the formation of a near-ideal probe, which is essential for achieving atomic-scale resolution in STEM imaging and spectroscopy.

3.2.1 Detectors

For low-magnification imaging, the On-axis Ring Camera (ORCA) was used for sample mapping and identification of SiN grid holes, enabling better orientation within the sample. The integrated software Autotune method was used for automated microscope tuning. At high magnifications, the Medium Angle Annular Dard Field (MAADF) detector was used, as well as High Angle Annular Dark Field (HAADF) and EELS detector. This instrument is equipped with a customized objective lens and a specially designed sample stage that integrates seamlessly with an ultra-high vacuum (UHV) system. MAADF detector is responsible for covering scattering angles between 60 and 200 milliradians, and HAADF detector is operating in the 80 to 300 milliradian range. EELS is performed using a Gatan spectrometer in combination with an Andor iXon Ultra 897 electron-multiplying CCD camera, allowing for sensitive detection of inelastically scattered electrons. The electron source is a high-brightness cold field emission gun (CFEG) operated at up to 100 kV, providing a highly coherent and monochromatic beam. The microscope is equipped with a third-generation $C3/C5$ aberration corrector, enabling the formation of a probe as small as 1.0 to 1.3 $\mathring{A}$ at accelerating voltages between 60 and 100 kV. The system operates under ultra-clean vacuum conditions, with a base pressure in the range of 10^{-11} to 10^{-10} mbar at both the electron gun and the sample. This pressure is approximately two orders of magnitude lower than that of most standard commercially available STEMs, allowing for extended high-resolution imaging with minimal sample contamination or degradation.

Following the cleaning process, STEM was used to evaluate the state of the samples after heating and laser-based cleaning. Since the initial mapping has been performed beforehand, it was possible to revisit the exact same regions and positions, allowing for a direct comparison of the sample's condition before and after cleaning. Additionally, after the irradiation, conducted after the cleaning process, the samples were reintroduced into the microscope to analyze the irradiation-induced effects. Since the imaging process is live and digital, the histogram can be adjusted to filter specific spectral components from the image, thereby improving contrast and enabling more accurate interpretation of the observed structures.

Furthermore, Fast Fourier Transform (FFT) analysis was used not only for structural characterization but also for fine-tuning the microscope settings. FFT patterns were crucial in identifying graphene stacking configurations: a monolayer displayed six distinct FFT points, whereas a bilayer exhibited twelve points. The relative position and angular orientation of these points with respect to the center of the spectrum directly correlated with the rotational misalignment between

the two graphene layers. The Gaussian filter, typically applied for smoothing images, played a particularly important role at extremely high magnifications. At these scales, the signal becomes challenging to interpret with the naked eye due to noise and distortions. Applying a Gaussian filter in this context enhanced structural clarity, allowing for a more precise sample visualization.

It is important to note that sample cleaning can only be performed up to a certain extent, and a residual level of contamination is always present, albeit significantly reduced after cleaning. However, an additional challenge arises from mobile contamination, which, although not always present, can occur during microscopy. This manifests as the accumulation of hydrocarbon deposits precisely at the location where the electron beam interacts with the sample, thus hindering the imaging process.

As part of the Nion Ultra STEM 100 microscope, an EELS detector is integrated, allowing this type of material characterization to be performed simultaneously during the microscopy session. Following irradiation, when it was determined that the structure of the bilayer graphene had changed, specifically, that clusters of high-contrast objects were now present in regions previously occupied by a clean bilayer graphene surface, EELS was applied to identify the nature of these new elements. To ensure that these elements were distinct from contamination and graphene, EELS analysis was also conducted in these regions.

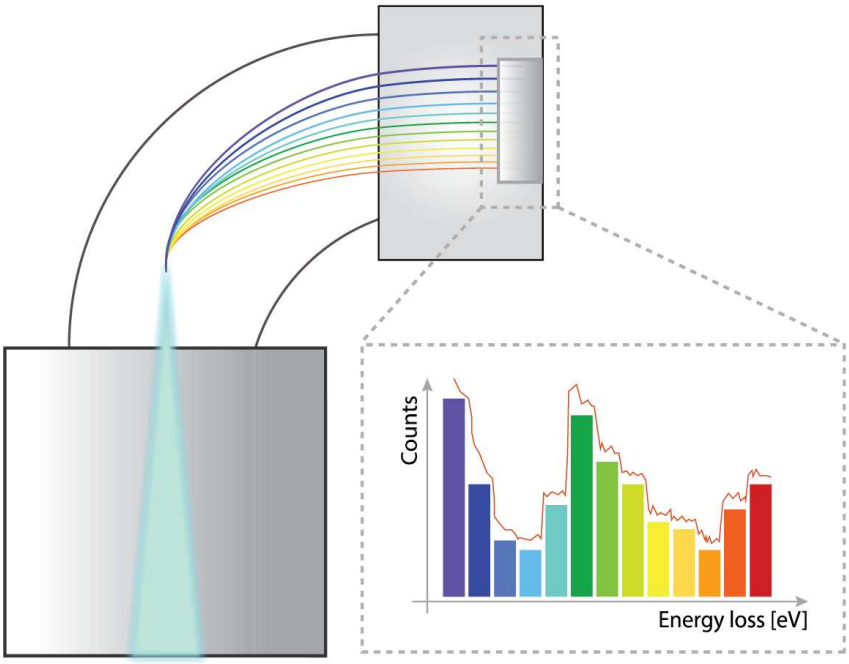

Figure 3.3: Illustrative representation of an electron energy loss spectrometer. As electrons exit the sample, they are dispersed by a magnetic field based on their kinetic energy: higher-energy electrons are deflected less (here shown in purple), while lower-energy electrons are deflected more (shown in red). By adjusting the magnetic field strength, the beam can be shifted vertically to target electrons with specific energy losses. To examine particular spectral features the beam can be further spread and focused using a selection magnet in combination with electron optics. This allows a chosen portion of the spectrum to strike a fluorescent screen, which is recorded by a CCD camera.

STEM EELS enables elemental and bonding analysis at atomic resolution by measuring the energy lost by electrons that undergo inelastic scattering in a sample. These electrons pass through the central hole of the annular detectors and are deflected by a magnetic prism, which acts as a spectrometer.

In the prism, electrons follow circular paths whose radii depend on their velocities (and hence energies), as determined by the Lorentz force given by equations 2.36 and 2.37. Electrons with different energy losses are spatially separated and projected onto a fluorescent screen, forming an energy-loss spectrum recorded by a CCD. The setup allows tuning of the magnetic field to focus on specific energy regions and magnify spectral features. Despite its power, EELS interpretation is complex. Reference atlases or simulations are often used to identify core-loss edges and fine structures [72]. Spatially resolved maps can be constructed by acquiring a spectrum at each

pixel, revealing local composition and bonding. The resolution is limited by the probe size and the instrument's energy resolution (~0.1 eV). Most electrons do not lose energy and contribute to the zero-loss peak, whose finite width (perfect condition is ~0.4 eV spread, 0.3 eV in ideal optical system) limits sensitivity to low-energy excitations like phonons.

3.3 Ion Irradiation

The ion irradiation method in this experiment involves irradiating graphene samples with xenon ions. SPECS Plasma source is connected to the CANVAS system, and contained within the target chamber, where laser cleaning of the samples is also performed (see Figure 2.3). This part of the experiment consists of two aspects of experimental practice, where one is a hands-on practical component involving work with the physical setup, while the other involves computer-programmed commands. Both parts are interconnected and dependent on each other. Assuming that the target chamber has already been cleaned or that experiments involving oxygen or xenon were recently conducted, the experiment can proceed. If this is not the case, it is necessary to clean the setup using oxygen plasma. Setup preparation involves attaching the xenon mini-can to the designated location, after which the valve system is used to allow the flow of xenon from the mini-can into the target chamber. Through this process, it is ensured that the volume between thee mini-can and the target chamber is filled exclusively with xenon and that no other unwanted gases are present, at the pressure of around 10^{-8} mbar. Using the mechanical arm, the puck is placed into the puck stage. After that, the deceleration setup is retracted outside of the plasma source beam's range, as the next step involves ignition and stabilization of the plasma. By monitoring the pressure gauge for the target chamber, the large valve next to the xenon mini-can is slowly opened until the gauge reads between 6 and $8 \cdot 10^{-6}$ mbar. When the pressure remains stable within this range for about 10 min, it is safe to start the plasma. This is done by igniting the plasma by setting the magnetron current to 16 mA, after which a light turquoise glow appears in the mirror at the bottom of the target chamber, indicating that the plasma source has been successfully ignited. For xenon gas, plasma stabilization takes approximately 20–25 min.

The laboratory setup of the plasma source and deceleration setup allows multiple measurements to be conducted at different positions within a single target chamber without the need to remove the sample from the entire system. However, repositioning the deceleration stage would require the sample to pass beneath the plasma source, which could introduce unwanted effects and com-

promise the experimental objective. To prevent this, the setup incorporates biasing a system that delivers an electric potential (usually 500 V) to the puck, creating an electric field stronger than the plasma beam itself in order to shield the sample. This step is performed before each position adjustment of the irradiation stage while the plasma source remains active.

The required measurements include beam profile measurements of the plasma beam itself, which provide insight not only into the source's intensity and energy spread, but also into its variations over time through repeated measurements. These measurements are conducted using a device known as a Faraday cup, which is a conductive metal device used to collect charged particles and measure the resulting current [41]. In this setup, it is employed to quantify the positive ion beam current generated by the plasma source. The cup is positioned directly in the beam path and features a 6.35 mm diameter aperture. A magnet positioned at the entrance deflects incoming electrons, ensuring that only ions contribute to the measured signal. Both the puck holder and the Faraday cup are linked to a power supply that allows them to be positively biased. Each irradiation experiment begins with the measurement of the xenon plasma beam profile. Once the successful ignition of the plasma is confirmed, the process of beam profile measurement is initiated. Through dedicated software, both the bias voltage applied to the Faraday cup and the resulting current generated from ion interactions with the cup's internal surface are monitored and recorded. The measurement begins by setting the Faraday cup bias to 0 V. The current produced by xenon ions is then measured as the bias is incrementally increased in 10 V steps, from 0 V up to 300 V. As expected, with increasing bias, the measured current gradually decreases. This trend results from the increasing electrostatic repulsion that filters out incoming ions, thereby reducing the number of ions reaching the cup. The relationship between the applied bias and measured current is visualized in Figure 3.4, where the blue data points represent the experimental measurements. The current is monitored as a function of applied voltage using a multimeter connected to the control unit of the deceleration stage.

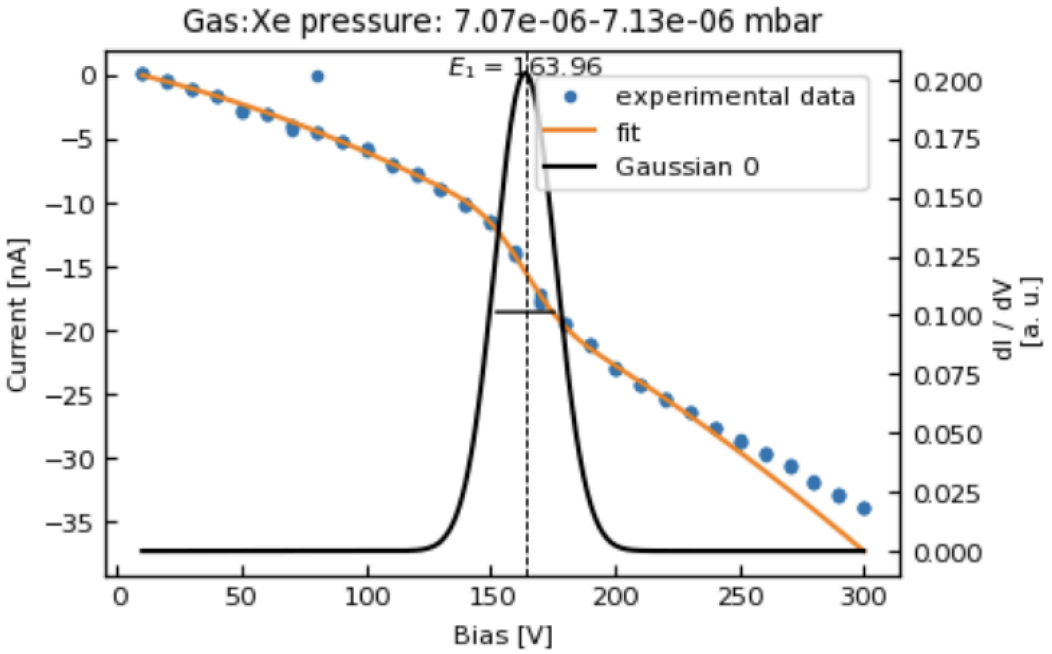

Figure 3.4: Beamprofile measurement of the xenon plasma. Dotted blue line is the data acquired by the Faraday cup and represents the relation between the generated current via impacting ions inside the cup and the gradually applied bias voltage to the cup. Orange line represents the polynomial fit of the gathered data. Black line is the Gaussian fit of the data, that is interpreted as the beam profile, with its μ representing the average energy of the ions (E_1 here). Data on top of the figure represent the pressure of the xenon gas inside the target chamber at the beginning and at the end of the beam profile measurement.

Notably, a sudden drop in current is observed around the midpoint of the curve, which marks the threshold where the bias voltage exceeds the average kinetic energy of most ions in the plasma beam. To better interpret these measurements, the data was first fitted with a polynomial curve (shown in orange in Figure 3.4) and subsequently with a Gaussian fit. This Gaussian distribution represents the actual beam profile that was used to guide the irradiation experiments. The peak of the Gaussian curve corresponds to the most probable ion energy, i.e., the energy carried by the largest fraction of ions within the beam. The left side of the distribution contains ions with lower energies, while the right side includes the high-energy tail of the beam.

Additionally, Figure 3.4 displays a horizontal black line indicating the standard deviation, σ, of the energy distribution. This σ value plays a central role in determining the biasing conditions for each irradiation experiment. Based on the measured beam profile, each subsequent irradiation step is planned by selecting an appropriate energy level, expressed as a position relative to

the beam's mean energy and its σ. This provides the means of tuning the ion beam energy by adjusting the applied bias voltage. Data measured by the Faraday cup is plotted and fitted using Gaussian distribution, as shown in the Figure 3.5.

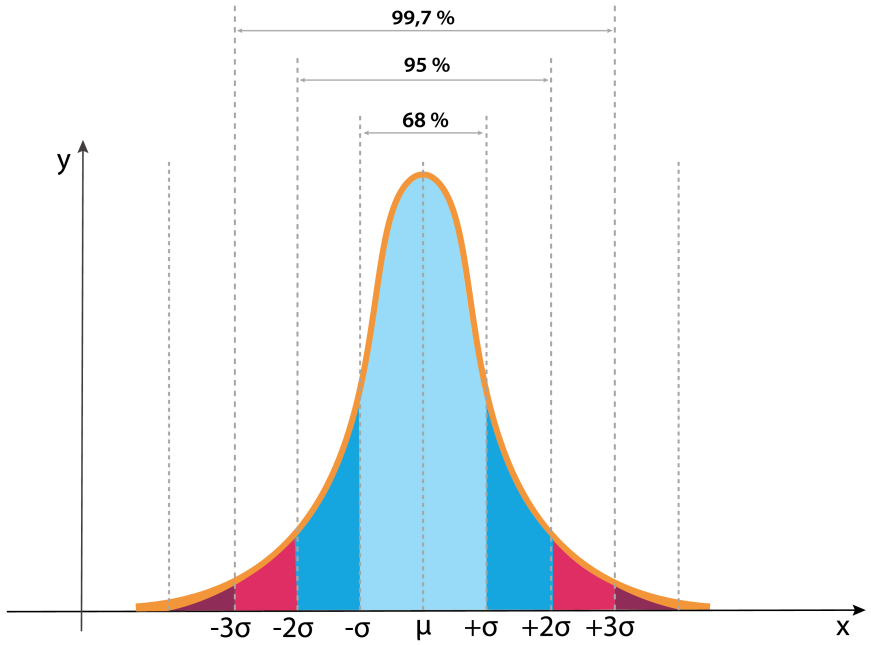

Figure 3.5: Illustration of a Gaussian (normal) distribution, center at the mean value μ. Symmetrically arond the mean, colored regions correspond to intervals of one, two and three standard deviaitons σ from the mean. The area between $\mu \pm \sigma$ encompasses approximately 68%, $\mu \pm 2\sigma$ cover about 95% and $\mu \pm 3\sigma$ about 99,7% of the distribution.

Based on the results of energy of the ions present in the plasma beam, and depending on the experimental objective, the appropriate electric current intensity, and usually as a fraction or multiple of the standard deviation of the energy distribution, is determined and applied for biasing the puck once it is positioned directly beneath the plasma source. Once the sample is positioned under the plasma source, ion plasma irradiation begins, and is lasting 12 min for each experiment. Afterward, the biasing voltage of the puck is returned to 500 V, and the deceleration stage is placed back to the Faraday cup position for an additional control measurement of the plasma beam's intensity and shape to confirm its stability after irradiation. The experimental phase concludes with turning off the plasma source and sealing the xenon mini-can. The effects and overall success of the experiment are then verified by electron microscopy. If no significant effects are observed, such as xenon implantation or the formation of defects in single or double layer graphene, the sample can be reused for further irradiation.

Chapter 4

Results and Discussion

4.1 Sample Preparation and Data Analysis

Regarding the general results, beginning with the success of sample preparation, it was confirmed that the fabrication method used for all six samples proved to be highly effective. This was validated by the presence of both single and double layer graphene regions in every single specimen. Furthermore, the laser cleaning technique and the cleaning by heating method both demonstrated excellent effectiveness. They enabled the formation of large, atomically clean regions across the samples, making them suitable for further experimentation. These outcomes confirm that both cleaning approaches described in the Methods section of this work are reliable, sufficient, and reproducible for conducting the experiments presented here.

The data analysis process was carried out in multiple stages and using several different approaches. The microscope itself is operated via a software called NionSwift, which allows for simultaneous imaging and initial data processing. One of the integrated processing tools is the FFT, a mathematical technique used to convert spatial data into frequency space. In microscopy, FFT helps reveal periodic features in the image, such as crystal orientations and lattice structures. This form of real-time processing enables the identification of sample regions based on their layer configuration, like for example, areas covered by single, double, or multilayer graphene. The characteristic diffraction spot patterns visible in the Fourier-transformed images help distinguish these regions and provide insight into the orientation and stacking of the graphene layers. Another essential tool in the analysis workflow is the histogram, which graphically represents the distribution of pixel intensities in an image. By manually selecting specific intensity ranges

from the histogram, users can isolate regions of interest or exclude irrelevant areas from further analysis. Due to the inherently noisy nature of the raw STEM data, applying a Gaussian filter is particularly beneficial. This filter works by averaging pixel values with their neighbors in a way that gives more weight to central pixels, effectively reducing high-frequency noise while preserving overall structure. The combination of FFT analysis, histogram selection, and Gaussian filtering results in a cleaner, more interpretable image suitable for precise investigation.

Another key component of the data analysis involved processing the acquired images using self-written Python scripts. One recurring issue encountered with the NionSwift software is its tendency to incorrectly assign the image scale bar. As a result, it becomes necessary to retrospectively calculate the true scale of each image based on the observed structures. This can be done manually by leveraging known atomic distances in graphene. By comparing this known carbon atom spacing to the number of pixels separating the same atoms in the image, one can determine the spatial resolution. However, to streamline the process and apply it consistently across multiple images, a Python script was written to perform these calculations automatically. The program begins by calculating the FFT of the image, which provides information about periodicities in the sample. It then locates high-intensity peaks in the FFT pattern, specifically the zero and first-order diffraction peaks. This pixel distance is then used to determine the real-space sampling of the image. The calculation uses a known reference distance in graphene: 0.213 nm, which corresponds to 3/2 times the carbon-carbon bond length (0.142 nm). By dividing this known real-space value by the measured pixel radius in the FFT, we obtain the sampling resolution in nm per pixel. Finally, the full field of view (FOV) in nanometers is calculated by multiplying the sampling resolution by the total width of the image in pixels.

An important component of this work was the use of EELS, which played a crucial role not only in confirming that the synthesized material was indeed graphene, as shown in Figure 4.1, exibiting a peak at around 280 eV, which corresponds to carbon K-edge [72], but also in identifying features observed after xenon irradiation that appeared structurally different from both atomically clean graphene and contaminated areas.

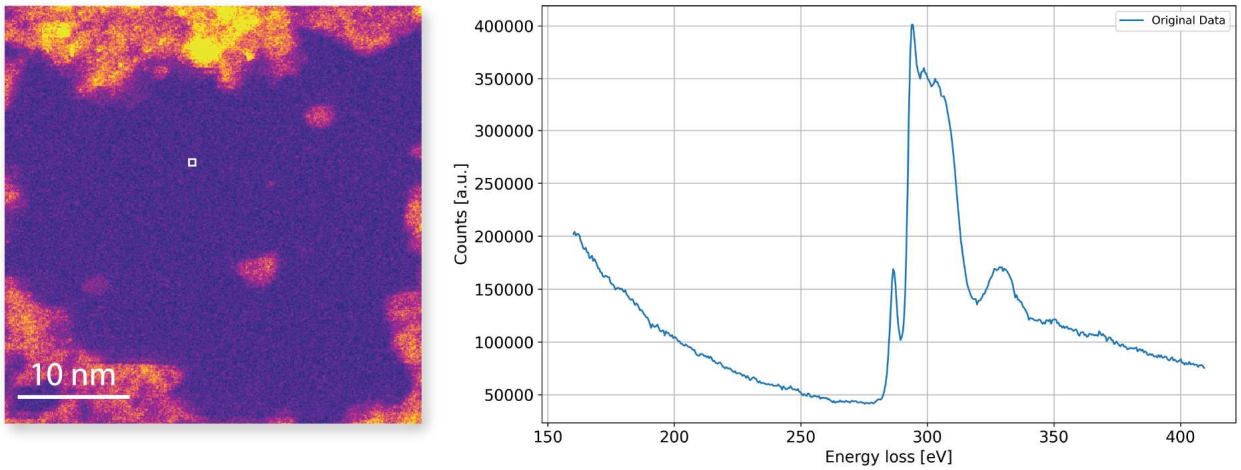

Figure 4.1: Double layer graphene and its EEL spectrum. Left: Color-adjusted double layer graphene sample micrograph, visualized using ”Plasma” lookup table in Fiji to enhance intensity contrast and highlight structural features. White rectangle representing the probe position at which the EEL spectrum was recorded. Right: EEL spectrum from the position shown on the left panel (blue line).

EELS enabled the verification that these structures were in fact xenon clusters [72], confirming successful xenon implantation, as shown in Figure 4.2 with peaks showing at around 700 eV, which corresponds to xenon $M_{4,5}$ edge [72], proving the effectiveness and specificity of the implantation process.

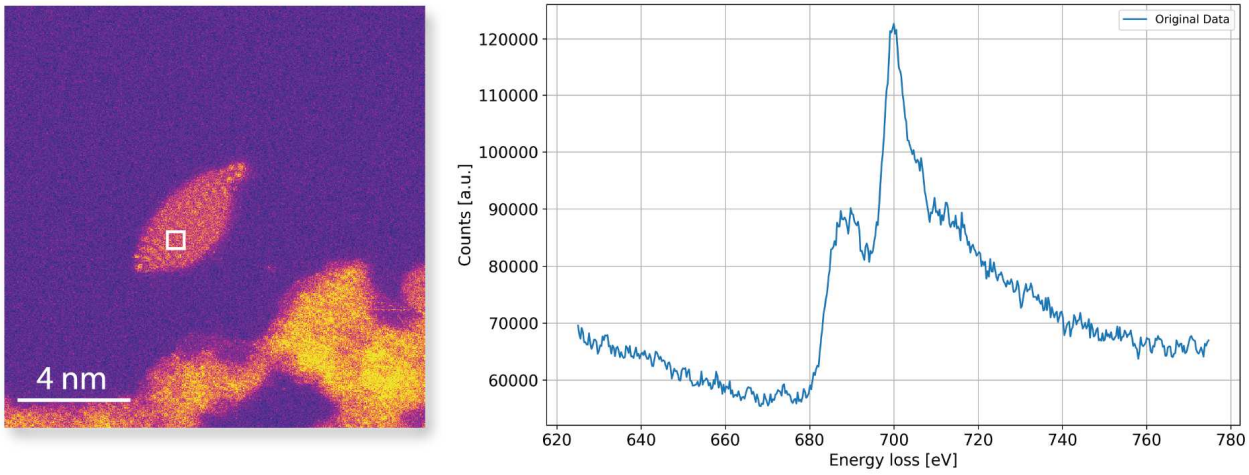

Figure 4.2: Xenon in double layer graphene and its EEL spectrum. Left: Color-adjusted double layer graphene sample with implanted xenon cluster micrograph, visualized using ”Plasma” lookup table in Fiji to enhance intensity contrast and highlight structural features. White rectangle representing the probe position at which the EEL spectrum was recorded. Right: EEL spectrum from the position shown on the left panel (blue line).

This work also investigates the implantation density of xenon atoms in double layer graphene. To perform this analysis accurately, it is essential to determine the exact surface area of atomically clean graphene within the observed field of view. For this purpose, a modified version of a Python script, originally developed by a colleague from the research group, was used [69]. The script builds upon the previously calculated FOV and performs a detailed analysis of the intensity histogram of the image. The core idea is to distinguish atomically clean regions of graphene from those containing surface impurities, i.e., contamination. This is achieved using a custom region-selection method based on pixel intensity and thresholding. By analyzing the histogram, specific intensity ranges associated with clean graphene are isolated, while higher or lower intensities, that are typically indicating foreign atoms or amorphous contamination, are excluded, which is shown in Figure 4.3.

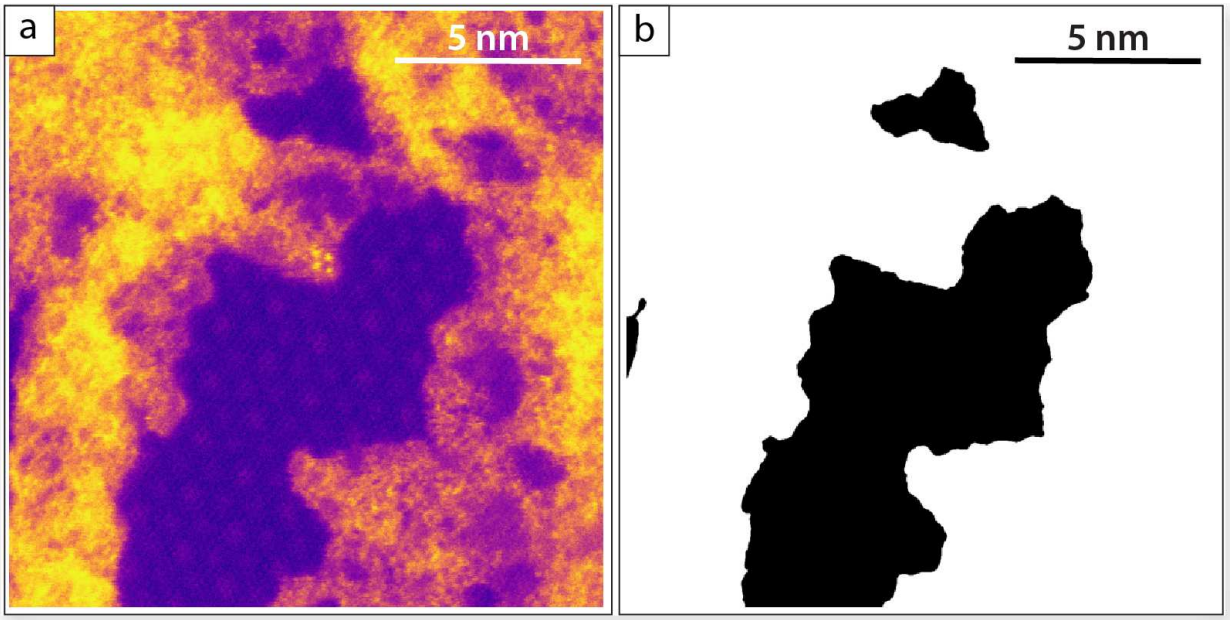

Figure 4.3: a) Color-adjusted micrograph, visualized using the ”Plasma” lookup table in Fiji to enhance intensity contrast and highlight structural features; b) Corresponding binary mask generated from the image in panel (a), where atomically clean regions are shown in black and areas identified as contamination are shown in white.

As shown in the figure, the code has been modified and refined to account for intensity variations coming from the moiré pattern. These features are correctly interpreted as part of the clean graphene surface rather than mistakenly classified as contamination. Additionally, this code showcases another capability, and that is detection xenon clusters embedded within clean regions. Since these clusters are implanted between the graphene layers, the area they occupy is identified and excluded from the calculation of atomically clean surface area. Once the clean

areas have been identified, the program counts the number of pixels that correspond to these regions. Then, it compares this value to the total number of pixels in the image. Given that the physical dimensions of the image in nanometers are already known from the FOV calculation, the script calculates the surface area of clean graphene in each image.

The self-written Python code developed for the data analysis proved to be a highly effective and reliable tool. Throughout the course of this research, the code underwent numerous improvements to ensure it is properly adapted for accurate and consistent analysis. For its fine-tuning, a diverse set of reference images was used. These included examples with various types of moiré patterns, a wide range of xenon cluster sizes and shapes, and different distributions and dimensions of clean graphene areas. These images were fed to the code, and the output was manually verified to determine whether the defined principles of the program functioned as intended. For images containing clearly defined, large, and easily recognizable clean areas, the code performed as it should and returned accurate results. These well-structured regions served as the benchmark to evaluate whether the code behaved reliably. However, challenges did arise, and in many cases, alongside the large clean regions, there were smaller clean areas hidden within heavily contaminated areas. These were not recognized by the initial versions of the code, but thanks to continued refinements and iterative testing, the updated code eventually managed to correctly classify and include even these small clean areas in the analysis, as shown in Figure 4.4.

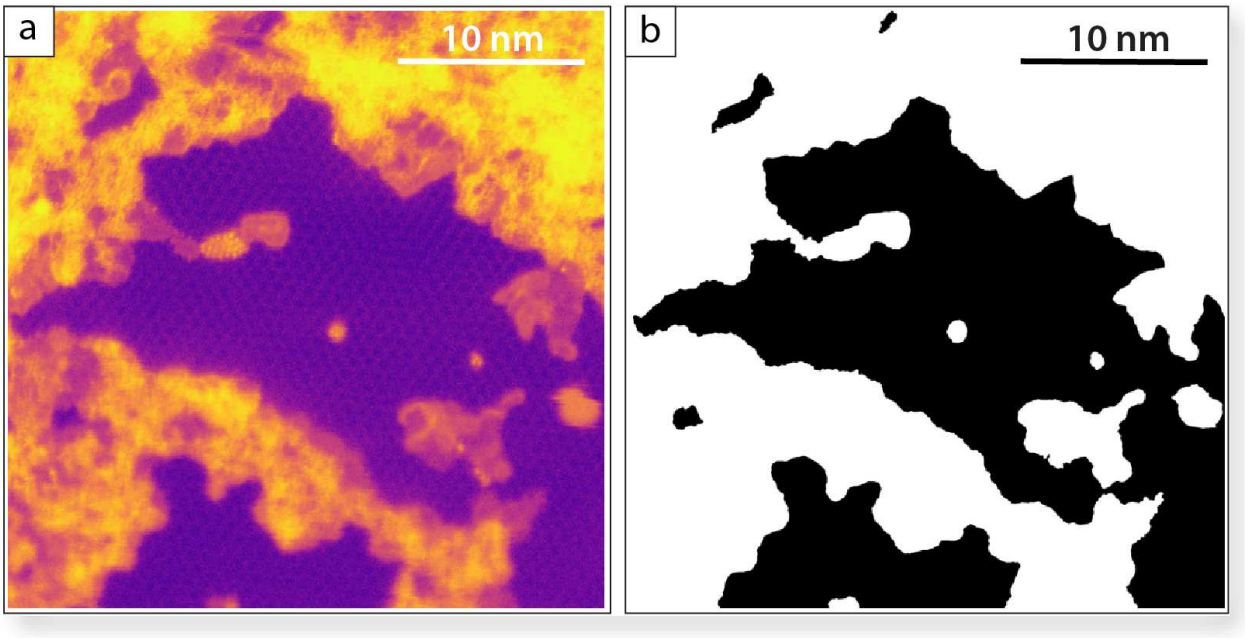

Figure 4.4: a) Color-adjusted micrograph, visualized using the ”Plasma” lookup table in Fiji to enhance intensity contrast and highlight structural features; b) Corresponding binary mask generated from the image in panel (a), where atomically clean regions are shown in black and areas containing xenon clusters or identified as contamination are shown in white.

This significantly enhanced the accuracy of the data and provided a more realistic representation of the percentage of clean pixels present in each image. Identifying xenon clusters, however, presented an additional difficulty. Two key problems were encountered. First, some clusters that were visibly apparent by eye, especially those located beneath light contamination, were not detected by the code. Second, very small clusters, consisting of just two or three atoms, were detected but incorrectly categorized as contamination. Although these specific cases do not affect the surface area calculations directly (since xenon clusters are not counted as clean surface), they do have implications for implantation density calculations. This is because the clusters, whether located in clean areas or beneath contamination, still exist within the double layer graphene and therefore influence the interpretation of how densely xenon atoms are implanted. That said, as more and more samples were analyzed using this method, and the amount of reference data grew, the code's performance improved steadily. It became increasingly evident that the results were converging toward a more accurate reflection of reality. Moreover, clusters located within or on the edges of contaminated regions were explicitly excluded from the implantation density calculations. In conclusion, this custom Python code has proven to be a very useful tool for estimating clean graphene surface areas with high precision. While it may not be fully suited for detailed atom-by-atom counting or precise identification of every xenon cluster, particularly

those partially covered or extremely small, it nonetheless provides valuable data that support the main conclusions of this thesis. With further refinement, its functionality could potentially be expanded, but even in its current form, the tool significantly contributes to the reliability and clarity of the overall analysis.

4.2 Xenon Ion Irradiation

At the beginning of the experimental work, it was initially assumed that data analysis and particularly the task of accurately identifying and counting individual atoms and clusters, would be assisted by some form of computer-based support, such as neural networks. However, it was soon realized that no existing neural network or automated tool is currently reliable enough to handle the complexity of this specific task. Xenon clusters exhibit significant dynamic behavior, including movement, shape transformation, and interactions with their surroundings, which makes them extremely challenging to track and analyze automatically. As a result, all data presented in this thesis, including those used for calculating derived quantities and for data representation, were obtained through meticulous manual inspection. Every atom and cluster was individually counted by hand from each recorded frame. To aid in this process, the study utilized a considerable number of image stacks, which proved essential in analyzing the dynamic behavior of larger and mobile clusters. These stacks allowed for close tracking of cluster movement, internal reorganization, and merging with other clusters, all of which contributed to a better understanding of their structure and minimizing errors during manual counting. In the case of large clusters, internal dynamics posed a particular challenge. Atoms that appeared stationary and clearly countable in one frame could become indistinct in the next due to motion or clusters' internal reconstruction. To address this, atom counts were taken from five different frames for each cluster, and the mean value was calculated to provide the most accurate estimation while minimizing the counting error.

Although the thesis clearly states which sample was prepared using which type of grid, no explicit categorization based on substrate type is applied in the composite data illustrations or in the analysis of derived quantities such as average implantation rate or implantation density. Moreover, the work does not aim to determine whether Quantifoil or SiN provides a better substrate. This is because successful implantation, along with the presence of high-quality single and double layer graphene regions and large atomically clean surfaces, was confirmed across both grid types.

Consequently, it can be concluded that the described experiments can be reliably conducted on either substrate. As mentioned earlier, statistical analysis was carried out using a combination of manual and semi-automated methods, depending on the specific goals of each analysis.

This thesis is based on data collected from six prepared specimens and represents a novel achievement, as well as an experimental and analytical approach never before successfully executed in this laboratory. Nevertheless, some figures, such as for example Figure 4.16 to 4.21, reveal varying numbers of collected data points, such as number of implanted clusters and atoms or created defects, across samples. This variability can be considered as an asset, as larger dataset generally leads to a smaller statistical error, which is particularly valuable in manual data collection, where some degree of human error is inevitable. To reduce this uncertainty, each cluster was manually counted at least three times, ensuring the highest possible accuracy and consistency across the dataset. While this method is undoubtedly labor-intensive, it is crucial for improving the reliability of the results. Although it cannot fully eliminate the possibility of counting errors, it significantly reduces their impact and reinforces the robustness of the findings presented in this work.

Essential component of the deceleration setup is the puck stage, which in this experimental configuration can be electrically biased. High biasing the sample (for example 500 V) serves as a protective mechanism, where by applying a certain voltage to the sample, all incoming xenon ions with kinetic energies lower than or equal to the applied bias are repelled and prevented from interacting with the graphene sample. This technique forms the basis for controlled irradiation energy during the experiments.

Approach to determining the threshold ion energy required for xenon implantation into double layer graphene involves an iterative process where the sample is irradiated with the specific ion energy interval, and if xenon implantation is observed, the following experiment is conducted at the higher limit of the ion energy interval. If implantation still occurs, the limit of the energy interval is further increased. On the other hand, if no implantation is detected, the lower limit of the energy interval is reduced. In essence, the method for locating the threshold energy relies on energy interpolation between successive irradiation steps. In this context, deciding which energy interval to apply in each irradiation experiment, as well as the size of the interpolation steps, is the key experimental strategy and refers to the electric potential applied for the biasing of the sample that sets the lower limit of the ion energy interval. Each experiment serves as a data point in narrowing down the energy range that defines the threshold. This brings forth an important

question: how can such a process be reliably executed in a system that is not perfectly stable, specifically, when using a plasma ion source whose beam energy distribution may fluctuate over time? The answer lies in the systematic measurement of the beam profile before and after every irradiation experiment. These measurements provide crucial information about the current state of the ion energy distribution within the plasma beam. They reveal not only the mean ion energy but also the shape and spread of the energy distribution at the time of the measurement. This is critical for ensuring that the biasing used in each irradiation step is accurately known and that any changes in the plasma source's performance are properly accounted for. By comparing beam profiles measured before and after each irradiation, it becomes possible to assess whether fluctuations in the energy distribution are moderate ($\Delta\sigma < 25$ eV) or substantial ($\Delta\sigma > 25$ eV). If the changes are minor, they can be considered insignificant, and the corresponding irradiation data can be treated as reliable. However, if the beam profile varies considerably, this indicates instability in the plasma source, and the experimental results must be interpreted with caution. The solution lies in the standardization offered by the σ values of the Gaussian energy distribution, which the beam profile follows. In order to make sure that this method is consistent and independent from the shape of the energy distribution at any time, interpolation steps were defined using multiples of the σ of the underlying Gaussian distribution, rather than fixed voltage intervals, as in that way each biasing value corresponds to the same statistical weight. By applying a bias at a given multiple of σ (for example, -1σ, +2σ), the distribution is truncated at that point. As a result, the distribution of ion energies is altered, and the mean of the distribution shifts toward lower value. In some cases, μ shifts below zero, although only ions with positive energies (lower value of the interval of the ion energies is at 0 eV) are expected to interact with the sample. Figure 4.5 shows how determining the energy interpolation steps based on the multiples of the σ and biasing the sample at these values alters the energy distribution of ions, as well as which part (energy interval) of the ion energy distribution is expected to correspond to the ions that interact with the sample.

What the first panel in the top portion of Figure 4.5 shows is the irradiation experiment, where after the beam profile was measured, it was decided to bias the sample at the value of 0 σ of the energy distribution, meaning that the bias voltage was set to the mean energy value of the Gaussian distribution. This means that it was expected that ions with energies less than μ=0 were repelled, while only those with positive energies would reach and interact with the graphene sample. The right portion of the Figure4.5, showcases that applying a bias of 200 V, which corresponds to approximately the value of 3σ of the energy distribution, would fully shield the sample

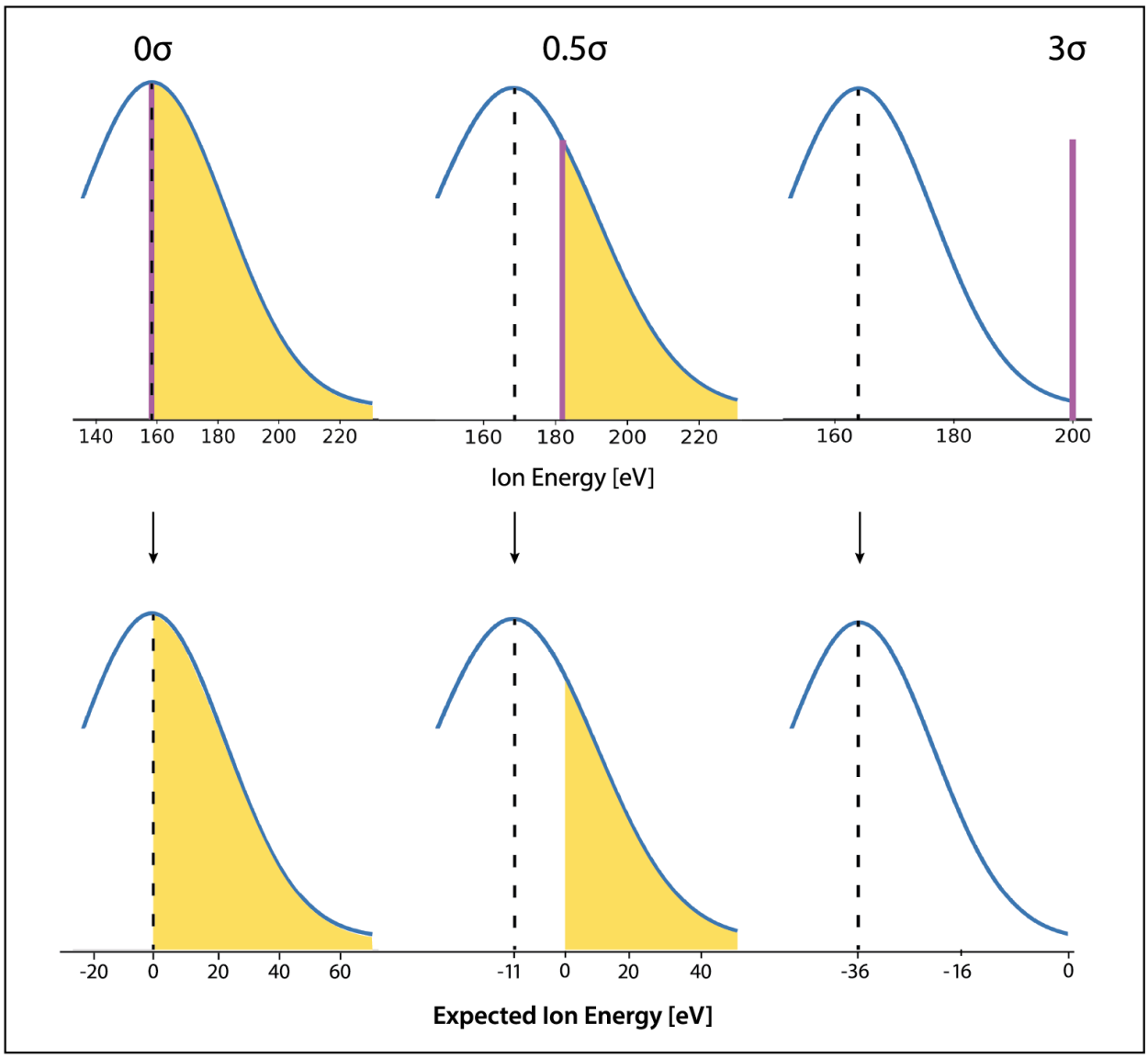

Figure 4.5: Top: Plots show plasma beam profiles with different σ cut-off values. Blue line represents the beam profile, dotted black line the μ of the energy distribution, and vertical purple line shows the biasing (σ cut-off) value. Bottom: After applying the biasing, the energy distribution is shifted for the value of the bias. Previous μ of the distribution now has the value of μ–bias, and previous biasing value now represents the lower limit of the energy distribution interval of the ions reaching the sample. Yellow area represents distribution of positively charged ions and their energies that are expected to interact with the sample.

from the plasma beam, as the shift of the energy distribution after biasing leaves about only 0.3% of energy distribution interval with ions that could interact with the sample. On the other hand, applying 0 V bias exposes the sample to the entire ion energy distribution, as it was done with Sample F and can be seen in Figure 4.21 c.

Presented here, in Figure 4.5, are beam profiles that differ in style from those shown in Figure 3.4. This variation is intentional, as the graphs result from the analysis and calculation of a specific quantity describing the number of ions reaching the sample per unit time under various biasing conditions. This quantity, referred to as ion flux and expressed in ions per second, is derived by integrating the Gaussian distribution of the beam from the applied bias voltage (lower limit) to infinity (upper limit) and normalized by

$$\frac{1}{\sqrt{2\ \pi\ \sigma^2}}\ , \tag{4.1}$$

which accounts for the normalization of the distribution in this interval. Beam profile is obtained by relating the current produced by ions (measured in nA) against the ion energy (in eV), thus integrating this function over the defined energy interval yields the total integrated ion signal, with units of nA eV. To obtain the ion flux for singly charged ions, this integrated value is converted using the relation between electric current, the elementary charge, and time, where eliminating the elementary charge yields the ion flux value in units of number of ions per second. This ion flux is essential for obtaining the dose, which is defined as the relation between the ion flux, aperture area of the Faraday cup, and irradiation time, where differences in distances between the plasma source and Faraday cup, and plasma source and puck stage must be taken into account. Dose represents the number of ions interacting with the sample per area.By knowing this, any observed variation in implantation behavior can be attributed solely to ion energy, and not to differences in ion quantity. Normalization of acquired data using ion flux allows for recalculation of implantation rates as if all samples had received the same number of incident ions, but with different kinetic energies. This approach is critical for evaluating the impact of energy on implantation efficiency. Assuming constant irradiation time, the dose is considered unchanged even when the ion energy distribution is truncated by biasing at different values of the beam profile. Table 4.1 shows samples and corresponding doses they were irradiated with.

Table 4.1: Samples and their corresponding irradiation doses.

	Sample A	Sample B	Sample C	Sample D	Sample E	Sample F
Dose $[\frac{ions}{cm^2}]$	0	$5.81 \cdot 10^{10}$	$1.48 \cdot 10^{13}$	$1.77 \cdot 10^{13}$	$2.48 \cdot 10^{13}$	$3.12 \cdot 10^{13}$

As shown in the Table 4.1, the dose for the Sample A is 0 ions cm^{-2}, which is actually expected since no ions should reach the sample under the biasing of 500 V. For the Sample B, with a biasing of 200 V, a significantly lower dose, with three orders of magnitude lower compared to the other four doses, is observed, which aligns with theoretical expectations. For the remaining

four samples, the doses are of the same order of magnitude. However, as it can be seen from the subsequent data, implantation still occurred even at a dose of 0 ions cm $^{-2}$.

Data analysis revealed an unexpected trend, i.e., the number of implanted xenon atoms and clusters within the double layer graphene increased with increasing values of the lower limit of the ion irradiation energy interval. To investigate the discrepancy, a series of control experiments was conducted. These included repeated beam profile measurements to monitor the stability of the plasma source and rule out short-term, high-amplitude fluctuations in the energy distribution that may have gone undetected during irradiation. After confirming the beam profile's stability over time, the focus of the control experiments shifted to testing the reliability of the sample biasing system. A sample bias of 500 V, corresponding to complete repelling of the ion beam, was applied with the intention to fully block all incoming ions and verify the absence of implantation. The plan was then to gradually decrease the biasing value in small steps until xenon implantation was first detected. While this stepwise approach was considered at the start of the project, it was originally dismissed due to its labor-intensive nature and material resources. However, in light of the anomalous results, this method was reconsidered. Biasing value that corresponds to 3σ of the previously measured beam profile is expected to block approximately 99.7% of the ion beam energy distribution. Given this, it was initially anticipated that xenon implantation would be negligible, which was not the case. Even under the highest possible applied bias of 500 V, xenon implantation was still observed in the double layer graphene. This led to the conclusion that the entire irradiation setup was malfunctioning. A final control experiment was performed under zero-bias conditions (0 V), allowing the full plasma beam energy to interact with the sample. As expected, this resulted in significant xenon implantation and also caused visible damage to both single and double layer graphene regions, thus validating the expectations. The results and comparative analysis of all irradiation and control experiments are summarized and visualized in the following graphs and tables.

Throughout the data analysis process, it became clear that categorizing xenon clusters, particularly by size, i.e., the number of atoms composing them, was essential. These clusters ranged from small formations consisting of just two to three atoms to very large aggregates containing up to approximately 140 atoms. As such, Figure 4.6 not only provides an introduction and overview of the diversity in cluster morphology but also serves as a visual reference guide for this thesis. It helps familiarize one with the various shapes and characteristics of xenon clusters, enabling easier recognition and classification in the following micrographs, even when individual clusters are not explicitly highlighted.

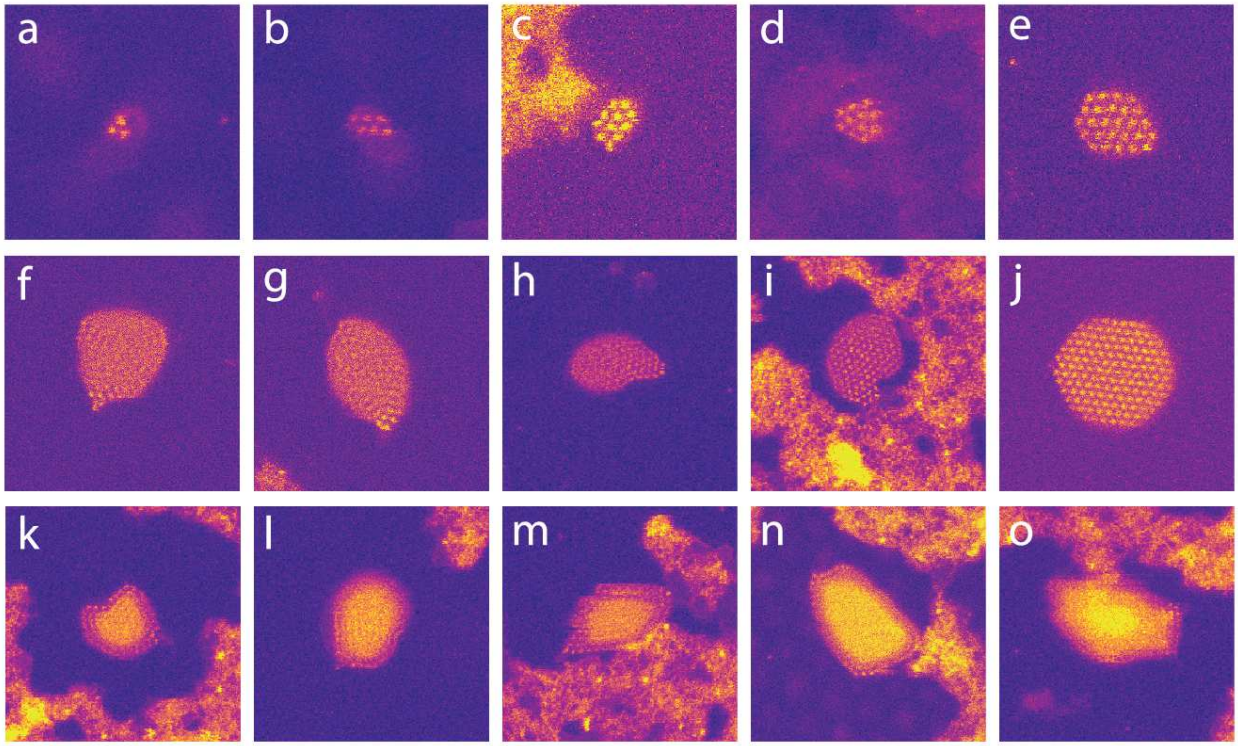

Figure 4.6: Different cluster sizes and formations. Images in panels (a)-(e) have an area of 4x4 nm^2, in panels (f)-(j) 8x8 nm^2 and panels (k)-(o) 10x10 nm^2.

In Figure 4.7, panels (a) to (c), show well-defined double layer graphene regions. However, these examples also demonstrate that even such regions do not always remain pristine throughout the entire course of the experiment. As shown in the images, mobile contamination can emerge and spread during imaging, significantly limiting both the effective imaging time and the overall capability for high-resolution observation. Although the speed and skill of the operator can still enable the acquisition of usable data, the presence of mobile contamination becomes a major obstacle when longer observation of a specific region is required, for example, to monitor the dynamic behavior of clusters over time. To mitigate this issue, a known technique called beam showering has been employed. This method involves focusing the electron beam on a region away from the intended area of observation for approximately 15 min. The aim is to attract and trap mobile contamination at that region, thereby minimizing its presence in the actual region of interest. While not always entirely effective, this approach can significantly reduce contamination-related disturbances during imaging. Despite the presence of mobile contamination, further cluster identification and classification were made possible through image enhancement techniques, particularly those applied using the ImageJ software. These processes helped distinguish between true contamination and the clusters of interest, even in suboptimal imaging conditions. Additionally, the Python code used in this work was capable of recognizing regions affected by mobile con-

tamination and classifying them separately from static contamination. This distinction enabled a more accurate analysis of truly clean areas on the sample, which were then used in subsequent surface area calculations and statistical evaluations. Regarding the general presence of contamination, one limitation of this microscopy method is the inability to determine which side of the double layer graphene the contamination resides on.

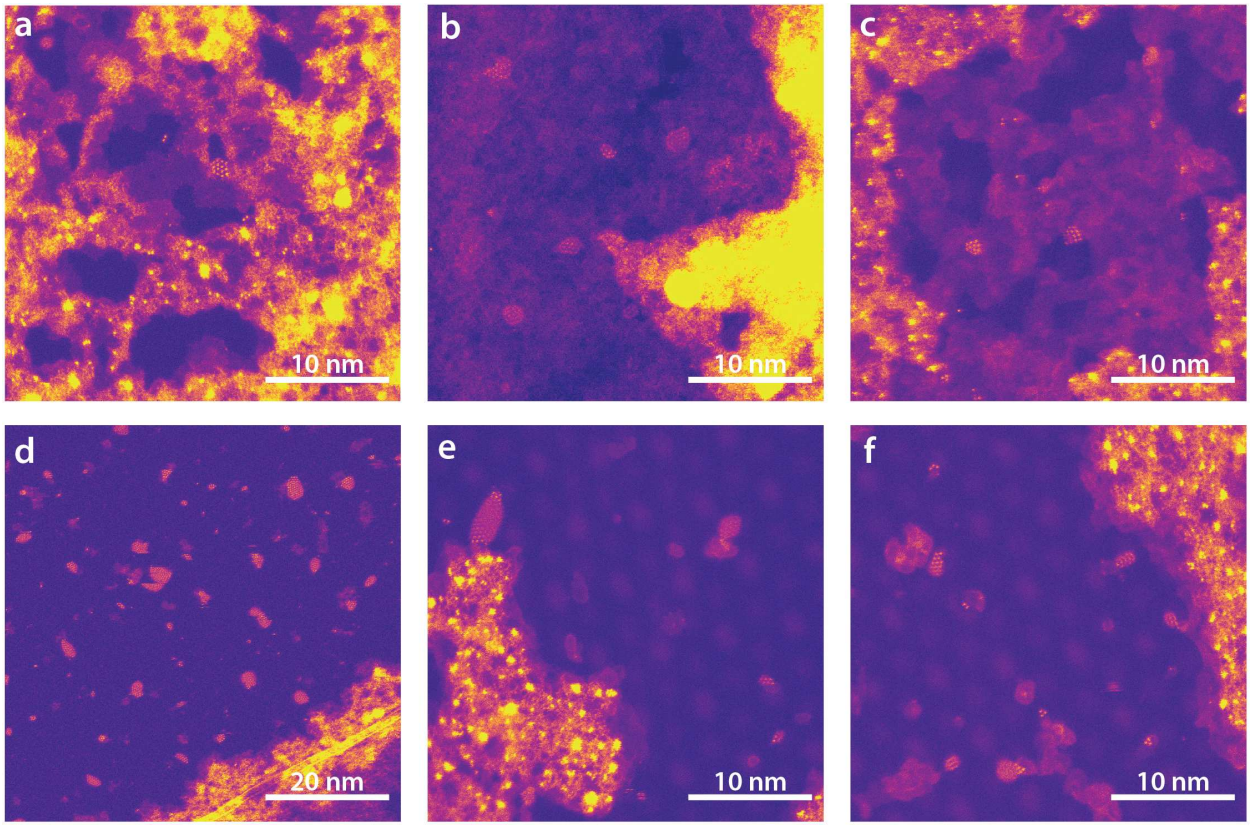

Figure 4.7: MAADF STEM micrographs of double layer graphene samples irradiated with xenon ions. The six panels correspond to different samples, with panel (a) corresponding to Sample C, panels (b) and (d) representing Sample B, and panels (c), (e) and (f) corresponding to Sample A corresponding to Sample E. All images are color-adjusted using the "Plasma" lookup table in Fiji to enhance intensity contrast and highlight structural and morphological features such as clean double layer graphene regions, xenon clusters, and contamination boundaries. The figure shows relatively small xenon clusters, each containing up to approximately 30 atoms, distributed across atomically clean regions. These clean areas are partially overlapped by mobile contamination, which remains distinguishable due to its lower intensity compared to typical static contamination at the time of imaging.

Since electron beam imaging interacts with the entire thickness of the sample, the depth resolution in this context is limited. Nevertheless, based on the observed movement of clusters through contaminated regions, it is concluded that contamination is situated on the exterior surfaces of

the double layer, whereas the xenon atoms are trapped within the van der Waals gap between the two graphene sheets.

Furthermore, Figure 4.7 presents six high-resolution images showcasing xenon clusters of relatively small size, generally containing up to around 30 atoms. These clusters are shown in their distinct two-dimensional form, where individual atoms are clearly resolved and easily countable, allowing for straightforward quantitative analysis. The figure highlights a broad distribution in both cluster sizes and implantation densities. This is especially evident in panel Figure 4.7 d, which features a high concentration of xenon clusters varying in size and spatial distribution. A notable characteristic of these clusters, already observable in these images, is their dynamic behavior. Xenon clusters exhibit significant mobility within gap of the double layer graphene, which complicates imaging and data analysis. The fact that even smaller clusters can move appreciably suggests that there is no straightforward correlation between cluster size and mobility or diffusion speed and pattern. Also visible in Figure 4.7 d, are individual xenon atoms and atomic pairs, which, although not quantitatively analyzed in this thesis, exhibit intriguing behavior. Their tendency to aggregate into clusters, as well as their interactions with neighboring atoms, pairs, or existing clusters, opens up a compelling path for future investigation. Understanding exactly how these isolated atoms contribute to cluster nucleation and growth could offer further insight into the mechanisms of noble gas behavior in 2D systems. In addition, Figure 4.7 d and f show distinct moiré patterns, confirming the presence of double layer graphene in these regions.

Figure 4.8 focuses on xenon clusters of intermediate size, i.e., containing up to approximately 80 atoms. Figure 4.8 a, shows signs of mobile contamination are again observed, despite the improved imaging conditions. Across Figure 4.8 a through d, the xenon clusters are shown to retain their two-dimensional character, with individual atoms still visibly resolved. Notably, despite the increased number of atoms compared to smaller clusters, these mid-sized clusters remain structurally flat and suitable for imaging. However, mobility remains an issue, even at this cluster size. The clusters exhibit motion within the double layer graphene, which poses challenges for consistent frame-to-frame analysis, as shown in Figure 4.9. More interestingly, observations also revealed instances of internal atomic reorganization within the clusters.

During these rearrangements, the atomic arrangement becomes temporarily less ordered, and the clusters may appear three-dimensional due to transient structural fluctuations. Nevertheless, by analyzing a sufficiently large number of frames, it was possible to resolve these events and accurately determine the total atom count in each cluster.

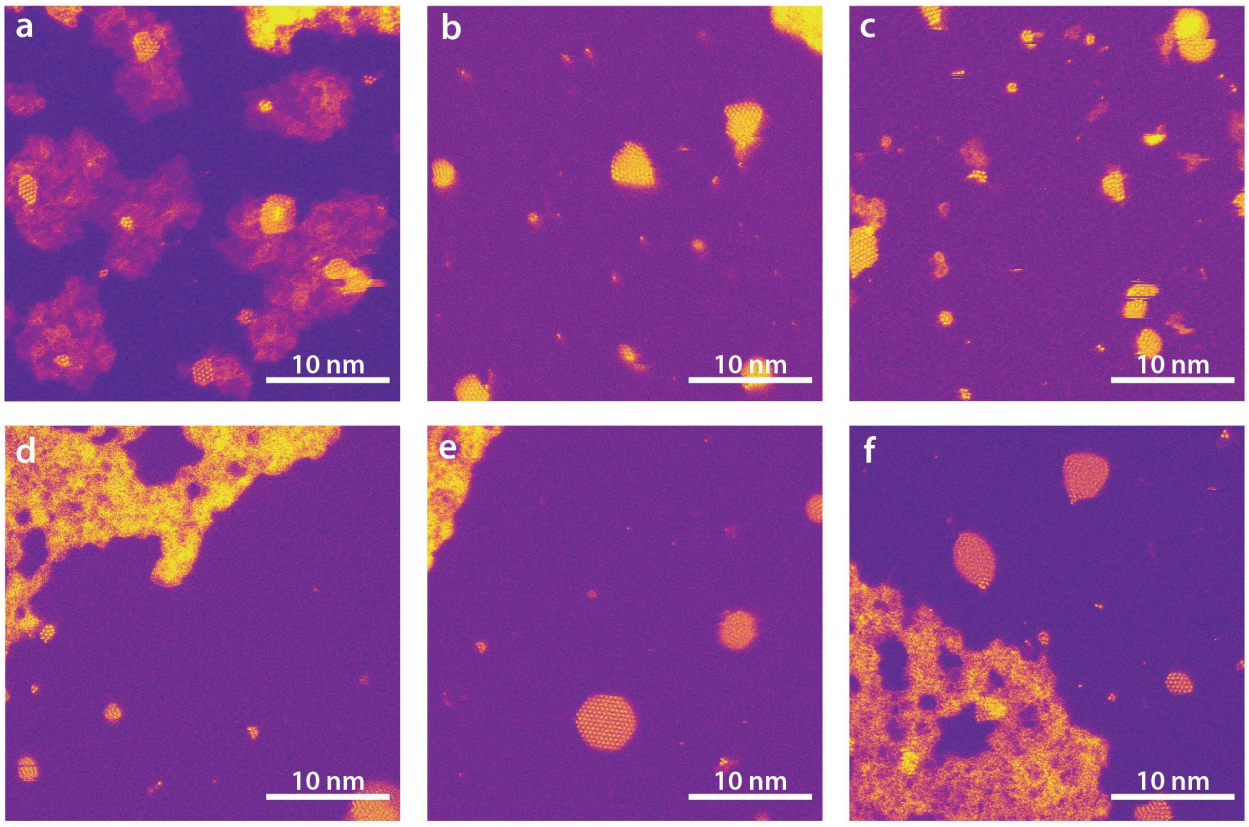

Figure 4.8: MAADF STEM micrographs of double layer graphene samples irradiated with xenon ions. All six panels correspond to Sample B. All images are color-adjusted using the "Plasma" lookup table in Fiji to enhance intensity contrast and highlight structural and morphological features such as clean double layer graphene regions, xenon clusters, and contamination boundaries. The figure shows the implantation of medium sized xenon clusters, each containing up to approximately 80 atoms, distributed across atomically clean regions. Panel (a) shows presence of mobile contamination even after beam showering method. Panels (b) and (c) show the mobility of xenon clusters, as their structure appears horizontally translated in some regions, thus indicating movement during the scan.

Figure 4.10 presents large xenon clusters, containing up to approximately 145 atoms. These clusters represent the upper end of the size distribution observed in this thesis. Notable example, shown in Figure 4.10 f, includes a cluster partially embedded in a contaminated region.

In such cases, determining the exact number of atoms becomes increasingly difficult due to overlaps and limited contrast. The primary focus of this collage, however, is to highlight clusters with clear three-dimensional structures. These larger clusters deviate significantly from the typical 2D morphology and they often appear cloud-like, with diffuse and irregular edges that oppose the expected structural models derived from smaller clusters. Furthermore, their internal regions are

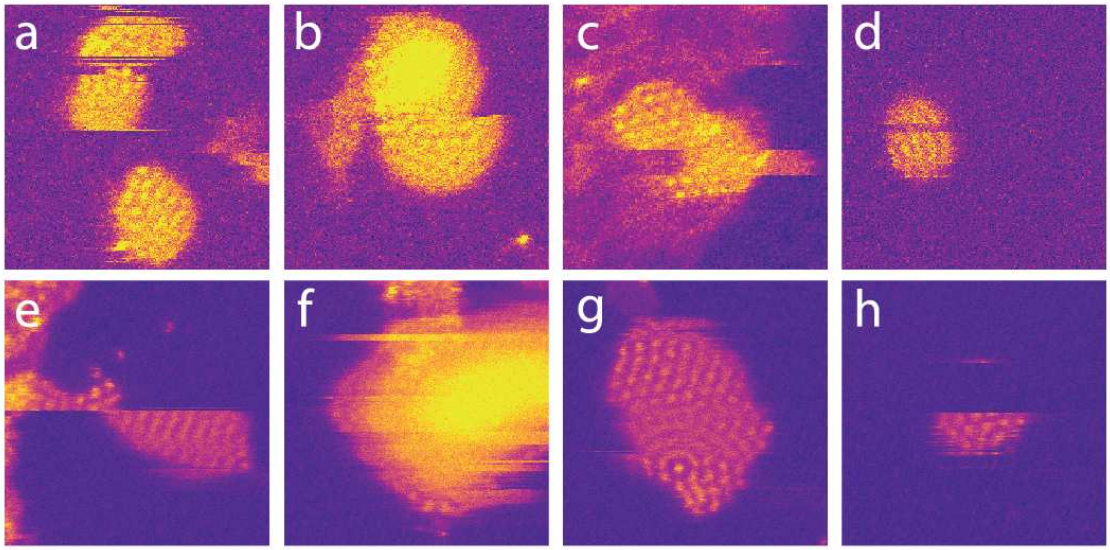

Figure 4.9: MAADS STEM micrographs that show mobility of different cluster sizes. As the image is recorded, clusters move across the clean surface or their atoms rearrange, causing blurring in the scan process or horizontal splits in the cluster structure. Size of the images in all panels is 6x6 nm^2.

highly dynamic, constantly reconfiguring in a way that renders atom-by-atom counting virtually impossible. As mentioned earlier in the context of 2D clusters, it is often feasible to infer either structure or atom count, provided one of the two is already known. In contrast, for 3D clusters such as those in Figure 4.10, neither of these parameters can be reliably extracted. Under these imaging conditions, only the 2D projected surface area of the cluster can be measured; its actual volume and total number of atoms remain unknown. The reason for this limitation stems from the nature of conventional STEM imaging. The electron beam interacts with the sample, integrating all internal features into a single 2D image. As a result, multiple stacked atoms are visually indistinguishable (they are distinguishable by the Z contrast of the image signal). A potential solution would involve tilting the sample to alter the beam's angle of incidence. This approach could potentially offer a more accurate view of the internal structure and allow 3D reconstruction of the cluster, however, such techniques fall outside the scope of this thesis.

The large quantity of data available for certain samples in this thesis is primarily a result of more extensive imaging performed on those particular regions. This was possible because the microscopy conditions, such as absence of vibrations and minimal contamination, were exceptionally favorable. In contrast, samples such as Sample C and Sample E provided fewer usable images, due to less stable imaging conditions and limited ability to acquire high-quality micrographs. Consequently, these samples contributed fewer data points to the overall analysis. In

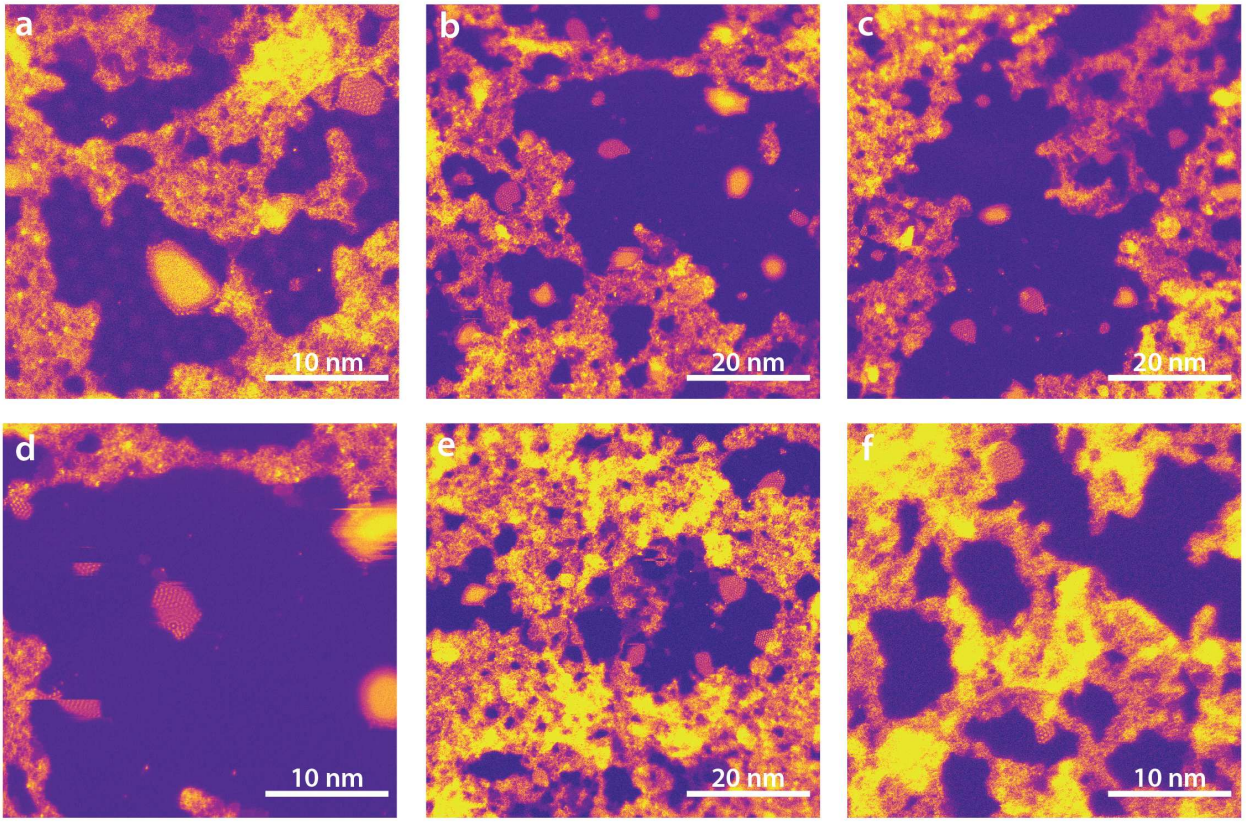

Figure 4.10: MAADF STEM micrographs of double layer graphene samples irradiated with xenon ions. The six panels correspond to different samples, with panels (a) to (e) correspoinding to Sample F, panel (f) representing Sample E. All images are color-adjusted using the "Plasma" lookup table in Fiji to enhance intensity contrast and highlight structural and morphological features such as clean double layer regions, xenon clusters, and contamination boundaries. The figure shows, among others, big xenon clusters, each containing up to approximately 140 atoms. Panels (a) to (c) showcase the cloud-like structure of three dimensional clusters. Panel (d) shows high mobility and internal dynamics of these bid three dimensional clusters. Panels (e) and (f) show that still clusters of various sizes are being implanted at all sample regions.

some cases, this discrepancy could affect the accuracy of the final analysis. It raises the possibility that certain samples, such as Sample E, may be treated as outliers and excluded from the analysis. Through control experiments, specifically on Sample A and B, where applied high bias voltages exceed the upper limits of energy distributions of the ions, it was discovered that there may be a systematic error in the experimental setup. Therefore, when interpreting results or calculating values like the implantation rate, conclusions cannot be drawn solely from samples' individual values, as they are directly dependent on the number of analyzed images per sample. To ensure a reliable representation, the final results rely on derived quantities such as total cluster implantation and implantation density of free clusters, and normalization techniques, as

presented in Figure 4.11.

To better understand the relationships between all the quantities mentioned so far, especially implantation density, it is considered important to determine what fraction of the analyzed surface area was actually clean for each sample. The calculated values are presented in Table 4.2.

Table 4.2: Analyzed area of each sample, showing the relation between the total clean area and total analyzed area of the sample, i.e., how much of the analyzed area of the sample was clean, with the value of 1 being 100% and 0 being 0%.

	Sample A	Sample B	Sample C	Sample D	Sample E	Sample F
Analyzed Area	0.39	0.68	0.24	0.16	0.24	0.24

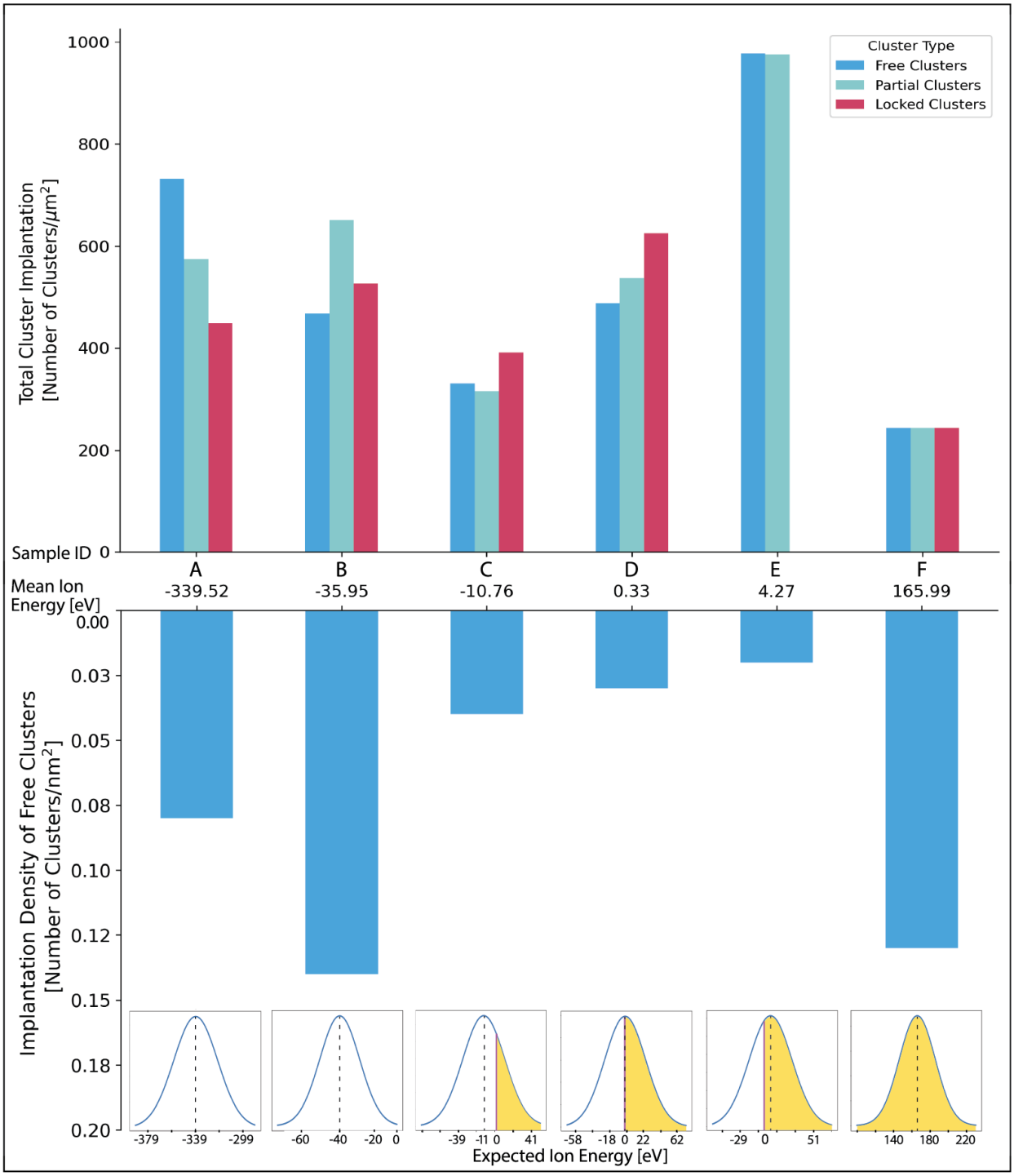

Figure 4.11: Top: Total implantation rate for each of the implanted clusters type. The horizontal axis of this figure shows the Sample IDs and is shared with the second graph, where it represents the mean ion energy. Bottom: Implantation density of free clusters. It represents the ratio between the number of implanted clusters within the atomically clean double layer graphene area and the size of that clean area. At the very bottom, beam profiles for each irradiation that was conducted on corresponding samples are shown in terms of expected ion irradiation energy after applied bias. For normalization purposes refer to the Table 4.1.

The total cluster implantation is the value that represents the ratio between the number of implanted clusters and total analyzed area, and is expressed as number of clusters per 1 μm^2 of sample area. This value was calculated for each type of implanted clusters and can be normalized by the ion flux for each of the samples. The normalization process involves identifying the maximum ion flux, dividing the ion flux of each sample by this value, and then multiplying the result by the measured number of clusters per surface area for each sample. The only exception to this normalization procedure has to be Sample A, as applying it would result in zero implanted clusters of any type. While this outcome would align perfectly with theoretical expectations, it does not reflect the actual experimental observations. The values of the total cluster implantation are shown in the upper section of the composite Figure 4.11. Derived value of implantation density of free clusters on the other hand was calculated only for the free clusters. It reflects the ratio between the number of implanted free xenon clusters into the atomically clean, uncontaminated areas of the double layer graphene, relative to the size of that clean area within the given image. Bottom half of the Figure 4.11 shows these values relative to the Sample and the mean (expected) ion energy, with yellow areas representing the interval of these energies at which corresponding sample was irradiated. Additionally, at the very bottom of the Figure 4.11 whole beam profiles after biasing are shown for each sample.

As it is shown in the Figure 4.11, both Sample A and B were subjected to high bias voltages of 500 V and 200 V respectively, i.e., values that should, in principle, fully suppress ion implantation, as they exceed the ion energy distribution from the plasma source. Yet, this was not the case. Even with the highest available bias of 500 V, implanted xenon atoms were still detected, with a density of 0.085 clusters per nm^2. Sample B, that was biased with a 200 V, still yielded an implantation density of 0.14 clusters per nm^2, which was unexpected, considering that this exceeds even the value of implantation density for Sample F, 0.13 clusters per nm^2, that was irradiated by the full energy of the plasma beam. A drop in total cluster implantation, as well as in implantation density value is seen at Sample C, especially when compared to those of Sample A and B. With a biasing value set at 0.5σ of the energy distribution of the previously measured beam profile (see Figure 4.18), irradiation of Sample C resulted in an implantation density of 0.035 clusters per nm^2. This discrepancy is even more apparent, especially considering that more extensive suppression of ions in Sample B should have yielded lower implantation. Moreover, Sample D, which was biased at the value corresponding to 0σ of the energy distribution of the previously measured beam profile (see Figure 4.19), resulted in an even lower implantation density of 0.032 clusters per nm^2, which is contrary to expectations and raises questions about the reliability of the setup.

It is important to note that, in this particular case, the sample was unintentionally exposed to full plasma power for a few seconds, which initially raised concerns about excluding it from the statistical analysis altogether. After calculating the actual dose, it was found that the brief exposure had minimal effect on the sample, and the experiment was allowed to continue. That said, these findings also bring into question the protective capability of the 500 V bias in this setup, since Sample A, despite being biased at the maximum possible biasing value of the experimental setup, still showed significant implantation, even bigger than it is at Sample C and D. In Sample E, biased at the value corresponding to -0.2σ of the energy distribution of the previously measured beam profile (see Figure 4.20), almost matching the mean of the ion energy distribution, the implantation density reached as low as 0.019 clusters per nm^2. When compared to Sample C, biased at almost the same value (see Figures 4.18 f and 4.19 f), Sample D on the contrary has highest total cluster implantation values. This lower density makes sense only when considering the total number of implanted clusters, without taking the area into consideration. In this case, Sample E having the lowest amount of analyzed data compared to any other sample, as it was previously discussed, would show lowest implantation values compared to other samples (see Figure 4.20). However, here it yields highest total cluster implantation. This trend of continuous decrease in implantation density values is interrupted with Sample F, which received the full energy distribution of ions coming from the plasma beam. It resulted in one of the highest implantation density of all samples, namely 0.13 clusters per nm^2. As anticipated, the exposure to the full range of ion energy distribution in Sample F caused damage to both single and double layer graphene, which is evident in Figures 4.12, 4.13 and 4.21. In the case of Sample B, only regions of single layer graphene showed defects, which is an unexpected outcome considering the anticipated biasing.

Figure 4.12, which highlights damage in single layer graphene and shows that xenon ions at the applied ion energy intervals, particularly in the high-energy regime, act as energetic projectiles capable of creating defects in the single layer graphene. The density of these defects was included in the dataset and statistically analyzed, as shown in Figures 4.17 and 4.21. Importantly, they were classified as defects rather than single vacancies, since it is difficult to determine how many atoms a single projectile knocked out of the lattice. Even when a defect appears to involve the absence of multiple atoms or broken bonds, it was still treated as a single defect site.

Additionally, Figure 4.13 presents data from regions where it was observed that damage also occurred in double layer regions of graphene. This indicates that the projectiles carried sufficient energy to penetrate both graphene layers, displacing carbon atoms along the way and leaving behind damage that extended through the double layer graphene. However, at no point was

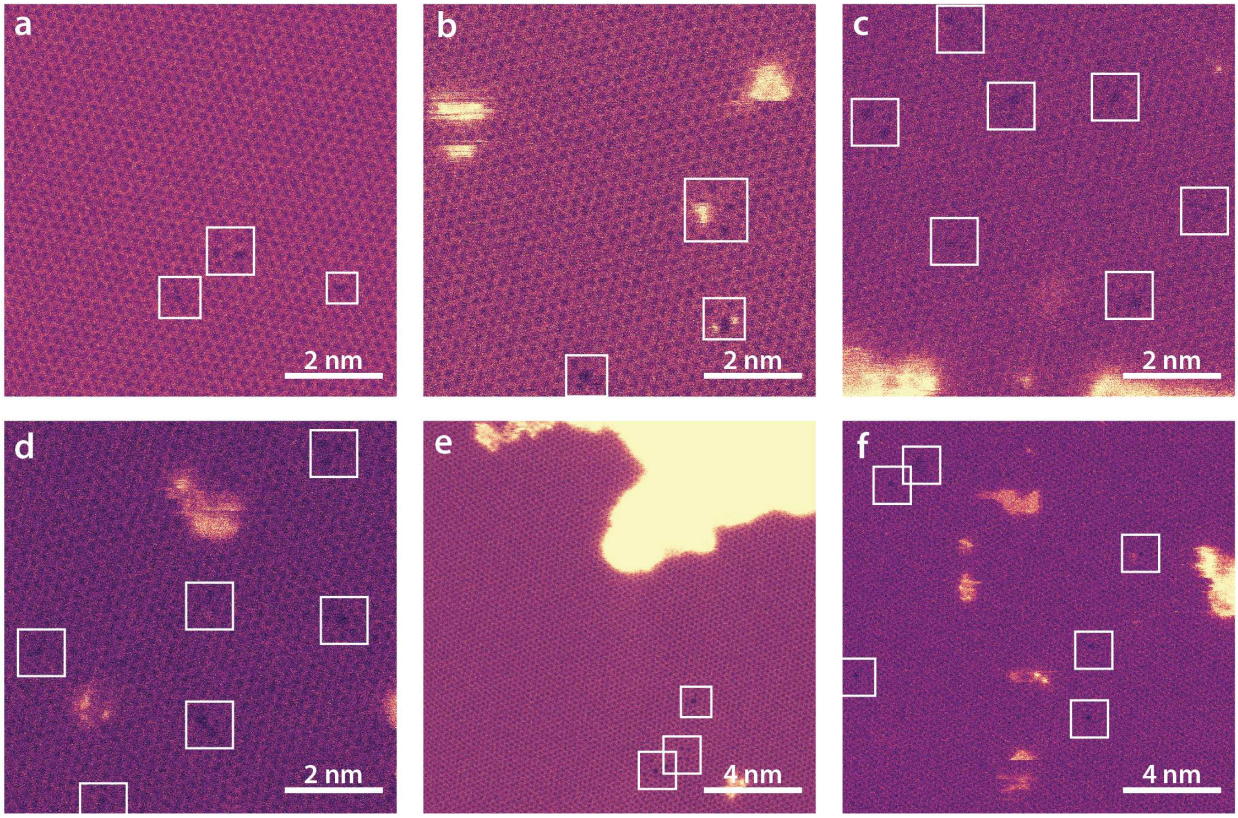

Figure 4.12: MAADF STEM micrographs of single layer graphene samples irradiated with xenon ions. The six panels correspond to individual samples, with panels (a), (e) and (f) corresponding to Sample B, and panels (b) to (d) representing Sample F. All images are color-adjusted using the "Plasma" lookup table in Fiji to enhance intensity contrast and highlight structural and morphological features. Figure shows defects in monolayer regions of these samples, highlighted in white rectangles.

xenon observed to substitute a carbon atom, that is, no instances were seen where a carbon atom was knocked out and directly replaced by a xenon atom. This case was expected, as such substitution is highly unlikely. On the other hand, the observed double layer damage itself was not initially anticipated, yet was clearly identified in the experiment.

Regarding the figures more broadly, it can be noted that the certain biasing used in the study proved to be reliable. In intervals where the ion energy was expected to result in the implantation of smaller clusters, and therefore fewer atoms, this was indeed the case. Conversely, in conditions where higher energies intervals were applied, both larger clusters and a higher number of implanted atoms were observed. These outcomes align well with the expected experimental trends.

Although the dynamics of xenon clusters was not the primary focus of this study, a substantial

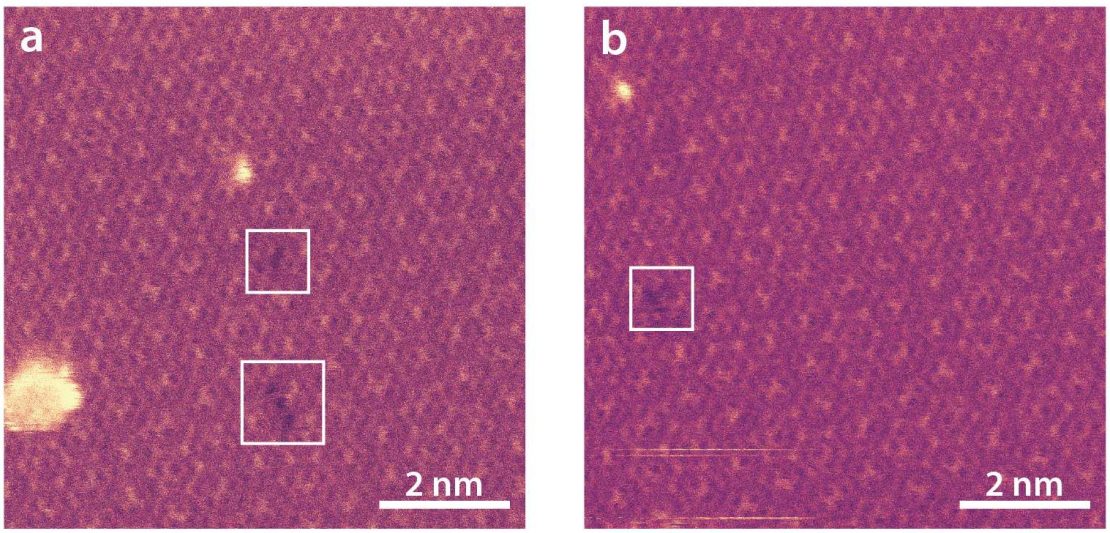

Figure 4.13: MAADF STEM micrographs of double layer graphene sample irradiated with xenon ions. The two panels correspond to Sample F. Both images are color-adjusted using the "Plasma" lookup table in Fiji to enhance intensity contrast and highlight structural and morphological features such as clean double layer regions and contamination. Figure shows defects in double layer regions of this sample, highlighted in white rectangles.

number of high-resolution images and video recordings were collected, showcasing both internal and inter-cluster dynamics. As illustrated in Figure 4.14, temporal evolution of the clusters is observed. For example, in Figure 4.14 a, a total of nine distinct clusters are visible, whereas just 60 s later, Figure 4.14 f shows only three remaining. This demonstrates the rapid dynamics of xenon clusters over very short time scales.

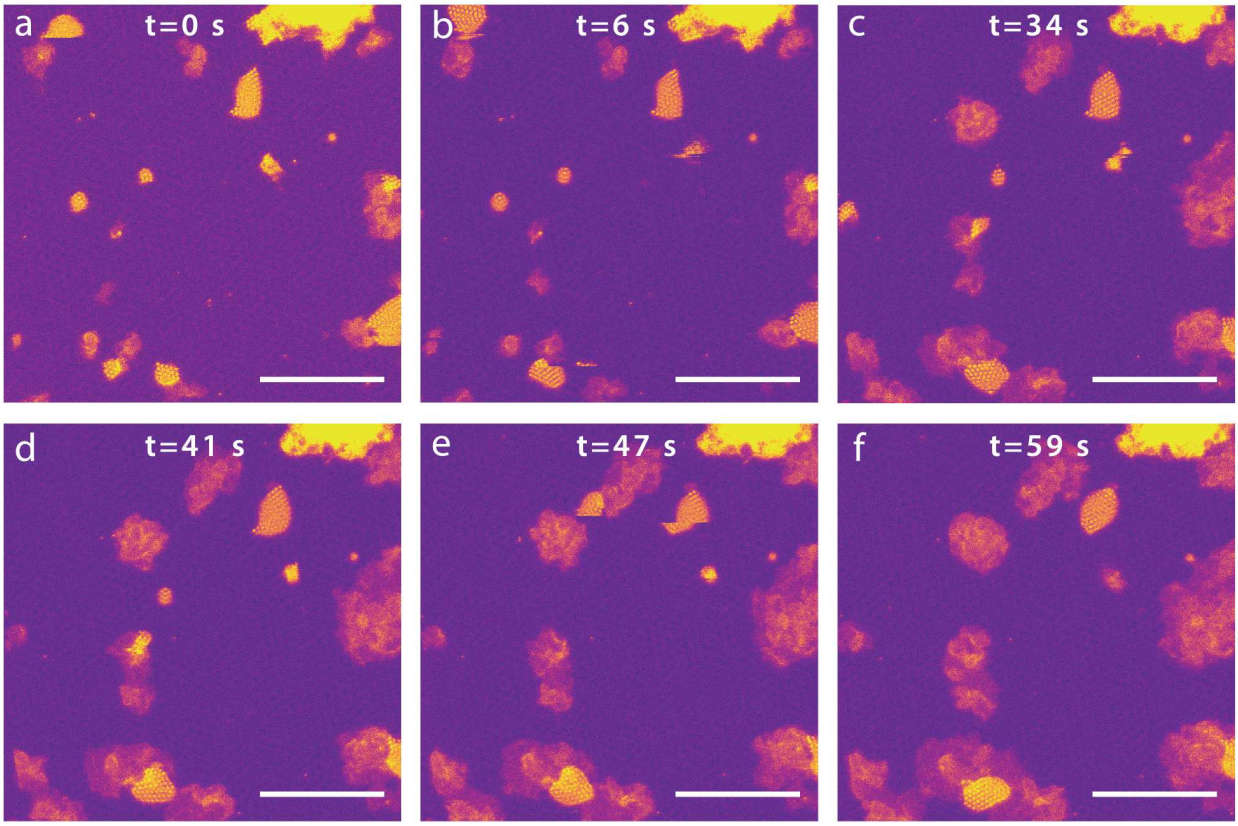

Figure 4.14: MAADF STEM micrographs of double layer graphene samples irradiated with xenon ions. All images are color-adjusted using the "Plasma" lookup table in Fiji to enhance intensity contrast and highlight structural and morphological features such as clean double layer regions, xenon clusters, and contamination boundaries. Scale bar of all pictures is 10 nm.

A more stable and visually accessible example of cluster merging is presented in Figure 4.15. This figure shows the group of smaller, less dynamic clusters, where two biggest clusters merge into one after just 38 s. However, one should not be misled by this relatively slower interaction, as xenon clusters are highly mobile, and capturing the intermediate stages of their merging process remains challenging. The difficulty arises primarily from limitations in temporal resolution. A single scan at 1024x1024 pixel resolution requires a dwell time of approximately 60 μs per pixel and 220 μs for the flyback time (time needed for the electron beam to move to the next line), results in a total acquisition time of about 3 s per frame. Given that xenon clusters are in continuous motion, the process of capturing distinct structural stages of their internal rearrangement or mutual fusion at high resolution becomes practically infeasible. Despite the interesting appeal of their dynamic behavior, it is their constant motion that makes detailed structural documentation so complex.

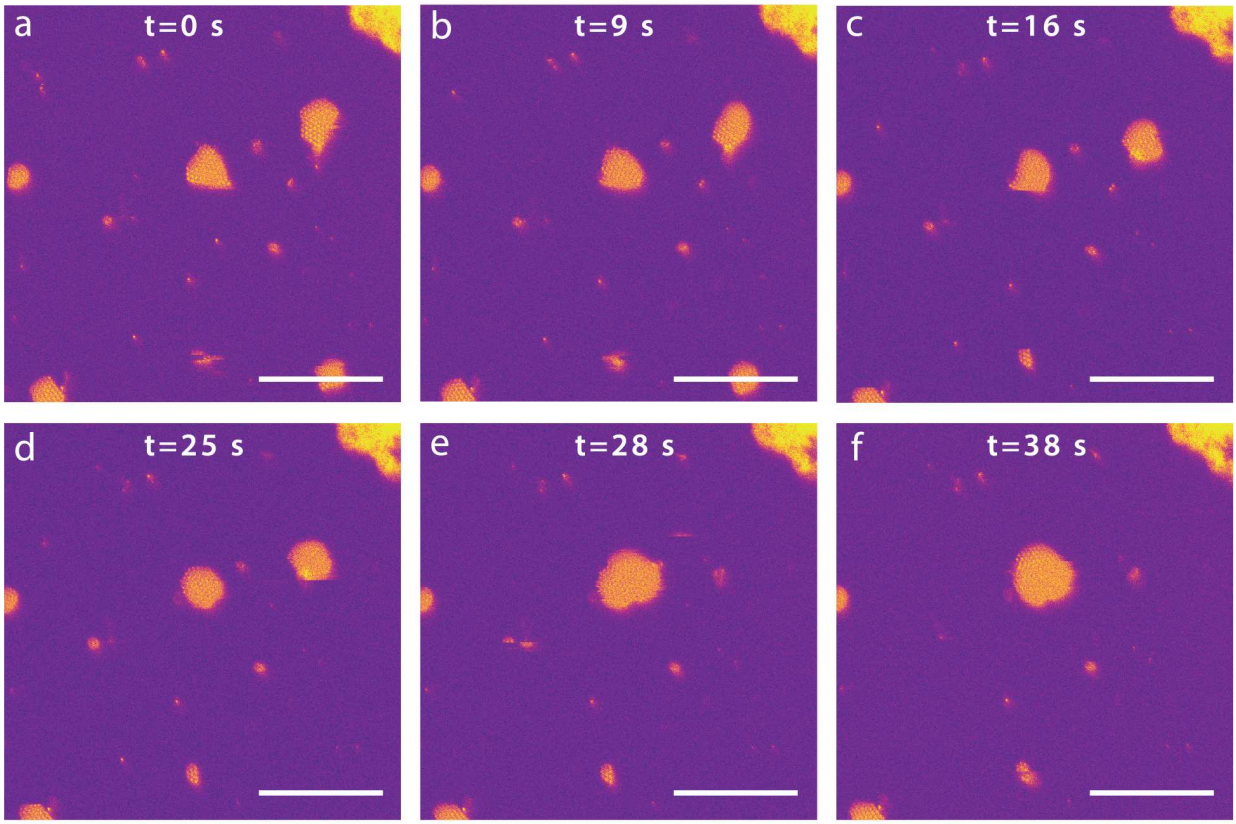

Figure 4.15: MAADF STEM micrographs of double layer graphene samples irradiated with xenon ions. All images are color-adjusted using the "Plasma" lookup table in Fiji to enhance intensity contrast and highlight structural and morphological features such as clean double layer regions, xenon clusters, and contamination boundaries. Scale bar of all pictures is 10 nm.

Following Figures 4.16, 4.17, 4.18, 4.19, 4.20 and 4.21 offer a clean overview of the raw data.

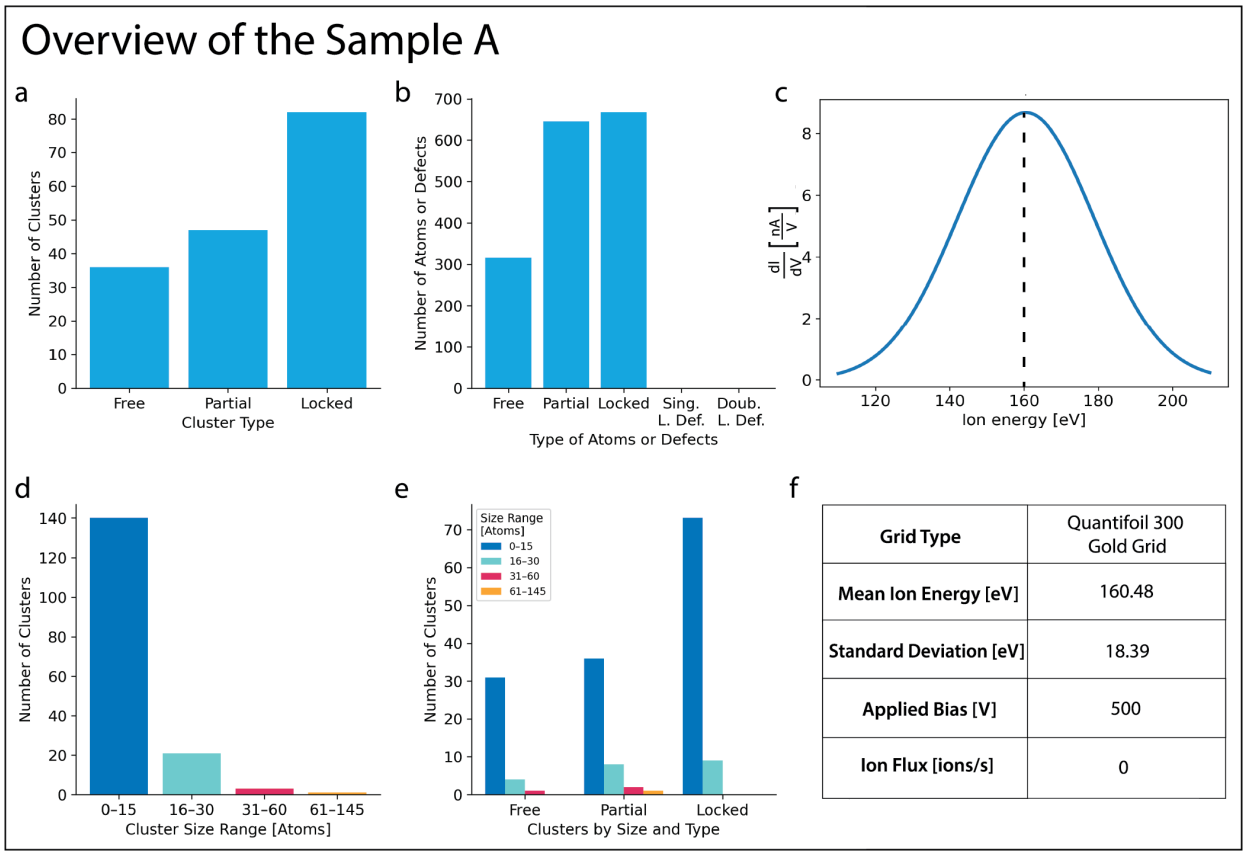

Figure 4.16: Data for Sample A. Panel (a) shows number of clusters in three different cluster type categories. Panel (b) shows number of implanted xenon atoms or created defects according to the type of implantation and defect creation. Panel (c) shows plasma beam profile before biasing, with black dotted line representing mean ion energy. Panel (d) shows number of size distribution of implanted clusters. Panel (e) shows size distribution of implanted clusters according to the cluster implantation type. Panel (f) shows a table overview of sample's grid type, mean ion energy, standard deviation of energy distribution shown in panel (f), applied biasing value, and calculated ion flux.

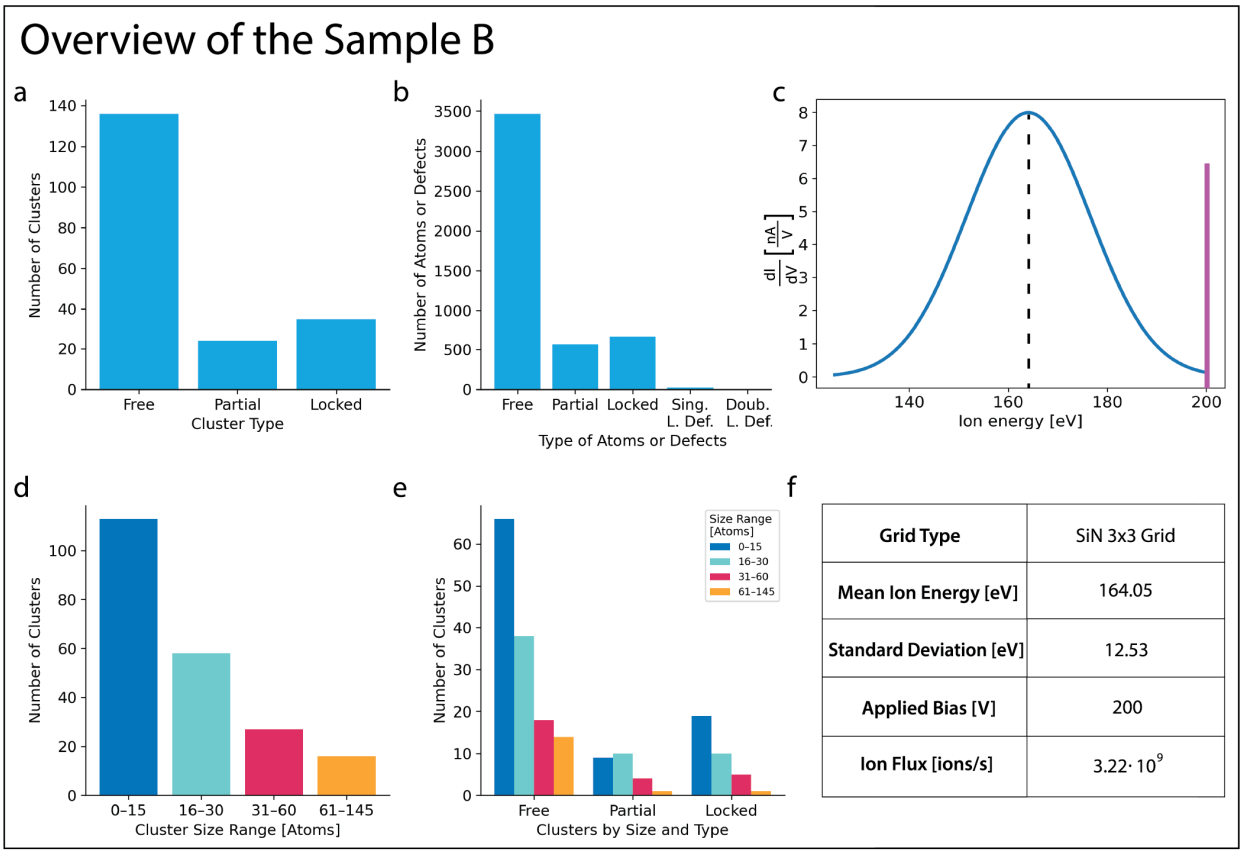

Figure 4.17: Data for Sample B. Panel (a) shows number of clusters in three different cluster type categories. Panel (b) shows number of implanted xenon atoms or created defects according to the type of implantation and defect creation. Panel (c) shows plasma beam profile before biasing, with black dotted line representing mean ion energy and purple line showing the value of the bias. Panel (d) shows number of size distribution of implanted clusters. Panel (e) shows size distribution of implanted clusters according to the cluster implantation type. Panel (f) shows a table overview of sample's grid type, mean ion energy, standard deviation of energy distribution shown in panel (f), applied biasing value, and calculated ion flux.

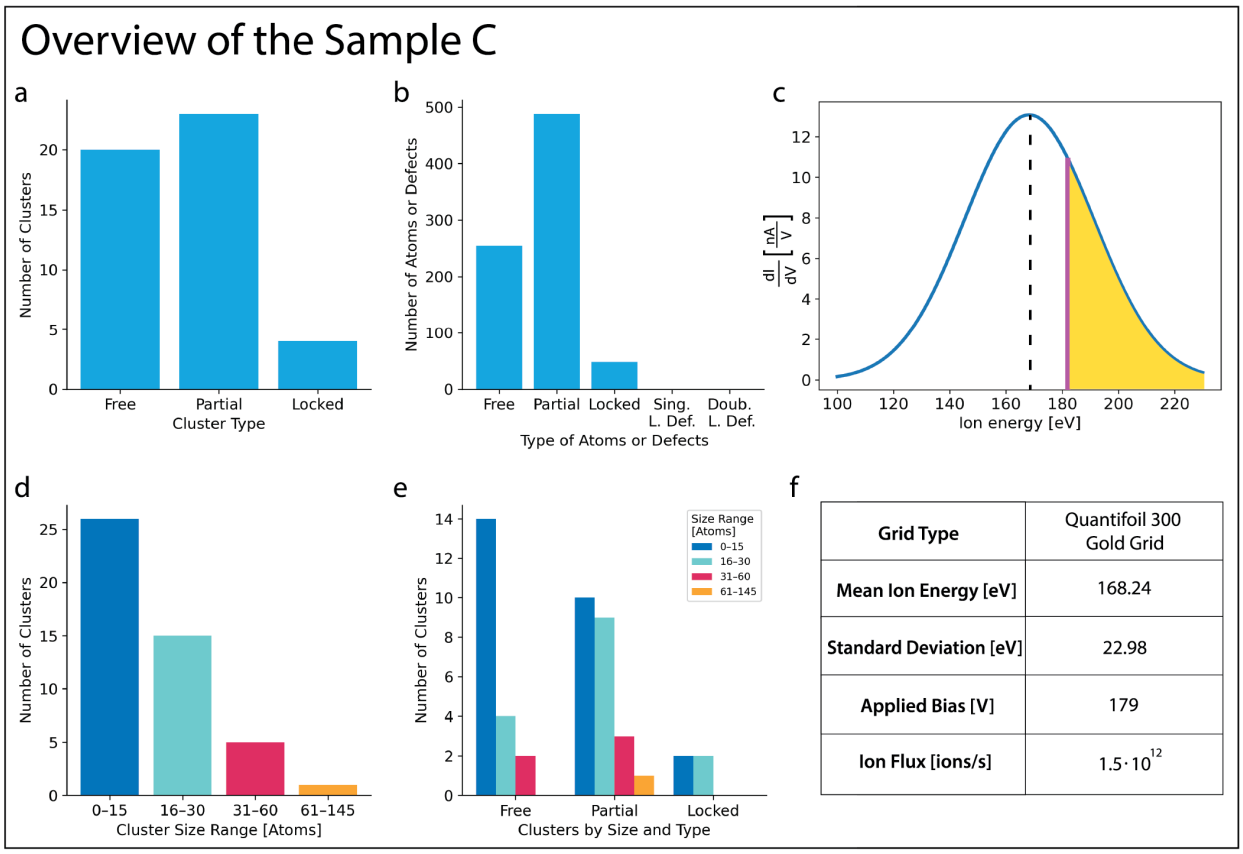

Figure 4.18: Data for Sample C. Panel (a) shows number of clusters in three different cluster type categories. Panel (b) shows number of implanted xenon atoms or created defects according to the type of implantation and defect creation. Panel (c) shows plasma beam profile before biasing, with black dotted line representing mean ion energy, purple line showing the value of the bias and yellow area under the curve representing the portion of the energy distribution of ions interacting with the sample. Panel (d) shows number of size distribution of implanted clusters. Panel (e) shows size distribution of implanted clusters according to the cluster implantation type. Panel (f) shows a table overview of sample's grid type, mean ion energy, standard deviation of energy distribution shown in panel (f), applied biasing value, and calculated ion flux.

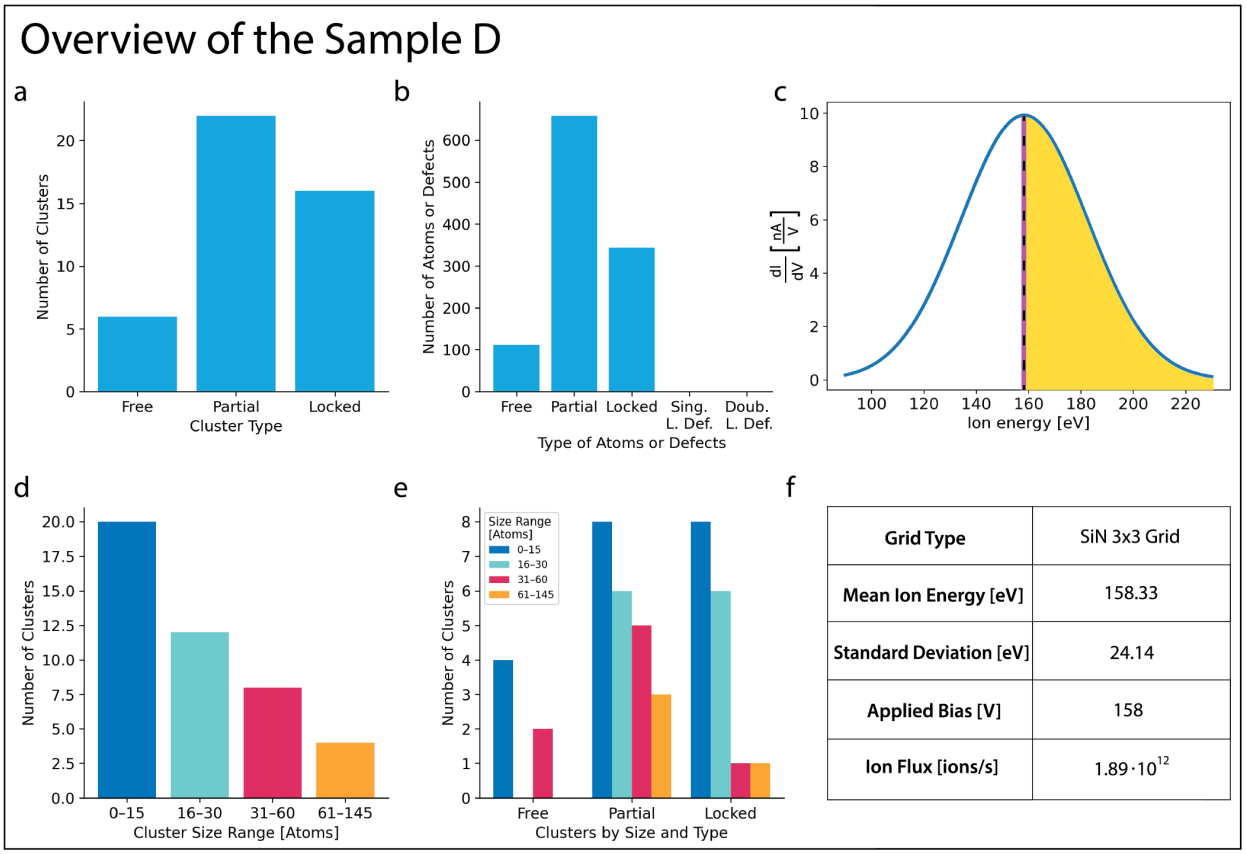

Figure 4.19: Data for Sample D. Panel (a) shows number of clusters in three different cluster type categories. Panel (b) shows number of implanted xenon atoms or created defects according to the type of implantation and defect creation. Panel (c) shows plasma beam profile before biasing, with black dotted line representing mean ion energy, purple line showing the value of the bias and yellow area under the curve representing the portion of the energy distribution of ions interacting with the sample. Panel (d) shows number of size distribution of implanted clusters. Panel (e) shows size distribution of implanted clusters according to the cluster implantation type. Panel (f) shows a table overview of sample's grid type, mean ion energy, standard deviation of energy distribution shown in panel (f), applied biasing value, and calculated ion flux.

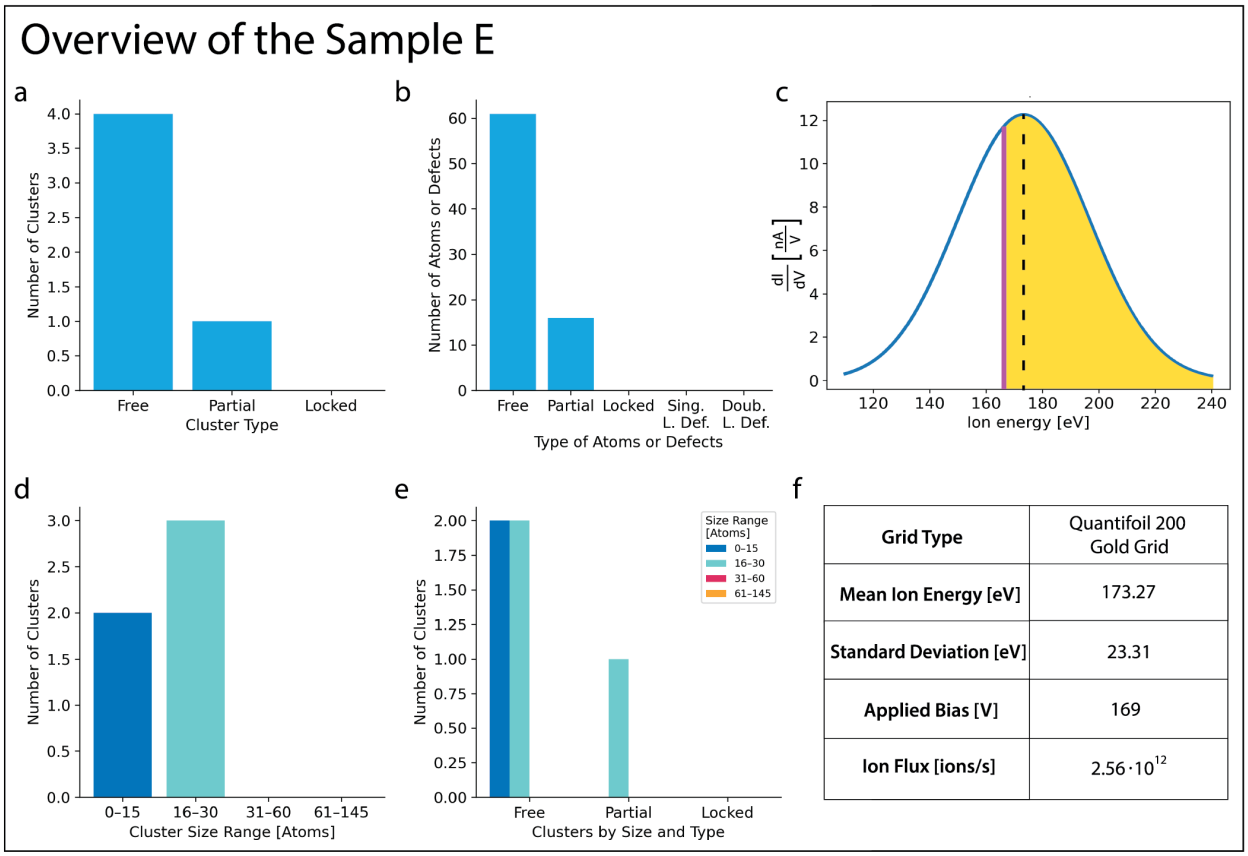

Figure 4.20: Data for Sample E. Panel (a) shows number of clusters in three different cluster type categories. Panel (b) shows number of implanted xenon atoms or created defects according to the type of implantation and defect creation. Panel (c) shows plasma beam profile before biasing, with black dotted line representing mean ion energy, purple line showing the value of the bias and yellow area under the curve representing the portion of the energy distribution of ions interacting with the sample. Panel (d) shows number of size distribution of implanted clusters. Panel (e) shows size distribution of implanted clusters according to the cluster implantation type. Panel (f) shows a table overview of sample's grid type, mean ion energy, standard deviation of energy distribution shown in panel (f), applied biasing value, and calculated ion flux.

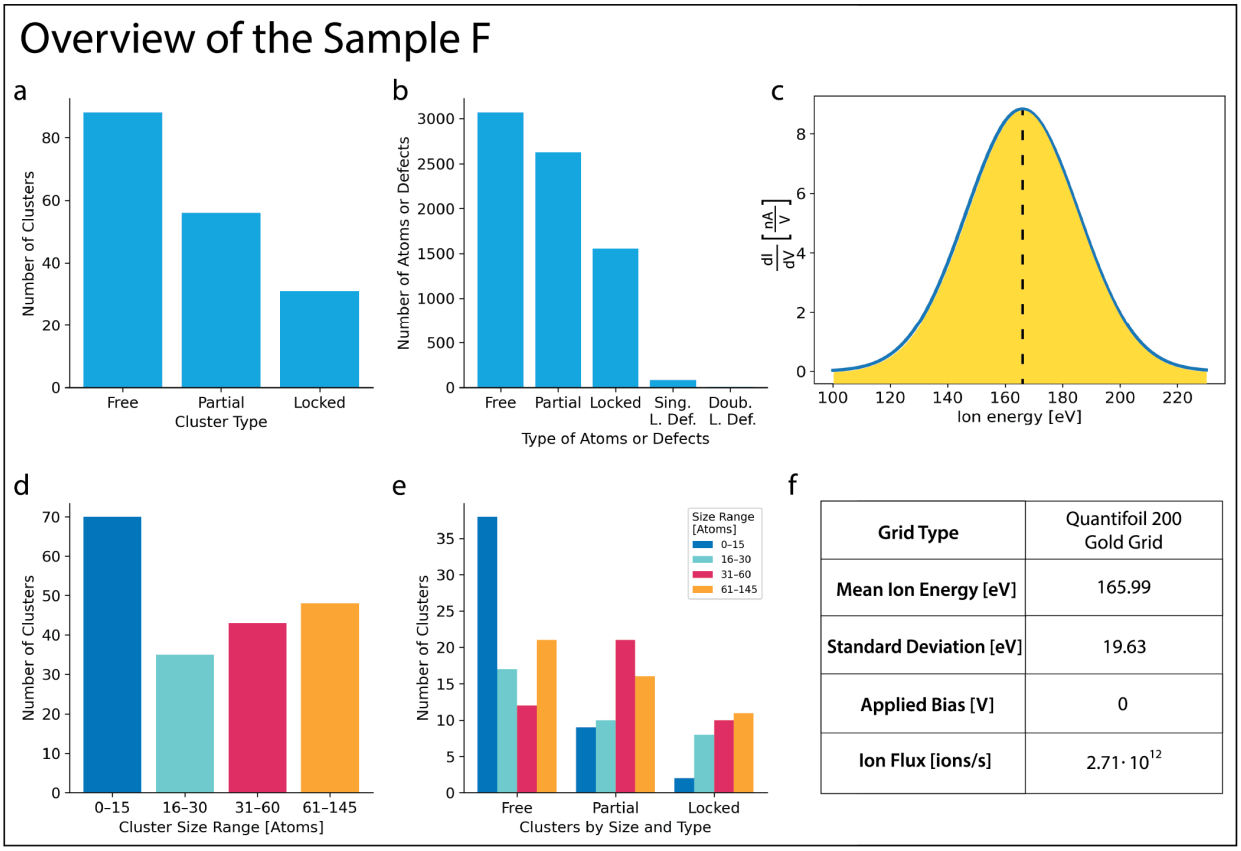

Figure 4.21: Data for Sample F. Panel (a) shows number of clusters in three different cluster type categories. Panel (b) shows number of implanted xenon atoms or created defects according to the type of implantation and defect creation. Panel (c) shows plasma beam profile before biasing, with black dotted line representing mean ion energy, and yellow area under the curve representing the portion of the energy distribution of ions interacting with the sample. Panel (d) shows number of size distribution of implanted clusters. Panel (e) shows size distribution of implanted clusters according to the cluster implantation type. Panel (f) shows a table overview of sample's grid type, mean ion energy, standard deviation of energy distribution shown in panel (f), applied biasing value, and calculated ion flux.

During the data analysis process, certain tendencies were observed in the behavior of xenon atoms during cluster formation, specifically, their preference for particular spatial confinements under the experimental conditions. These observations open up two potential approaches for further analysis. First, in cases where the number of atoms in a cluster is unknown, the number can be estimated based on the cluster's shape and dimensions. Second, when the atom count is already known, this data can be used to infer the appearance of clusters that may be obscured, for example by contamination. The main objective of this thesis was to explore and validate whether this novel approach of implantation is both feasible and reliable. Having confirmed that

the implantation of xenon atoms into double layer graphene can be successfully achieved, we can conclude that this process has, for the first time, been realized within our university laboratory. However, the second major goal of this work, namely determining the threshold energy required to displace a carbon atom from the lattice, could not be fulfilled. This is because none of the measurements carried out resulted in a complete lack of xenon implantation or a damage-free single layer regions. Consequently, we turned to statistical analysis as a way to better understand the experimental outcomes, leading to the figures presented in this work. These findings offer a basis for further statistical or computational studies that could ultimately determine this threshold energy. Since theoretical estimates do exist, verifying them experimentally would be of great value.

Nevertheless, as evident from the Figure 4.11, no clear dependency could be established between the applied bias voltage, the energy distribution of ions, and the resulting implantation density. From this, we conclude that, despite its ability to facilitate successful xenon implantation, the current irradiation setup cannot be considered reliable for precise experimental control. Likely possibility is that the positive bias attracts electrons to the puck and they shield the bias from ions which results in less deceleration as expected. This discrepancy means the experiments were not conducted under the intended conditions. Initially, we were excited to observe successful xenon implantation in the double layer graphene samples. However, in the cases of Samples A and B, where no implantation was expected due to the high bias, we anticipated being able to interpolate the exact biasing threshold that either enables or entirely prevents implantation. Unfortunately, this was not achieved. On a positive note, these findings set the stage for future work, beginning with a complete redesign of the irradiation stage and deceleration setup. Ensuring reliable electrical contact for proper puck biasing as a priority. Following this hardware improvement, further characterization of the plasma source will enable future researchers to work with a setup that provides reliable data and an accurate understanding of the underlying physics.

Looking ahead, the data gathered in this thesis also offers several exciting directions for future research. This includes investigating the internal dynamics of clusters, their mobility across double layer graphene, their interaction with different moiré patterns, and how they merge or form from individual atoms. There is also potential in studying clusters partially anchored to contamination, identifying holes within clusters that reveal double layer structure, and even mapping double layer graphene using the trajectories of large clusters.

Chapter 5

Conclusions

One of the most important aspects of this study, and one that must not be overlooked, is the sheer scale of the analysis: several hundred images were examined, and a total of 15 786 individual xenon atoms were counted manually. Considering that this was done without any form of automated software assistance, particular attention was given to the potential for counting errors, which were evaluated in accordance with the categorization of cluster sizes. Smaller clusters inherently carry a lower risk of counting error. Not only are they easier to resolve visually, but they are also less prone to internal structural changes or reorganization during observation. Moreover, they tend to maintain their two-dimensional morphology over time, which further contributes to the reliability of the manual counting process.

Experimental results presented in this work aimed to explore the controlled implantation of xenon atoms into double layer graphene using low-energy ion irradiation, with particular attention to the dependence of implantation outcomes on the applied bias voltage and the ion energy distribution of the plasma source. One of the goals was to identify an energy threshold below which ion implantation would not occur, thereby determining the displacement threshold energy of carbon atoms in double layer graphene. Contrary to what was expected, the experimental data revealed significant discrepancies between the intended experimental conditions and the actual outcomes. Even under high applied bias voltages designed to fully block the incoming ions, xenon atoms were still implanted in the double layer graphene. Specifically, Sample A, irradiated under the highest applied bias, still exhibited an implantation density of 0.085 clusters per nm^2, suggesting that either the biasing system was ineffective or the ions still somehow retained enough energy to overcome the intended energy barrier. This trend continued in Sample B, where a 200 V bias corresponding to approximately three standard deviations from the mean

beam energy distribution still resulted in a measured implantation density of 0.14 clusters per nm^2. This was higher than Sample C, where biasing value, corresponding to the 0.5σ of the previously measured unbiased ion energy distribution, was used, and an even lower implantation density of 0.035 clusters per nm^2 was observed. These findings are in direct contradiction with the theoretical assumption that increasing the bias should reduce implantation due to electrostatic deceleration of incoming ions. Further experiments on Sample D, under a bias setting of 0σ, returned an unexpectedly low implantation density of 0.032 clusters per nm^2, which is even less than all previous samples despite the less restrictive bias. While this value could be attributed in part to limited imaging data, it still deviates significantly from the expected trend of results. Similarly, Sample E, biased at the value corresponding to -0.2σ of the previously measured beam profile, showed an implantation density of 0.019 clusters per nm^2, which was inconsistent with the increased exposure. Finally, Sample F, which received full plasma source energy exposure without any deceleration (0 V bias), yielded the second highest implantation density of 0.13 clusters per nm^2, in line with assumptions and expectations that low bias input leads to increased implantation. Despite this partial alignment with theoretical trends, namely that lower bias and higher ion energy interval leads to more implantation, the lack of a consistent and monotonic correlation across all samples ultimately prevents a definitive conclusion about the threshold displacement energy. This discrepancy strongly suggests that the current irradiation system is not functioning as expected, allowing unintended ion implantation even under supposed energy-filtering conditions. Additionally, the damage observed in single layer graphene in Sample B, and in both single and double layer graphene in Sample F, was showed through present defects, indicating that the beam energy was sufficient not only to implant atoms but also to displace carbon atoms from one and both layers. However, no evidence was found for xenon atoms replacing carbon within the lattice, aligning with theoretical predictions that such events are highly unlikely under these conditions.

Altogether, these results confirm that xenon implantation into double layer graphene is possible across a wide range of nominally decelerated ion energies, but also highlight that the experimental setup, particularly the biasing system, must be re-evaluated. Without a functioning and verifiable deceleration mechanism, the goal of determining a reliable threshold displacement energy cannot be fulfilled.

Bibliography

[1] K. S. Novoselov, A. K. Geim, S. V. Morozov, D. Jiang, Y. Zhang, S. V. Dubonos, I. V. Grigorieva, A. A. Firsov, Electric Field Effect in Atomically Thin Carbon Films, Science 306 (5696) (2004) 666–669. doi:10.1126/science.1102896.

[2] C. Lee, X. Wei, J. W. Kysar, J. Hone, Measurement of the Elastic Properties and Intrinsic Strength of Monolayer Graphene, Science 321 (5887) (2008) 385–388. doi:10.1126/science.1157996.

[3] A. Zandiatashbar, G.-H. Lee, S. J. An, S. Lee, N. Mathew, M. Terrones, T. Hayashi, C. R. Picu, J. Hone, N. Koratkar, Effect of defects on the intrinsic strength and stiffness of graphene, Nat Commun 5 (1) (2014) 3186. doi:10.1038/ncomms4186.

[4] J. Wang, X. Jin, C. Li, W. Wang, H. Wu, S. Guo, Graphene and graphene derivatives toughening polymers: Toward high toughness and strength, Chemical Engineering Journal 370 (2019) 831–854. doi:10.1016/j.cej.2019.03.229.

[5] G. Compagnini, F. Giannazzo, S. Sonde, V. Raineri, E. Rimini, Ion irradiation and defect formation in single layer graphene, Carbon 47 (14) (2009) 3201–3207. doi:10.1016/j.carbon.2009.07.033.

[6] X. Wu, H. Zhao, D. Yan, J. Pei, Doping of graphene using ion beam irradiation and the atomic mechanism, Computational Materials Science 129 (2017) 184–193. doi:10.1016/j.commatsci.2016.12.025.

[7] X. Wu, R. Yang, X. Chen, W. Liu, Fabrication of Nanopore in MoS2-Graphene vdW Heterostructure by Ion Beam Irradiation and the Mechanical Performance, Nanomaterials 12 (2) (2022) 196. doi:10.3390/nano12020196.

[8] Z. Li, F. Chen, Ion beam modification of two-dimensional materials: Characterization, properties, and applications, Applied Physics Reviews 4 (1) (2017) 011103. doi:10.1063/1.4977087.

[9] M. Längle, K. Mizohata, C. Mangler, A. Trentino, K. Mustonen, E. H. Åhlgren, J. Kotakoski, Two-dimensional few-atom noble gas clusters in a graphene sandwich, Nat. Mater. 23 (6) (2024) 762–767. doi:10.1038/s41563-023-01780-1.

[10] A. Zinoviev, P.Yu. Babenko, K. Nordlund, Nuclear stopping powers for DFT potentials, Nuclear Instruments and Methods in Physics Research Section B: Beam Interactions with Materials and Atoms 508 (2021) 10–18. doi:10.1016/j.nimb.2021.10.001.

[11] J. C. Meyer, F. Eder, S. Kurasch, V. Skakalova, J. Kotakoski, H. J. Park, S. Roth, A. Chuvilin, S. Eyhusen, G. Benner, A. V. Krasheninnikov, U. Kaiser, Accurate Measurement of Electron Beam Induced Displacement Cross Sections for Single-Layer Graphene, Phys. Rev. Lett. 108 (19) (2012) 196102. doi:10.1103/PhysRevLett.108.196102.

[12] J. C. Meyer, F. Eder, S. Kurasch, V. Skakalova, J. Kotakoski, H. J. Park, S. Roth, A. Chuvilin, S. Eyhusen, G. Benner, A. V. Krasheninnikov, U. Kaiser, Erratum: Accurate Measurement of Electron Beam Induced Displacement Cross Sections for Single-Layer Graphene [Phys. Rev. Lett. 108, 196102 (2012)], Phys. Rev. Lett. 110 (23) (2013) 239902. doi:10.1103/PhysRevLett.110.239902.

[13] M. Norgett, M. Robinson, I. Torrens, A proposed method of calculating displacement dose rates, Nuclear Engineering and Design 33 (1) (1975) 50–54. doi:10.1016/0029-5493(75)90035-7.

[14] R. Gross, A. Marx, Festkörperphysik:, OLDENBOURG WISSENSCHAFTSVERLAG, 2014. doi:10.1524/9783110358704.

[15] P. R. Wallace, The Band Theory of Graphite, Physical Review 71 (9) (1947) 622–634. doi:10.1103/PhysRev.71.622.

[16] A. H. Castro Neto, F. Guinea, N. M. R. Peres, K. S. Novoselov, A. K. Geim, The electronic properties of graphene, Reviews of Modern Physics 81 (1) (2009) 109–162. doi:10.1103/RevModPhys.81.109.

[17] R. E. Prange, S. M. Girvin, The Quantum Hall Effect, Springer Science & Business Media, 2012.

[18] R. Du, M.-H. Liu, J. Mohrmann, F. Wu, R. Krupke, H. Von Löhneysen, K. Richter, R. Danneau, Tuning Anti-Klein to Klein Tunneling in Bilayer Graphene, Physical Review Letters 121 (12) (2018) 127706. doi:10.1103/PhysRevLett.121.127706.

[19] R. A. Jishi, D. Inomata, K. Nakao, M. S. Dresselhaus, G. Dresselhaus, Electronic and Lattice Properties of Carbon Nanotubes, Journal of the Physical Society of Japan 63 (6) (1994) 2252–2260. doi:0.1143/JPSJ.63.2252.

[20] K. S. Novoselov, A. K. Geim, S. V. Morozov, D. Jiang, M. I. Katsnelson, I. V. Grigorieva, S. V. Dubonos, A. A. Firsov, Two-dimensional gas of massless Dirac fermions in graphene, Nature 438 (7065) (2005) 197–200. doi:10.1038/nature04233.

[21] C. Lee, X. Wei, J. W. Kysar, J. Hone, Measurement of the Elastic Properties and Intrinsic Strength of Monolayer Graphene, Science 321 (5887) (2008) 385–388. doi:10.1126/science.1157996.

[22] J.-U. Lee, D. Yoon, H. Cheong, Estimation of Young's Modulus of Graphene by Raman Spectroscopy, Nano Lett. 12 (9) (2012) 4444–4448. doi:10.1021/nl301073q.

[23] J. S. Bunch, S. S. Verbridge, J. S. Alden, A. M. Van Der Zande, J. M. Parpia, H. G. Craighead, P. L. McEuen, Impermeable Atomic Membranes from Graphene Sheets, Nano Lett. 8 (8) (2008) 2458–2462. doi:10.1021/nl801457b.

[24] P. Z. Sun, Q. Yang, W. J. Kuang, Y. V. Stebunov, W. Q. Xiong, J. Yu, R. R. Nair, M. I. Katsnelson, S. J. Yuan, I. V. Grigorieva, M. Lozada-Hidalgo, F. C. Wang, A. K. Geim, Limits on gas impermeability of graphene, Nature 579 (7798) (2020) 229–232. doi:10.1038/s41586-020-2070-x.

[25] E. Stolyarova, D. Stolyarov, K. Bolotin, S. Ryu, L. Liu, K. T. Rim, M. Klima, M. Hybertsen, I. Pogorelsky, I. Pavlishin, K. Kusche, J. Hone, P. Kim, H. L. Stormer, V. Yakimenko, G. Flynn, Observation of Graphene Bubbles and Effective Mass Transport under Graphene Films, Nano Lett. 9 (1) (2009) 332–337. doi:10.1021/nl803087x.

[26] J. C. Meyer, A. K. Geim, M. I. Katsnelson, K. S. Novoselov, T. J. Booth, S. Roth, The structure of suspended graphene sheets, Nature 446 (7131) (2007) 60–63. doi:10.1038/nature05545.

[27] T. Susi, C. Hofer, G. Argentero, G. T. Leuthner, T. J. Pennycook, C. Mangler, J. C. Meyer, J. Kotakoski, Isotope analysis in the transmission electron microscope, Nat Commun 7 (1) (2016) 13040. doi:10.1038/ncomms13040.

[28] R. Mirzayev, K. Mustonen, M. R. A. Monazam, A. Mittelberger, T. J. Pennycook, C. Mangler, T. Susi, J. Kotakoski, J. C. Meyer, Buckyball sandwiches, Sci. Adv. 3 (6) (2017) e1700176. doi:10.1126/sciadv.1700176.

[29] X. Ye, M. R. Jones, L. B. Frechette, Q. Chen, A. S. Powers, P. Ercius, G. Dunn, G. M. Rotskoff, S. C. Nguyen, V. P. Adiga, A. Zettl, E. Rabani, P. L. Geissler, A. P. Alivisatos, Single-particle mapping of nonequilibrium nanocrystal transformations, Science 354 (6314) (2016) 874–877. doi:10.1126/science.aah4434.

[30] J. M. Yuk, J. Park, P. Ercius, K. Kim, D. J. Hellebusch, M. F. Crommie, J. Y. Lee, A. Zettl, A. P. Alivisatos, High-Resolution EM of Colloidal Nanocrystal Growth Using Graphene Liquid Cells, Science 336 (6077) (2012) 61–64. doi:10.1126/science.1217654.

[31] R. S. Pantelic, J. C. Meyer, U. Kaiser, H. Stahlberg, The application of graphene as a sample support in transmission electron microscopy, Solid State Communications 152 (15) (2012) 1375–1382. doi:10.1016/j.ssc.2012.04.038.

[32] K. S. Vasu, E. Prestat, J. Abraham, J. Dix, R. J. Kashtiban, J. Beheshtian, J. Sloan, P. Carbone, M. Neek-Amal, S. J. Haigh, A. K. Geim, R. R. Nair, Van der Waals pressure and its effect on trapped interlayer molecules, Nat Commun 7 (1) (2016) 12168. doi:10.1038/ncomms12168.

[33] C. Lee, W. Xiaoding, W. K. Jeffrey, J. Hone, Measurement of the Elastic Properties and Intrinsic Strength of Monolayer Graphene, Science (American Association for the Advancement of Science) 321 (5887) (2008) 385–388. doi:10.1126/science.1157996.

[34] O. Frank, G. Tsoukleri, I. Riaz, K. Papagelis, J. Parthenios, A. C. Ferrari, A. K. Geim, K. S. Novoselov, C. Galiotis, Development of a universal stress sensor for graphene and carbon fibres, Nat Commun 2 (255) (2011). doi:10.1038/ncomms1247.

[35] D. A. Dikin, S. Stankovich, E. J. Zimney, R. D. Piner, G. H. B. Dommett, G. Evmenenko, S. T. Nguyen, R. S. Ruoff, Preparation and characterization of graphene oxide paper, Nature 448 (7152) (2007) 457–460. doi:10.1038/nature06016.

[36] Y. Zhang, Y.-W. Tan, H. L. Stormer, P. Kim, Experimental observation of the quantum Hall effect and Berry's phase in graphene, Nature 438 (7065) (2005) 201–204. doi:10.1038/nature04235.

[37] C. Mangler, J. Meyer, A. Mittelberger, K. Mustonen, T. Susi, J. Kotakoski, A Materials Scientist's CANVAS: A System for Controlled Alteration of Nanomaterials in Vacuum Down to the Atomic Scale, Microscopy and Microanalysis 28 (S1) (2022) 2940–2942. doi:10.1017/S1431927622011023.

[38] M. Hotz, G. Corbin, N. Dellby, O. Krivanek, C. Mangier, J. Meyer, Ultra-High Vacuum Aberration-Corrected STEM for in-situ studies, Microsc Microanal 22 (S3) (2016) 34–35. doi:10.1017/S1431927616001021.

[39] W. Joudi, R. S. Windisch, A. Trentino, D. Propst, J. Madsen, T. Susi, C. Mangler, K. Mustonen, F. Libisch, J. Kotakoski, Corrugation-Dominated Mechanical Softening of Defect-Engineered Graphene, Phys. Rev. Lett. 134 (16) (2025) 166102. doi:10.1103/PhysRevLett.134.166102.

[40] SPECS User Manual MPS-ECR Plasma Cracker Source (2013).

[41] K. L. Brown, G. W. Tautfest, Faraday-Cup Monitors for High-Energy Electron Beams, Review of Scientific Instruments 27 (9) (1956) 696–702. doi:10.1063/1.1715674.

[42] J. Lindhard, M. Scharff, H. Schitt, Range Concepts and Heavy Ion Ranges (Notes on Atomic Collisions, II), Vol. 6, Matematisk-fysiske Meddelelser udgivet af det Kong. danske Videnskabernes Selskab, Munksgaard, 1963. doi:10.1080/00337577008235052.

[43] M. Schleberger, J. Kotakoski, 2D Material Science: Defect Engineering by Particle Irradiation, Materials 11 (10) (2018) 1885. doi:10.3390/ma11101885.

[44] P. Sigmund, Stopping of slow ions, Bull. Russ. Acad. Sci. Phys. 72 (5) (2008) 569–578. doi:10.3103/S1062873808050018.

[45] J. M. Blatt, L. C. Biedenharn, The Angular Distribution of Scattering and Reaction Cross Sections, Rev. Mod. Phys. 24 (4) (1952) 258–272. doi:10.1103/RevModPhys.24.258.

[46] M. Nastasi, J. Mayer, J. K. Hirvonen, Ion-Solid Interactions: Fundamentals and Applications, 1st Edition, Cambridge University Press, 1996. doi:10.1017/CBO9780511565007.

[47] M. Backman, Effects of nuclear and electronic stopping power on ion irradiation of silicon-based compounds, Ph.D. thesis, University of Helsinki, Finland (2012).

[48] J. F. Ziegler, M. Ziegler, J. Biersack, SRIM – The stopping and range of ions in matter (2010), Nuclear Instruments and Methods in Physics Research Section B: Beam Interactions with Materials and Atoms 268 (11-12) (2010) 1818–1823. doi:10.1016/j.nimb.2010.02.091.

[49] E. H. Lieb, B. Simon, The Thomas-Fermi theory of atoms, molecules and solids, Advances in Mathematics 23 (1) (1977) 22–116. doi:10.1016/0001-8708(77)90108-6.

[50] A. K. Belyaev, A. I. Toropkin, A. S. Tyukanov, Nonadiabatic transitions in collisions of a negative hydrogen ion with a hydrogen molecule, Russ. J. Phys. Chem. B 6 (2) (2012) 229–233. doi:10.1134/S1990793112020157.

[51] H. Bethe, Zur Theorie des Durchgangs schneller Korpuskularstrahlen durch Materie, Annalen der Physik 397 (3) (1930) 325–400. doi:10.1002/andp.19303970303.

[52] D. J. Stephens, V. J. Allan, Light Microscopy Techniques for Live Cell Imaging, Science 300 (5616) (2003) 82–86. doi:10.1126/science.1082160.

[53] C. J. Peddie, C. Genoud, A. Kreshuk, K. Meechan, K. D. Micheva, K. Narayan, C. Pape, R. G. Parton, N. L. Schieber, Y. Schwab, B. Titze, P. Verkade, A. Weigel, L. M. Collinson, Volume electron microscopy, Nat Rev Methods Primers 2 (1) (2022) 51. doi:10.1038/s43586-022-00131-9.

[54] M. A. O'Keefe, "Resolution" in high-resolution electron microscopy, Ultramicroscopy 47 (1-3) (1992) 282–297. doi:10.1016/0304-3991(92)90203-V.

[55] J. Spence, The future of atomic resolution electron microscopy for materials science, Materials Science and Engineering: R: Reports 26 (1-2) (1999) 1–49. doi:10.1016/S0927-796X(99)00005-4.

[56] B. Huang, H. Babcock, X. Zhuang, Breaking the Diffraction Barrier: Super-Resolution Imaging of Cells, Cell 143 (7) (2010) 1047–1058. doi:10.1016/j.cell.2010.12.002.

[57] J. E. Greivenkamp, Field Guide to Geometrical Optics, SPIE, 2004. doi:10.1117/3.547461.

[58] B. R. Masters, Ernst Abbe and the Foundation of Scientific Microscopes, Optics & Photonics News 18 (2) (2007) 18. doi:10.1364/OPN.18.2.000018.

[59] L. D. Broglie, XXXV. A Tentative Theory of Light Quanta, Philosophical Magazine Letters 86 (7) (2006) 411–423. doi:10.1080/09500830600914721.

[60] D. B. Williams, C. B. Carter, Transmission Electron Microscopy: A Textbook for Materials Science, 2nd Edition, Springer, 2009.

[61] O. L. Krivanek, M. F. Chisholm, V. Nicolosi, T. J. Pennycook, G. J. Corbin, N. Dellby, M. F. Murfitt, C. S. Own, Z. S. Szilagyi, M. P. Oxley, S. T. Pantelides, S. J. Pennycook, Atom-by-atom structural and chemical analysis by annular dark-field electron microscopy, Nature 464 (7288) (2010) 571–574. doi:10.1038/nature08879.

[62] J. Fan, Q. Tan, J. Hao, Analysis of displacement damage mechanism and simulation proton irradiation on GaAs, AIP Advances 12 (9) (2022) 095304. doi:10.1063/5.0104457.

[63] W. A. McKinley, H. Feshbach, The Coulomb Scattering of Relativistic Electrons by Nuclei, Phys. Rev. 74 (12) (1948) 1759–1763. doi:10.1103/PhysRev.74.1759.

[64] H. Bethe, Zur Theorie des Durchgangs schneller Korpuskularstrahlen durch Materie, Annalen der Physik 397 (3) (1930) 325–400. doi:10.1002/andp.19303970303.

[65] T. Susi, J. C. Meyer, J. Kotakoski, Quantifying transmission electron microscopy irradiation effects using two-dimensional materials, Nat Rev Phys 1 (6) (2019) 397–405. doi:10.1038/s42254-019-0058-y.

[66] M. Haider, H. Mueller, Is there a Road Map of Aberration Correction towards Ultra-High Rsolution in TEM and STEM?, MAM 11 (S02) (2005). doi:10.1017/S1431927605510547.

[67] R. F. Egerton, Electron Energy-Loss Spectroscopy in the Electron Microscope, Springer US, Boston, MA, 1996. doi:10.1007/978-1-4757-5099-7.

[68] L. I. Roest, S. E. Van Heijst, L. Maduro, J. Rojo, S. Conesa-Boj, Charting the low-loss region in electron energy loss spectroscopy with machine learning, Ultramicroscopy 222 (2021) 113202. doi:10.1016/j.ultramic.2021.113202.

[69] P. Irschik, Atomically clean graphene through heating in ultra-high vacuum, University of Vienna (2024). doi:10.25365/THESIS.77045.

[70] N. Dellby, O. L. Krivanek, P. D. Nellist, P. E. Batson, A. R. Lupini, Progress in aberration-corrected scanning transmission electron microscopy, Microscopy 50 (3) (2001) 177–185. doi:10.1093/jmicro/50.3.177.

[71] R. Brydson, Aberration-Corrected Analytical Transmission Electron Microscopy, 1st Edition, John Wiley & Sons, Ltd., 2011. doi:10.1002/9781119978848.

[72] EELS.Info Atlas, last accessed on 20 March 2025.
URL https://eels.info